ANALYSIS AND DESIGN OF WIDEBAND DIELECTRIC RESONATOR ANTENNAS IN FREQUENCY AND TIME DOMAINS

by

Mian Shahzad Iqbal

Dissertation submitted in fulfilment of the requirements

for the degree of

DOCTOR OF PHILOSOPHY

Department of Engineering
Faculty of Science and Engineering
Macquarie University
Sydney, Australia

August 2015

ABSTRACT

Dielectric Resonator Antennas (DRAs) are a class of antennas that offer promising solutions to many advanced wireless communication systems due to their high radiation efficiency, compactness, light-weight and simple feed mechanisms. This thesis presents the design and characterization of novel yet simple configurations of DRAs for wideband and ultrawideband (UWB) applications. A multitude of DRAs made by stacking multiple dielectric segments are considered since they are simple to fabricate and offer wide impedance bandwidth.

This thesis proposes a DRA with a full ground plane to achieve contiguous 10-dB return-loss bandwidth of 115%, which fully encompasses the Federal Communications Commission (FCC) UWB band. This antenna is composed of two different dielectric segments and a full ground plane to produce realized mean gain of 4-5 dBi. Unlike printed planar UWB antennas with partial ground planes, the proposed DRA has a full ground plane to reduce unwanted radiation to the lower hemisphere. When used in UWB-IR system, the antenna has to receive or transmit pulsed signals. Therefore, investigating it only in the frequency domain is not enough to fully assess its performance; time-domain characterization of the antenna is essential to assess its pulse-preserving capabilities. Therefore, pulse-preserving capabilities and effective isotropically radiated power (EIRP) spectra of the tetrahedron DRA are rigorously investigated for several types of UWB input pulses. The correlations between the input pulses and the radiated pulses show that average correlation factors in elevation planes and azimuthal plane are

0.833 and 0.912, respectively. Nevertheless, EIRP spectrum calculations indicate that none of those pulses efficiently fill the FCC UWB mask when applied to this tetrahedron DRA. Hence, a third-order Rayleigh pulse is introduced and tuned in to efficiently make use of the allowed spectrum limits whilst radiating highly correlated pulses. It is worth noting that spectrum efficiency of the DRA improves from 40% to 52% as a result of the optimized input pulse.

The thesis also presents the design, implementation and testing of low-profile multi-segment dielectric resonator antennas (MSDRAs) for wideband systems. The paramount contribution of this design is to reduce the height of MSDRA for high-data-rate wireless devices. Extensive exploitation of a multitude of different dielectric segments, with respect to effective permittivity and Q factor, has provided the physical insight of the MSDRA, and led to a compact antenna design with a wide impedance bandwidth. The bandwidth-to-volume ratio of MSDRA is increased up to 73% as compared to the state-of-the-art design of a tetrahedron DRA. The proposed design is tested with both a large ground plane (40×40 mm^2) and a small rectangular ground plane (6×20 mm^2). The measured results of MSDRA with large ground plane show a 10-dB return-loss bandwidth of 83% from 4.5-10.5 GHz, and the MSDRA with the small rectangular ground plane show a a 10-dB return-loss bandwidth of 94% from 3.7-10.2 GHz.

These antenna configurations are good candidates for both impulse radio and carrier-based UWB systems and they can be used in a myriad of portable wireless applications such as wireless USB and personal area networks.

STATEMENT OF CANDIDATE

I certify that the work presented in this thesis entitled ***"Analysis and Design of Wideband Dielectric Resonator Antennas in the Frequency and Time Domains"*** has not previously been submitted for a degree nor has it been submitted as part of the requirements for a degree to any other university or institution other than Macquarie University..

I also certify that the thesis is an original piece of research and it has been written by me.

In addition, I certify that all information sources and literature used are indicated in the thesis.

. . . . . .

Mian Shahzad Iqbal

ACKNOWLEDGMENTS

This Ph.D. thesis would not have been possible without the support and contribution of many extraordinary individuals. Foremost, I would like to express my special appreciation and thanks to my principal supervisor, Dr. Karu Esselle, who has been a tremendous mentor for me. He provided me with his thoughtful guidance, constructive suggestions and constant encouragement during this work.

I would also like to acknowledge friendly co-supervision provided by Dr. Yuehe and Dr. Basit for my research projects. They assisted me at all the critical times I had faced during my research and carries an important place. I am indebted to Assistant Prof. Ladislau Matekovits (Italy) for his inspiring guidance in the field of electromagnetic in time-domain and for generously sharing his profound knowledge and experience. His encouragement holds vital importance that laid the foundation to learn more.

Many thanks must go to my colleagues in the department for their help with using Anechoic Chamber during the measurements. I would also like to thank Mr. Raheel, and Mr. Usman for the technical help and their continuous advices during the antenna fabrication process.

I am blessed to have an amazing family; my parents, brothers, and my sister. Their support has been unconditional for all these years. In particular, I

am deeply indebted to my parents who have cherished with me every great moment and supported me whenever I needed it. Without their everlasting love and esteemed guidance, I would not have accomplished anything in my life. Words are not enough to praise my wife Lubna Saeed, whose love, encouragement and motivation have guided me through the most challenging times. I must mention my daughters, Aamina Noor and Shehzeen Noor, for rejuvenating my days with their gorgeous smiles, which has made this long journey possible, endurable and enjoyable.

Finally, to Almighty God, for bestowing countless blessings on me and giving me the strength to realize my life-long dream. Thank you so much!

Mian Shahzad Iqbal

Sydeny, New South Wales

August 2015

To My Parents

Contents

List of Figures

List of Tables

Chapter 1

Introduction

The development of low-loss ceramic materials in the late 1960s opened avenues to utilizing dielectric materials as a storing element in circuit applications, such as filters and oscillators. Initially, they were enclosed in metal cavities to prevent radiation and to control high quality factor. The basic function of high quality factor is to minimize the insertion losses so that they can be used as highly selective circuits [14]. Moreover, high quality factor suppresses the electric noise in oscillator devices and improves the signal's stability.

On the other hand, the use of dielectric resonator (DR) in the absence of a metal cavity and appropriate feed to the dielectric resonator can turn it into a radiating element or function like an antenna. Furthermore, lowering the dielectric constant of dielectric material makes it ideal as an efficient radiator over a broad range of frequencies [15, 16].

In the early 1980s, cylindrical, rectangular, and hemispherical shapes of DR were investigated for their possible use as an antenna element [17–19]. From that point onward, a substantial amount of characterization was undertaken by several researchers [20–30].

It emerged that DR can confine microwave energy within itself, provided that the energy is fed in the appropriate direction. Emphasis at that time was mostly on miniatur-

ized designs to address the needs of portable wireless applications. Till now, a myriad of novel dielectric resonator antenna (DRA) shapes or hybrid antennas have been designed to meet the requirements of emerging broadband systems [31–35]. The shape of a DR can be tubular, spherical and parallelepiped, as shown in Fig. 1.1(a). These DRs are being employed in base stations as antennas and filters. In Fig. 1.1(b), many of dielectric ceramics have been developed in the Sebastian's laboratory for research purpose.

(a) (b)

Figure 1.1: (a) Dielectric resonators used in base stations (b) Dielectric ceramics developed in Sebastian's Lab [1, 2]

A DR is an electromagnetic component that exhibits resonance with useful properties for a narrow and broad range of frequencies. It generally consists of ceramic puck with high permittivity. There are number of ways to excite these DR to function as an antenna and these include probe feed, aperture coupling and microstrip feeding. DRAs are attractive because of their wide range of applications from terrestrial and satellite communication including software radio, GPS, and DBS TV. The recent progress in microwave telecommunications, satellite broadcasting and intelligent transport system (ITS) has resulted in rising demand for DRs, which are low loss and used mainly in wireless

communication devices.

The present use of electro-ceramic components requires increasing control of the materials to better master the final properties, which are becoming increasingly critical for practical applications. Two main factors, permittivity (ε) and dissipation (tanδ), have to be considered to document the level of performance during practical applications. On the basis of the different domains of application, other parameters related to these factors are currently being used: loss factor ($\varepsilon'' = \varepsilon' tan\delta$) and quality factor ($Q = 1/tan\delta$).

1.1 UWB Technology and Emerging Trends

At present, global regulations and standards for ultrawideband (UWB) technology are still being considered and constructed. However, research on UWB has made great advances. Freescale Semiconductor was the first company in the world to produce UWB chips and its XS110 solution is the only commercially available UWB chipset to date [3], which is shown in Fig. 1.2. It provides full wireless connectivity implementing direct sequence ultra wideband (DS- UWB). The chipset delivers more than 110 Mbps data transfer rate supporting applications such as streaming video, streaming audio, and high-rate data transfer at very low levels of power consumption.

Figure 1.2: Freescale XS110 UWB chipset [3]

At the 2005 3GSM World Congress, Samsung and Freescale demonstrated the world's

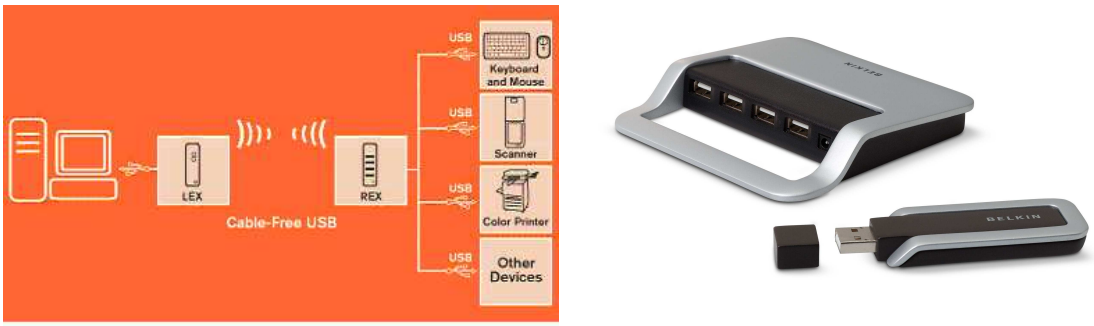

(a) (b)

Figure 1.3: (a) Cable-free diagram structure (b) Belkin's Cable-free hub [4]

first UWB-enabled cell phone featuring its UWB wireless chipset [4]. Belkin's four-port hub, shown in Fig. 1.3 (b), enables immediate high-speed wireless connectivity for any USB device and requires no software. USB devices plug into the hub with cords, but the hub does not require a cable to connect to the computer. Therefore, it gives desktop computer users the freedom to place their USB devices where it is most convenient for them. Laptop users also free to roam wirelessly with their laptop around the room while still maintaining access to their stationary USB devices, such as printers, scanners, hard drives, and MP3 players.

Analogously, Haier Corporation and Freescale Semiconductors showcased the first UWB-enabled LCD, high definition television (HDTV) in 2005 [5], as shown in Fig.1.4. This freescale technology capable of transferring multiple high definition movie streams wirelessly, up to 110 megabits per second (Mbps), at a distance up to 20 meters.

Figure 1.4: Ultrawideband LCD [5]

1.2 Motivation of the Research

The evolution of electronic communication in the last two decades, especially that of the internet and the shrinking size of mobile phones to pocketsize smart phones, have transformed the world into a global village. This transformation has substantially made a huge impact following the release of a Federal Communications Commission (FCC) ruling to use the unlicensed low-power electronic devices from 3.1 GHz to 10.6 GHz in 2002 [36]. Since the release of the ultra-wideband spectrum, demand for extremely high-speed data services and multimedia applications has risen exponentially. To meet the needs of high capacity wireless links, broadband antennas must be able to communicate effectively between the electronic devices. Secondly, miniaturization of electronic products has put limitations on bulky-sized antennas, and consequently urging for compact antennas for UWB systems are now in great demand.

Many UWB consumer applications are playing an active role in personal area network (PAN) by using wired links. These include laptop to modem connection, laptop to printer, and DVD player to TV screen. However, converting all wired connections into unwired format is a major challenge, especially the high data rate video links. Therefore, it is

anticipated that the UWB modules will be part of every consumer electronic application in the near future. As a result, there is a need for a high-data-rate transceiver of compact size to meet the stringent requirements of UWB systems.

To fulfill these requirements, many UWB antenna solutions are available, such as printed planar antennas. The paramount intention of designing printed planer antennas is to radiate their energy in one particular direction i.e., the upper hemisphere. However, they do radiate significantly to the lower hemisphere (unwanted direction) because the partial ground plane does not act as a shield to block this radiation. When such an antenna is integrated to the top of a wireless device (such as wireless-enabled Blu-Ray player), radiation into the lower hemisphere is wasted inside the device.

Secondly, metallic antennas tend to make more conductor loss at higher frequencies and this leads to them being poor radiator. Therefore, alternative antenna solutions with unmetalized material and high radiation efficiency are highly desirable.

DRAs are potential candidates for many present and future wireless communication systems owing to their high radiation efficiency, low-loss, light-weight, ease of excitation, and relatively wide bandwidth in comparison with the microstrip antenna. Fig.1.5 (a) and (b) show the application of DR which is integrated in cellular phones. In microstrip antennas, a printed slot is used to radiate whereas DRAs are radiated through the whole surface except the grounded part. Avoidance of surface waves is another attractive advantage of the DRA over the coplanar waveguide microstrip antenna. Furthermore, DRA can be designed with a full ground plane to reduce power wastage in the lower hemisphere. This gives a motivation to investigate and design DRAs that can operate at wide frequency bands by using different dielectric materials. The target performance parameters are contiguous return loss bandwidth (3.1-10.6 GHz), a compact multi-segment dielectric material for wideband operations with constant gain, stable radiation pattern, high fidelity factor and EIRP (effective isotropic radiated power) as per FCC mask.

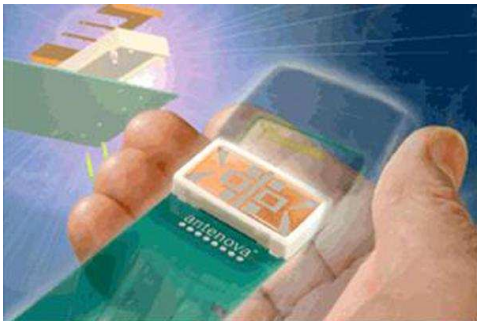

(a)

(b)

Figure 1.5: Dielectric ceramics used in mobile phone

1.3 Research Framework and Objectives

When this research started, back in 2012, a variety of wideband dielectric resonator antennas had already been designed globally for various wireless applications. In addition, a probe-fed DRA was designed and investigated for UWB applications. Following are the objectives of the dissertation.

- To design and characterize novel yet simple DRA for the UWB system
- To rigorously exploit time-domain characterisation of UWB DRA
- To reduce the DRA's volume-to-size ratio for the UWB system
- To test the DRA for medical and body area network

This thesis deals with the design and analysis of wideband dielectric resonator antennas and ultrawideband dielectric resonator antenna. The research investigates new methods to design different DRA configurations and design and implement antennas as the major task. To assist the design and analysis of DRAs in frequency and time-domain, numerical investigations are conducted, in ANSYS high-frequency structure simulator (HFSS)

and CST microwave studio (CST MWS), to address issues related to the contiguous input impedance matching, consistent radiation pattern, moderate gain, high radiation efficiency, high correlation factor, and EIRP mask. In addition, the thesis presents the design, implementation and testing of low-profile multi-segment dielectric resonator antennas (MSDRAs) for wideband systems. The paramount contribution of this design is to miniaturize the height of MSDRA for high-data-rate wireless devices. Extensive exploitation of a multitude of different dielectric segments, with respect to effective permittivity and Q-factor, provides physical insight into the MSDRA leading to compact antenna design with wide impedance bandwidth.

1.4 Overview of the thesis

The thesis consists of six chapters, including this introductory chapter and the second chapter that reviews the necessary background and current state of the art on DRAs. The next four chapters are organized as follows:

In Chapter 3, DRA with full ground plane is presented for UWB communication. An air gap is introduced in the DRA to enhance the impedance bandwidth of antenna. A detailed study is carried out to investigate the effects of its air region on the bandwidth performance of the antenna.

In Chapter 4, time-domain characteristics and EIRP spectra of the UWB DRA are investigated for several types of UWB input pulses. Furthermore, pulse performance of the antenna is improved by investigating the design parameters of the UWB DRA.

In Chapter 5, a low-profile multi-segment DRA (MSDRA) for wideband applications is described. The aspect ratio and effective permittivity of a low-profile DRA are investigated in order to enhance the MSDRA's bandwidth-to-volume ratio. In addition, a novel design of a wideband MSDRA with miniaturized ground plane is presented. In

order to miniaturize the overall antenna's size, ground plane is rigorously analysed and consequently its bandwidth performance is improved.

Finally, Chapter 6 recapitulates the key research findings, concluded the thesis and presents guidelines for future work.

1.5 Major Contribution

This thesis rigorously characterizes the spectral and temporal properties of UWB DRA. In the spectral domain, obtaining contiguous impedance bandwidth in UWB range is a challenging task. Therefore, a novel structure of DRA has been designed to achieve a clear contiguous 10 dB return loss in the entire UWB band. The radiation patterns of DRA at different frequencies show that most of the power is radiated in the upper hemisphere, reducing the power wastage in an undesired direction. Moreover, peak gain of 6-7 dBi is maintained throughout the band.

Characterization of time-domain behavior is an integral part of UWB communication devices. Therefore, extensive analysis has been done to exploit the temporal properties of DRA. Firstly, three different broadband pulses, already described in the literature, have used to excite the signal. The pulse-preserving characteristics of UWB DRA have been computed in the XY, XZ and YZ planes. Excellent pulse-preserving capabilities are demonstrated by UWB DRA. Additionally, effective isotropic radiated power (EIRP) has been computed in order to fill the FCC mask completely. However, none of these pulses fully utilize the FCC mask. Consequently, a new third-order Rayleigh pulse has been introduced after a thorough investigation of different types of pulses. The EIRP curve generated by third-order pulse fully conforms the FCC mask. It also shows excellent preserving capabilities in all important directions.

The dissertation also presents the design, implementation and testing of low-profile

multisegment dielectric resonator antennas (MSDRAs) for wideband systems. The most important contribution of this design is to reduce the height of MSDRA for high-data-rate wireless devices. The bandwidth-to-volume ratio of MSDRA is increased up to 73% when compared to the state-of-the-art design of a tetrahedron DRA. The measured results of MSDRA with a large ground plane show a 10-dB return-loss bandwidth of 83% from 4.5-10.5 GHz, and the MSDRA with the rectangular ground plane show a a 10-dB return-loss bandwidth of 94% from 3.7-10.2 GHz.

Chapter 2

Background and Literature Review

2.1 Introduction

Dielectric Resonators (DR) were first theoretically introduced by Richtinger in 1939 [37], and their modes were first analysed by Okaya and Barash [14]. At that time, DRs were mostly used as energy storage applications such as circuits, oscillators and filters [24]. One of the major reasons to use in aforementioned applications was due to its high Q factor. Normally, DRs were covered by metal cavities to maintain their high Q factor. If the DRs are uncovered by metal cavities, they become efficient radiator.

In the early 1980s, DRs were first studied as an antenna and since then they were known as Dielectric Resonator Antenna (DRA). Different shapes of Dielectric Resonators were first assessed by Long, McAllister and Shen [17–19]. In the late 1980s, different parameters of DRs were focused on such as mode of excitation, feed mechanism and applying analytical and numerical techniques to find the Q factor and input impedance. The major research contribution in the field of DRAs was done by Kishk et al. and so on [19,20,22,38–42]. During the mid 1990s, developments in low profile designs [22,43–45], and multi-band/wideband design [46] were reported in research publications.

Up till now, hundreds of research papers have been published on DRAs. Work has continued in the area of miniaturization, low profile, compact and wideband designs. Some of the emerging research includes bandwidth enhancement, finite ground plane effect, tunable dielectric resonator antenna, reconfigurable patterns and ultra-wideband designs.

2.2 Basic Characteristics

Early investigation of the simple shape DRAs concludes on some major characteristics which are applicable to most DRAs. These are outlined below as follows:

- The size of the DRA decreases and becomes more compact if dielectric constant increases
- By increasing the dielectric constant, Q factor will increases and the bandwidth of antenna will become narrower. On the other hand, the small value of dielectric constant makes the DRA operational on a wide range of frequencies but DRAs' dimensions expand in size
- Aspect ratio has a significant effect on the resonance frequency and radiation Q factor, given that the dielectric constant remains constant
- DRAs experience minimal conductor loss due to inherent properties of dielectric materials, even at millimetre-wave frequencies
- A wide range of dielectric constant allows the designer to control the physical size and resonance frequency which range from 1.3 GHz to 40 GHz
- Feeding mechanisms of DRAs depend on the coverage requirements and integration of antenna with other technologies

Numerous feeding techniques are available such as probes [18, 29, 47, 48], slots [20, 49–51], microstrip lines [52, 53], dielectric image guide [54, 55] and coplanar waveguide [56, 57] to efficiently excite the DRAs. In last decade studies were motivated by an observation that bandwidth requirements exponentially rise with the high-data-rate wireless communication devices. In addition, FCC authorized the unlicensed use of UWB in the frequency range from 3.1 to 10.6 GHz. UWB frequency range covers several applications such as WLAN, Wi-Max, Bluetooth, Geo-positioning, Radar/Sensor, Wireless Body Area Network, mobile communications, underwater, space, sports, military and emergency medicine measurements.

2.3 Shapes of DRA

There are a number of ways to present the shapes of DRA according to the application being used. However, these shapes are classified into three basic ones: rectangular, cylindrical and hemispherical. Each shape has its own analytical solution for defining resonant frequency, radiation Q factor and radiation pattern of the DRA. In cylindrical DRA, ratio of radius/height controls the resonant frequency and Q factor whereas in rectangular DRA aspect ratio (length/width and height/width) controls the resonant frequency.

2.3.1 Rectangular DRA

The focus of this dissertation is on rectangular-shaped DRAs, to further enhance the bandwidth performance of Yuehe's design [58], and from now onward DRAs of rectangular structure will be discussed in detail. The DRA with rectangular cross-section is characterized by a height, width, length, and a dielectric constant. Depending on the application, a rectangular DRA with either a small footprint or low profile can be selected. A number of different dimensions (aspect ratios) are possible for the same dielectric constant

and resonant frequency [15].

2.4 Principle of Operation

This section outlines the theory of rectangular DRA used in the design and analysis of DRA in this thesis. Several models have been formulated to calculate resonant frequency and impedance bandwidth of linearly polarized DRA [59–61].

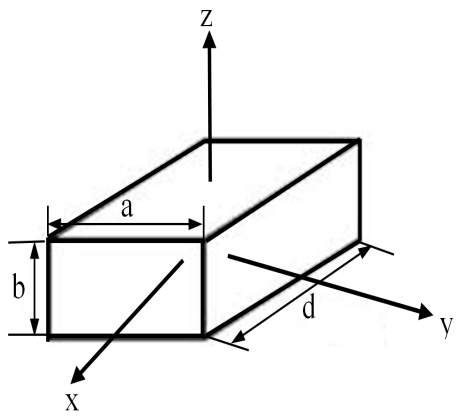

Figure 2.1: Geometry of isolated dielectric resonator antenna

Fig. 2.1 illustrates an isolated rectangular DR. Unlike spherical or cylindrical DR's, rectangular structures find it difficult to classify the modes. One major reason is the sharp edges, which are difficult to incorporate while doing numerical computations. Thus, no exact approximation as yet exists. This is despite Van Bladel having presented a general analysis of the modes of an arbitrarily shaped DR of very high permittivity [62,63]. Further, it is assumed that the material of DR is lossless. Van Bladel has grouped the modes of a DR into *confined* or *nonconfined* type. For both types of modes, the following boundary condition is satisfied at all the surfaces of the resonator:

$$E \cdot n = 0 \tag{2.1}$$

where E represents the electric-field intensity and 'n' represents the normal to the surface of the resonator. This is one of the conditions that fields satisfy at a magnetic wall. Equation 2.1 for all the surfaces of the DRA are considered to be *nonconfined*.

The second magnetic wall condition, i.e.

$$n \times H = 0 \tag{2.2}$$

is not necessarily satisfied at all surfaces of the DR by all the modes. The modes of a DR which satisfy both 2.1 and 2.2 are known as *confined* modes. The lowest order *nonconfined*. and *confined* modes radiate like magnetic and electric dipoles, respectively. It has been observed that, due to the body of revolution, spherical and cylindrical shapes have supported *confined* modes whereas rectangular DR can support *nonconfined* modes due to no body of revolution. Therefore, rectangular DR can only satisfy one of the condition of a magnetic wall as given by equation 2.1.

Okaya and Barash proposed that modes of a rectangular DR can be divided into two types [14]: TE(H) and TM(E). However, when DWM is used to locate the fields of lowest order TM(E) mode, it does not satisfy equation 2.1. On the contrary, TE(H) mode is well known and it satisfies the conditions of *nonconfined* modes. Consequently, only the lowest order mode known as $TE_{\delta 11}$ is discussed in this thesis.

In order to model the DRA, the waveguide is truncated along x-direction at $\pm\frac{d}{2}$ with magnetic walls. This model can be used in two different forms. In the first case, isolated DRA in free space with dimensions a, b, and d whereas in second case DRA is mounted on a ground plane with dimensions a, b/2, and d as shown in Fig. 2.2. In the latter case, DRA will be reside on a conducting surface and therefore an equivalent dielectric waveguide would also be included the mirror image of the DRA.

For a rectangular DRA with dimensions a, b > d, the lowest order mode will be $TE^{x}_{\delta 11}$. The field components of the rectangular dielectric resonator are employing dielec-

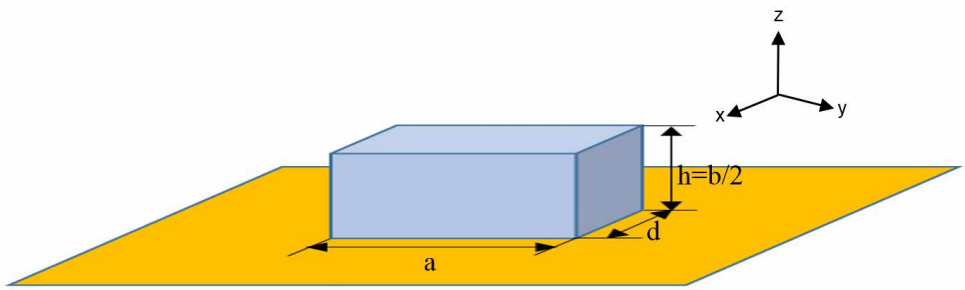

Figure 2.2: Geometry of the dielectric resonator model on ground plane

tric waveguide model [59] :

$$
\begin{aligned}
E_y &= k_z \cos(k_y y) \sin(k_z z) \cos(k_x x) \\
E_z &= -k_y \sin(k_y y) \cos(k_z z) \cos(k_x x) \\
E_x &= 0 \\
H_y &= \frac{k_y k_x}{jw\mu_o} \sin(k_y y) \cos(k_z z) \sin(k_x x) \\
H_z &= \frac{k_z k_x}{jw\mu_o} \cos(k_y y) \sin(k_z z) \sin(k_x x) \\
H_x &= \frac{k_y^2 + k_z^2}{jw\mu_o} \cos(k_y y) \cos(k_z z) \cos(k_x x)
\end{aligned}
\tag{2.3}
$$

where A is an arbitrary constant and k_x, k_y, and k_z denote the wave number along the x, y, and z directions, respectively, inside the DR. For guided modes the fields are confined within the guide and a further approximation can be made as follows:

$$k_y = \frac{m\pi}{a} \tag{2.4}$$

$$k_z = \frac{n\pi}{b} \tag{2.5}$$

This approximation is equivalent to assuming the magnetic walls exists at $y = \pm\frac{a}{2}$ and $z = \pm\frac{b}{2}$. Further, by using DWM [59], the following transcendental equation is obtained for the wave number k_x:

$$k_x^2 + k_y^2 + k_z^2 = \varepsilon_r k_o^2 \tag{2.6}$$

$$k_x \tan(k_x d/2) = \sqrt{(\varepsilon_r - 1)k_o^2 - k_x^2} \tag{2.7}$$

where k_o denotes the free space wave number corresponding to the resonant frequency. For given resonator parameters ϵ_r, a, b, and d the resonance frequency of DRA is one at which wavenumber k_x, determined using 2.4, 2.5, and 2.6 also satisfy 2.7.

2.5 Q Factor of the fundamental TE_{111} mode

The Q factor of the DRA is determined using [40]:

$$Q = 2\omega_0 \frac{W_e}{P_{rad}} \tag{2.8}$$

where W_e and P_{rad} are the stored energy and radiated power, respectively. These quantities are given by:

$$W_e = \varepsilon_o \varepsilon_r abd \left(1 + \frac{\sin(k_x d)}{k_x d}\right)(k_y^2 + k_z^2) \tag{2.9}$$

$$P_{rad} = 10k_o^4 \left|p_m\right|^2 \tag{2.10}$$

where p_m is the magnetic dipole moment of the DRA:

$$p_m = \frac{-jw8\varepsilon_o(\varepsilon_r - 1)}{k_x k_y k_z} \sin(k_x d/2)\hat{x} \tag{2.11}$$

The Q factor can be computed by substituting Eqs. 2.9 and 2.10 into Eq. 2.8. These equations relate the Q-factor to the dielectric permittivity and DR dimensions. It can be seen that Q factor is approximately proportional to $\varepsilon_r^{3/2}$. This relationship suggests that the increase in dielectric permittivity leads to an increase in confinement of energy in the DR and the radiated power declines. Thus, Q factor increases. Since the Q factor is inversely proportional to bandwidth, the bandwidth of the DRA will decrease.

2.6 Feeding Structures

The selection of the feed and its location both play an important role in maximizing the input matching of the DRA. Feeding to DRAs is possible by making the excitation element function in two different ways: a) electric current, and b) magnetic current. The amount of coupling, k, between the source and the fields within the DRA can be determined using Lorentz Reciprocity Theorem and coupling theory. For an electric current source $\mathbf{J}_e$

$$k \propto \int_V (\ E\ .\ J_e\ )\ dV \tag{2.12}$$

and for a magnetic source $\mathbf{M}_e$

$$k \propto \int_V (\ E\ .\ M_e\ )\ dV \tag{2.13}$$

where V is the volume of the source within which electric or magnetic current exists, while E and H are the electric and magnetic fields within the DRA. Eq. 2.12 implies that electric (magnetic) current source should be located in the region of strong electric (magnetic) fields within the DRA in order to achieve maximum coupling between them. In these cases, probe is the perfect example of the electric current source whereas aperture or loop is the perfect example of the magnetic current source.

Fig. 2.3 shows the E-field distribution of fundamental mode (TE_{111}) inside a rectangular DR. Dielectric resonators can be excited by different types of feeding structures. Most of the common methods involve microstrip feeding or probe-feed. Besides this, DRA with wave guide, aperture coupling and dielectric image guide have been reported in the literature. The design of antennas used in this thesis comprises feeding with a probe, and subsequently this feeding mechanism will be discussed in greater detail compared to the other feeding methods.

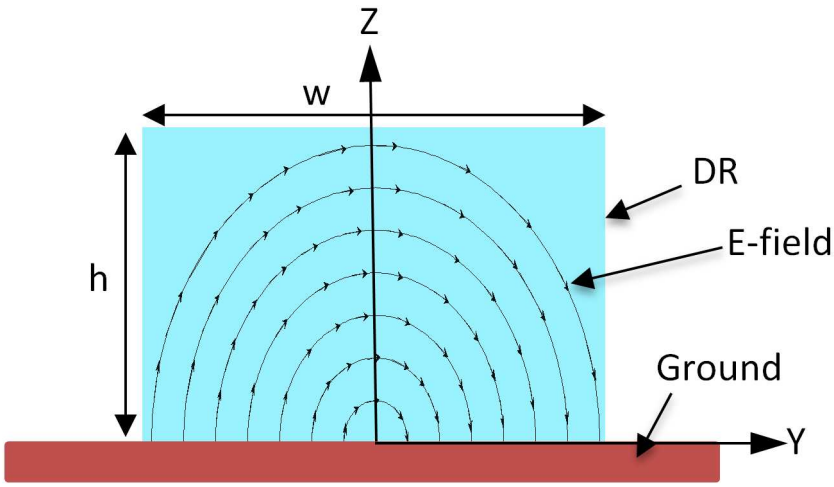

Figure 2.3: E-field distribution of rectangular DR

2.6.1 Coaxial probe

Using a coaxial probe is one of the common methods used to excite a rectangular DRA [18, 58, 64–66]. The probe consists of the center pin of a coaxial transmission line that protrudes through the ground plane, as shown in Fig. 2.4 (a). Feeding of the DRA is possible either by accommodating the probe inside the DRA or by placing the probe adjacent to it. It is important to mention that the probe can be considered a vertical current source, and therefore in order to achieve strong coupling with the DRA, precise position and height of the probe play a pivotal role to match the input impedance and resonant frequency of the DRA.

In Fig. 2.4 (b), the strip-fed method is used to excite the DRA, which is compatible with a coaxial probe [46, 60, 67]. This method has the distinct advantage over the coaxial probe counterpart in that it facilitates post-manual trimmings.

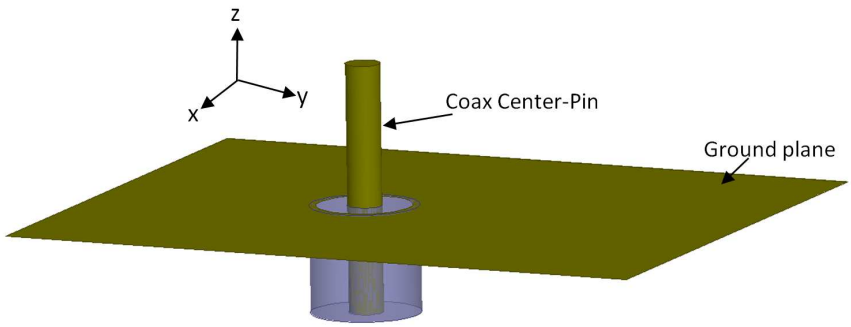

(a) Probe-fed method

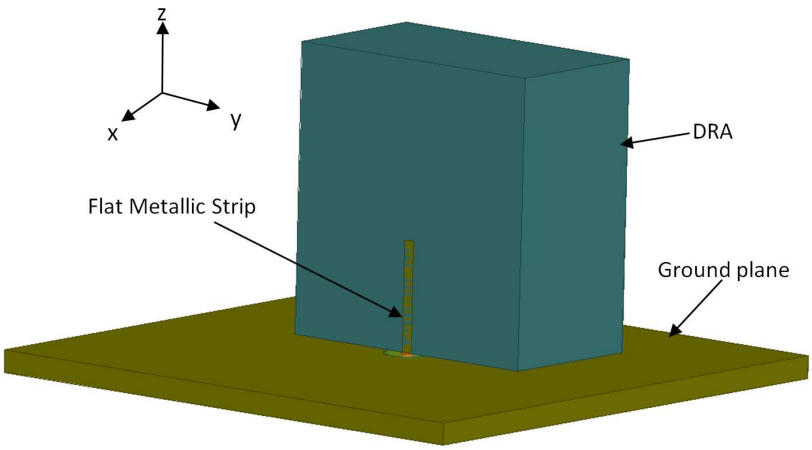

(b) Strip-fed method

Figure 2.4: Vertical probe sources

2.6.2 Microstrip Line

Compared to coaxial probe, another method, commonly used to couple dielectric resonators, is known as microstrip lines, as shown in Fig. 2.5. In this method, magnetic fields in the DRA are efficiently utilized to couple with microstrip line. It means that the DRA is excited without any physical contact with the feeding line. This type of mechanism is very useful in printed feed distribution networks and microwave circuits.

The effect of coupling between the DRA and microstrip line can be controlled by adjusting the lateral position of the DRA. Apart from this, coupling can be made more

efficient by increasing the permittivity of the dielectric resonator. Therefore, DRAs' array are required in order to enhance the coupling which leads to efficient radiation and to minimizes a substantial amount of power from reaching the end of the transmission line [55,68,69]. However, the drawback in using array is that polarization of the DRAs depends solely dependent on the orientation of the microstrip line i.e., the direction of the magnetic field in the DRA is parallel in the DRA to the microstrip line [6].

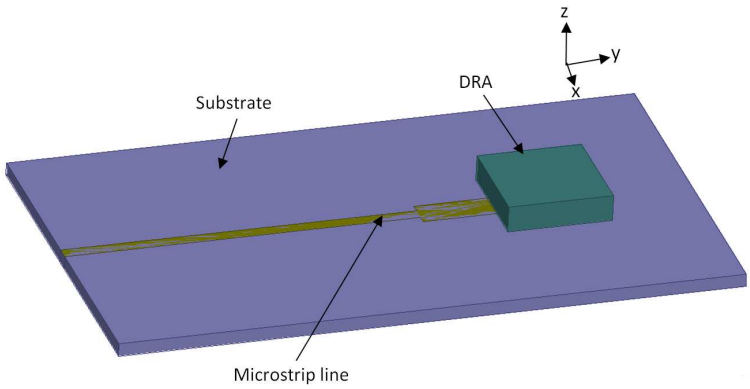

Figure 2.5: Microstrip feeding line [6]

2.7 Multisegment DRA

In some cases, the high number of DRAs may not be practical, especially for commercial applications where cost is an important factor. Therefore, to achieve strong coupling between the DRA and the microstrip feed line, the value of the DRA's dielectric constant should be relatively higher compared to the conventional DRA (usually more than ε_r =20) [15]. Since the radiation Q factor is proportional to the dielectric constant which leads to narrow DRA's impedance bandwidth. Therefore, in order to achieve wider bandwidth, lower values of dielectric constant are considered. However, this leads to poor coupling between the microstrip line and the DRA.

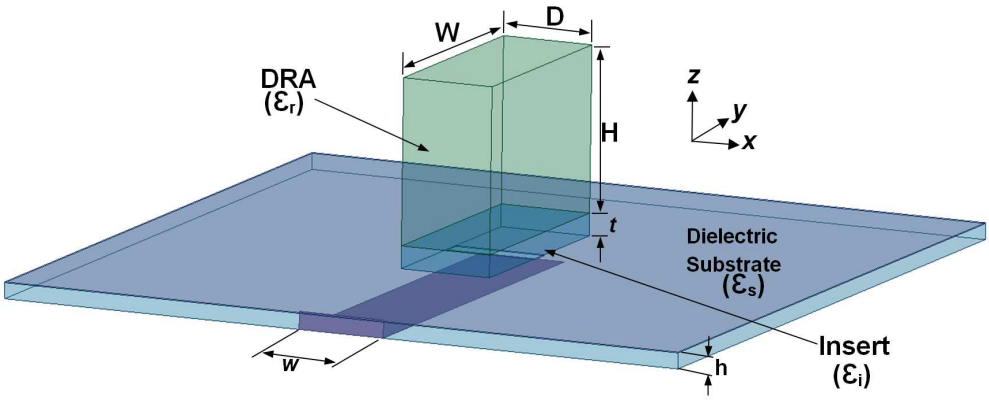

Figure 2.6: The multisegment dielectric resonator antenna [7]

In order to mitigate the predicament of DRA's weak coupling, many dielectric segments are placed in a stacked arrangement which is known as multisegment DRA (MSDRA) [7], as shown in Fig. 2.6. The DRAs of lower permittivity segment are inserted between the different higher dielectric segments in order to better transform the impedance of the DRA to that of the microstrip line. This method significantly improves the coupling performance of the DRA.

The MSDRA can be designed using the equations for the rectangular DRA as mentioned earlier. To account for the effect of the insert and the microstrip substrate on the resonant frequency of the MSDRA, the dielectric waveguide model equations are modified by including an effective permittivity and effective height. The effective permittivity of the MSDRA is calculated using [7]:

$$\varepsilon_{eff} = \frac{H_{eff}}{h_{1/\varepsilon_r} + t/_{\varepsilon_i} + s/_{\varepsilon_s}} \tag{2.14}$$

where ε_r, ε_i, and ε_s are the dielectric constants of the DRA, insert, and substrate, respectively. The effective height (H_{eff}) is simply sum of the DRA height (h), insert

thickness (t) and substrate thickness (s):

$$H_{eff} = h + t + s \tag{2.15}$$

Equation 2.14 and 2.15 are substituted into 2.7, with ε_{eff} replacing ε_r and $2H_{eff}$ replacing b.

2.8 Low profile and compact DRA

The aspect ratio of most shapes of dielectric resonator antennas can be altered while maintaining the same resonant frequency, for a given dielectric constant. More insight can be obtained by using the high permittivity of the dielectric resonator in order to miniaturize the antenna size. This will, however, resulting in an an undesirable reduction in bandwidth. As the dielectric constant increases, the radiation Q factor of the antenna will in fact increase as $\varepsilon_r^{3/2}$, leading to very narrow impedance bandwidth. Therefore, alternative techniques are required to reduce the size of DRA. In one approach [64,70], an additional metal plate from one side of the DRA is employed to reduce the length from $\lambda/2$ to $\lambda/4$. By applying image theory, field distribution remains the same and therefore reduced the volume of DRA by half. Another method to reduce the size of antenna by reducing the effective permittivity, is to use multisegment DRAs as discussed in the previous section.

2.9 Bandwidth Enhancement of DRA

Dielectric resonator antenna can attain broader impedance bandwidth if various enhancement techniques are implemented. Some of these techniques depend on shaping the DRA geometry such as split-cylindrical DRA, cylindrical-ring DRA, stair shaped DRA or tetrahedral shaped DRA [20, 30, 31, 71–77]. Some others depend on using more than one

dielectric material such as the multi-segment DRAs and others. Most of these designs rely on combining a multiple resonance to achieve wide impedance bandwidth.

The bandwidth of DRA can be increased by an appropriate design of the feeding element or by introducing an air gap between the DRA and ground plane. In recent years, attempts have been made to design different type of feed element which include: i) resonating rectangular slot feed ii) Ring-Aperture Feed iii) U-shaped-Aperture feed iv) Microstrip-Fed DRAs v) Dual Mode Rectangular DRAs vi) Cavity Backed Disk [51, 54, 78–80]. Analogously, some additional factors are introduced into DRA to enhance the impedance bandwidth. Most important is an air gap between the DRA and ground plane. This air region reduces the antenna's effective permittivity which is the main cause of bandwidth improvement. To further enhance the concept, several papers have been published on Ring DRAs, Multiple DRA, stacked DRAs and coplanar DRAs.

Similarly, bandwidth enhancement can be achieved by introducing some simple modifications, such as slicing a notch, using a multiple shape or altering the shape together. Therefore, a lower Q factor is obtained by removing the dielectric material's central part of the cylindrical DRA. A similar concept can be carried forward to the rectangular DRA.

2.10 Motivation to work in low-profile UWB DRA

In this digital age of high-speed wireless personal area networks (WPAN), current state-of-the-art standards are being developed by every day. Most of the antennas used in UWB technology are planar conducing antennas with a unique set of characteristics. On the other hand, DRA consists of ceramics and it has its own unique advantages over other antennas. Antenna's miniaturization is another aspect which needs to be achieved in cutting-edge technologies. In order to scale-down the size of antennas, DRA has outstanding capabilities to offer the miniaturize structure. For this reason, DRA is an important

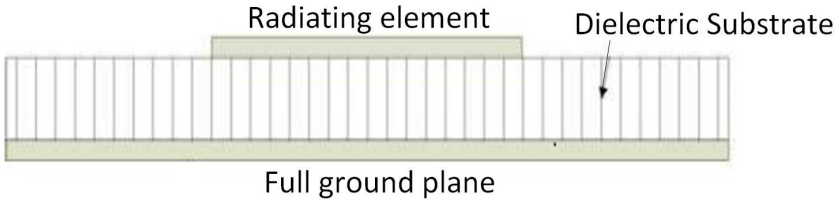

(a)

Figure 2.7: An antenna with full ground plane

potential candidates for emerging technologies.

Some of the latest technology that has been recently reported in literature [81], concerning high-speed WPAN devices, has evolved with the following new standards or systems: Certified Wireless USB (WUSB), Bluetooth, TransferJet, WirelessHD, and Wireless Home Digital Interface (WHDI).

Unlike other UWB antennas , DRA with finite ground plane, as shown in Fig .2.7, radiates most of the power in the upper hemisphere. On the other hand, all partial ground planes (see examples are shown in Fig .2.8) radiate all most 50% of the power into the lower hemisphere inside the device because the ground plane does not act as a shield to block this radiation. When such an antenna is integrated into the top surface of a wireless device case this radiation into the lower hemisphere is wasted. Therefore, such antennas cannot be placed close to and parallel to conducting surfaces such as a metal case. As a result, an analysis of UWB DRA's ground-plane is of paramount motivation if these above-mentioned predicaments are to be resolved.

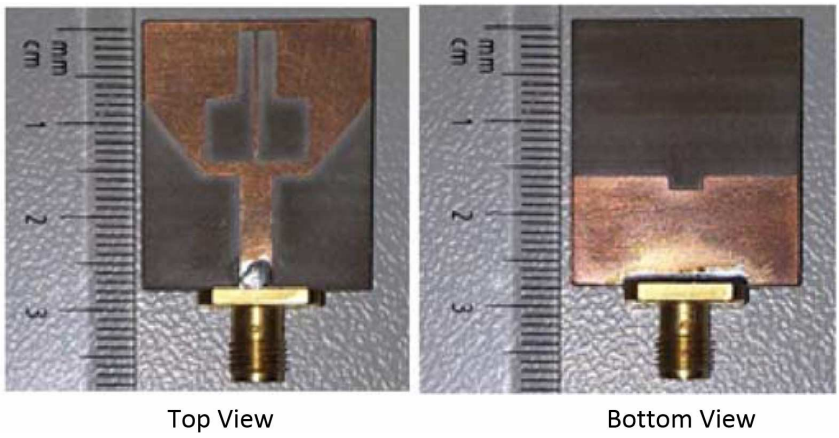

(a)

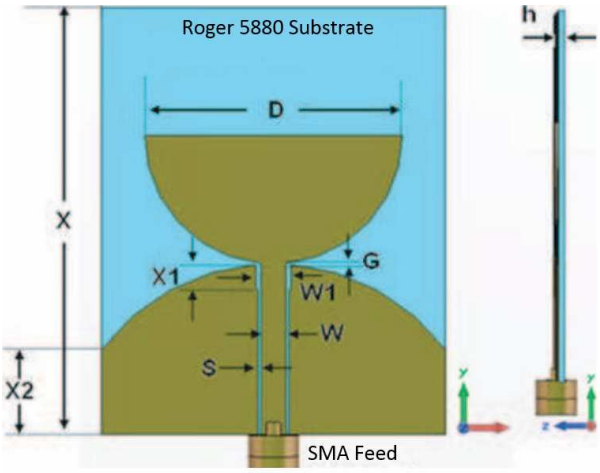

(b)

Figure 2.8: UWB antennas with partial ground planes [8, 9]

2.11 Preliminaries of UWB systems

Antenna analysis and design is a key topic that has been used for many dissertation and developed number of antenna products. One of the important things to understand about antenna's characterization is the scope of application in which it is being used. Before discussing the UWB antennas in this thesis, we should have some knowledge about UWB technology. Some of the important questions are : how it evolved, what are the rules and regulations to use this technology and what are its applications.

The following section presents ultra-wideband technology and different techniques that have been used to cover its requirements. The technology itself is not important if it is not implemented, and therefore a brief knowledge of the applications that have been developed and studied over the past years will be described here.

The standards and regulations are essential to govern the technology worldwide and consistently. In this thesis, we are more interested in the emitted radiated power and frequency allocation. These factors are closely linked to the wideband antennas.

2.12 Historical Background of UWB

The magic and mystery of radio have captured the imagination from the earliest speculation of William Crookes (1832-1919) to the present day [82]. Marconi (1874-1937) was among the first to realize the possibility of radio communication. He was convinced that this scientific invention had practical applications. With the passage of time, Marconi and others continued to improve radio technology, and they moved beyond spark-gap devices (narrowband system) and implemented continuous wave radio systems.

At that time people were more interested in narrowband systems, and eventually efficient narrowband systems came into existence. In contrast, bulk broadband antenna designs were largely forgotten, awaiting research by a later generation of antenna engi-

neers.

Through the late 1980's, UWB technology was referred to as baseband, carrier-free or impulse technology, since the term "ultra wideband" was not used until 1989 by the U.S. Department of Defense. From 1960-1999, over 200 papers were published in accredited IEEE journals, and more than 100 patents were issued on topics relating to UWB technology [13].

2.13 Ultra-wideband Systems

In the past 20 years, UWB has been used for radar, sensing and military communication. A significant change occurred in February 2002 when the US Federal Communication Commission (FCC) issued a ruling that UWB antennas can be used for data communication applications. However, FCC made it clear that if the entire 7.5 GHz band is optimally utilized , the maximum power available to a transmitter is approximately 0.5 mW. The power used over the whole band is much less than the power used by narrowband systems, as shown in Fig. 2.9. Therefore almost no interference is produced, as the power level transmitted is nearly at the noise level of the systems using the same spectrum, making it possible to share the spectrum and space with other existing technologies. This power limitation effectively relegates UWB to indoor, short-range communications for high-data-rates. A number of applications have been proposed,such as wireless USB and personal area networks, offering 100 Mbps to several Gbps with a distance ranging from 1 to 4 meters.

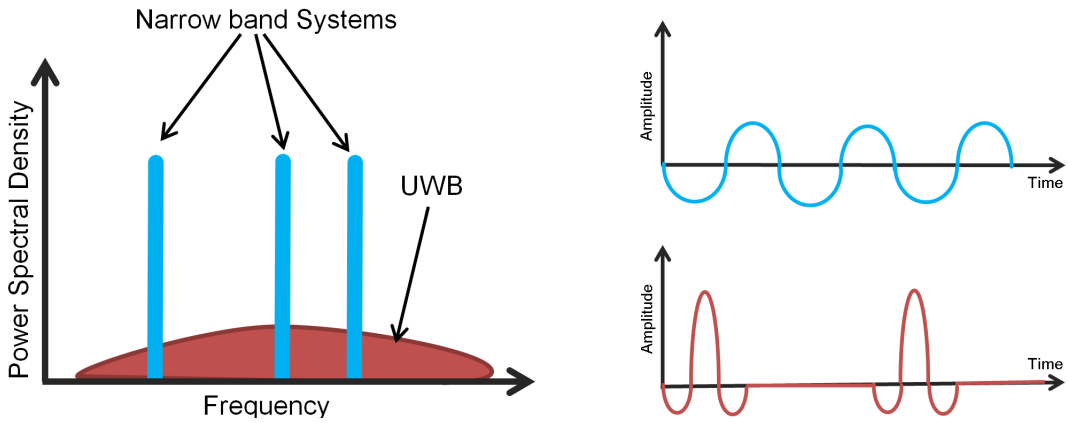

(a) (b)

Figure 2.9: Gain Pattern of Narrow band and Ultrawideband systems: (a) Frequency and, (b) Time domain.

2.14 Characterization of UWB antennas

2.14.1 Antenna Matching

Antenna matching is one of the key requirements when designing an antenna. A good impedance match between the antenna and transmission line maximizes the power transfer and efficient use of an antenna. On the other hand, a poor match leads to unwanted reflections and resonance in the antenna. Therefore, one can say that antenna matching represents the quality of antenna. There are a number of ways to express the quality of antenna which includes voltage standing wave ratio (VSWR), Scattering parameter known as LogMag S_{11} (dB) , and power loss (%).

The voltage reflection coefficient (or S_{11}) at the input port of antenna is defined as [13]

$$\Gamma = \frac{Z_L - Z_T}{Z_L + Z_T} \tag{2.16}$$

where Z_L and Z_T are the impedances of the antenna and the transmission line, respec-

tively. It can be expressed in power as [13]

$$\Gamma_{dB} = 20\log(\rho) \tag{2.17}$$

where $\rho = |\Gamma|$. Another commonly used expression to define antenna mismatch is the return loss, which is the inverse of the power reflection coefficient.

$$RL = -20\log(\rho) \tag{2.18}$$

Similarly, voltage standing wave ration (VSWR) is also used to represent the mismatch at the input port of the antenna [13]

$$VSWR = \frac{1+\rho}{1-\rho} \tag{2.19}$$

Table 2.1 provides a rough idea about the impedance matching at different values. One may easily interpret the quality of antenna by looking to at the table.

The conventional narrowband antenna represents its inherent property to radiate on a single frequency whereas controlling of wide impedance bandwidth is a very challenging task. Intelligent control of antenna geometry leads to wide impedance bandwidth. Therefore, UWB antennas are more dependent on design control, and selecting a desired performance is made possible by optimizing various parameters.

2.14.2 Radiation Pattern and Gain

The radiation pattern of an antenna is a graphical representation of its radiation properties as a function of space coordinates [83]. Antenna radiation is characterized by its directivity or gain in the frequency domain. The directivity is defined as:

$$D = \frac{U}{U_0} = \frac{4\pi U}{P_{rad}} \tag{2.20}$$

where U is the radiation intensity at a given direction from the antenna. U_0 is the radiation intensity averaged over all directions in a sphere and P_{rad} is the total power radiated by the antenna [83].

Table 2.1: Matching in terms of VSWR, LogMag S_{11}, and Power Loss (%) [13]

Match	VSWR	LogMag S_{11} (dB)	Power Loss (%); (dB)
Marginal	3.00 : 1	-6.0	25.0; -1.25
Good	2.00 : 1	-9.5	11.1; -0.511
Good	1.92 : 1	-10.0	10.0; -0.458
Excellent	1.50 : 1	-14.0	4.0; -0.177
Superb	1.22 : 1	-20.0	1.0; -0.043

The antenna gain is another important parameter that takes into consideration the antenna radiation efficiency e. As defined in 2.20, it is not included in the impedance and polarization mismatches. It is related to directivity as:

$$G = eD \tag{2.21}$$

The radiation patterns are normalized to an isotropic antenna, and therefore the values of directivity and gain are given in dBi.

2.14.3 UWB Radiation Efficiency

Radiation efficiency is the ratio of the total power radiated by an antenna to the net power accepted by the antenna from the connected transmitter [83].

$$e = \frac{P_{rad}}{P_{in}} = \frac{P_{rad}}{P_{rad} - P_{loss}} \tag{2.22}$$

where P_{loss} is the power loss in the antenna structure, P_{rad} is the radiated power and P_{in} is the input at the antenna terminal.

2.14.4 Mean Realized Gain

The mean realized gain (MRG) is defined as "evaluation of the radiation properties of a broadband antenna over a large frequency range with one single value". In order to better estimate the gain in one particular direction, MRG is calculated by using [13]:

$$G_m(\theta, \varphi) = \frac{1}{f_h - f_l} \int_{f_l}^{f_h} G(f, \theta, \varphi) df \tag{2.23}$$

where f_h and f_l are the lower and upper edge of frequencies, respectively. In the case of UWB antennas, the lower and upper frequencies points are 3.1 and 10.6 GHz.

Before discussing the analysis of time domain, it is important to understand the difference between frequency domain measurement and time domain measurement. Fig. 2.10 represents the same information in both the frequency and time domain. They each have their own measurement strength. Frequency domain is useful for analysing the harmonic content of a signal and it is extremely important for cellular radio systems interference with other systems operating at the same frequencies. Conversely, time domain measurements include pulse rise and fall times, ringing and distortion.

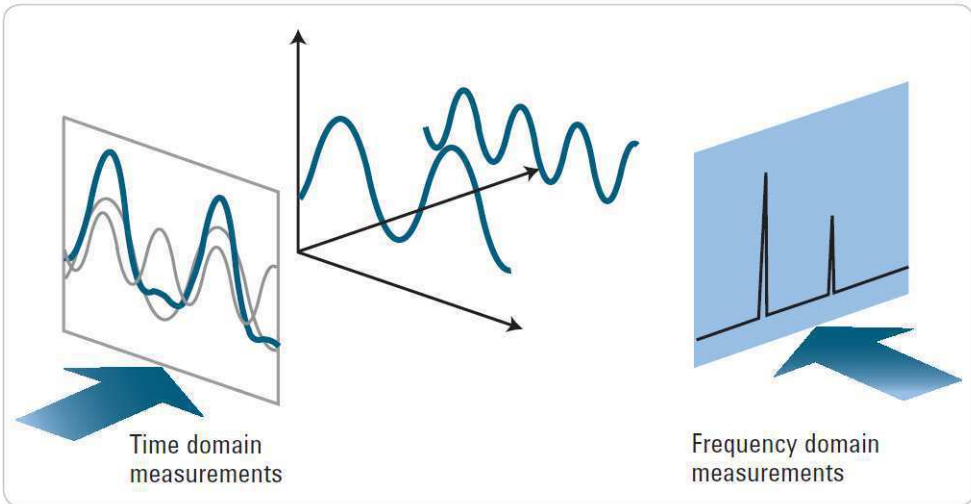

Figure 2.10: Relationship between time and frequency domain [10]

2.14.5 Fidelity Factor

There is no such concept of fidelity factor in narrowband antennas because they operate on a single frequency. Pulse distortion is practically not possible at single frequency. The concept of fidelity factor evolved with the usage of wideband frequencies. Due to a broad spectrum existing, there is more chances of dispersion while pulses are radiating. Transmission of these pulses in a multipath environment will lead to even greater dispersion. The dispersion produced by the environment is quantified by the term "Fidelity Factor".

To analyse the fidelity factor or correlation factor, pulse is used to excite the antenna. Fidelity factor is computed between input pulse and radiated pulses by using

$$\hat{R}_s(t) = \frac{R_s(t)}{\sqrt{\left[\int_{-\infty}^{\infty} |R_s(t)|^2 \, dt\right]}} \tag{2.24}$$

$$\hat{T}_s(t) = \frac{T_s(t)}{\sqrt{\left[\int_{-\infty}^{\infty} |T_s(t)|^2 \, dt\right]}} \tag{2.25}$$

This is done by placing some virtual probes located at a distance of 150 mm away from

the feed point of the DRA antenna; the corresponding E_θ components of the electric field intensity signals $R_s(t)$ were recorded.

Following the definition in [84], the degree to which the radiated-field waveform of a transmitting UWB antenna resembles the driving voltage can be quantified by the correlation factor, ρ. The radiated and transmitted pulses are normalized as shown in (4.1) and (2.25). This normalization was done in order to compare only the shape of the pulses, since $R_s(t)$ is expected to be much lower than $T_s(t)$:

$$\rho = \max_n \int_{-\infty}^{\infty} \hat{T}_s(t)\hat{R}_s(t+\tau)dt \tag{2.26}$$

where τ is the delay to maximize ρ in (2.26).

2.14.6 Group Delay

Group delay is commonly used to characterize two port devices. It measures the average delay between centre of transient input and output signal. This information is useful for finding the phase distortion of the antennas systems, and the dispersion of the transmitted signal.

The frequency dependent complex transfer function $H(\omega)$ (equivalent to the transmitted versus input signal) on an antenna system can be expressed as follows

$$H(\omega) = A(\omega)e^{j\phi(\omega)} \tag{2.27}$$

where A(ω) is the amplitude and $\phi(\omega)$ the phase response of the antenna.

The group delay is defined as the derivative of the phase response versus frequency.

$$\tau = -\frac{d\phi(\omega)}{d\omega} = -\frac{1}{360^o}\frac{d\phi(f)}{df} \tag{2.28}$$

The average of the group delay is the time taken to move the signal from one antenna to another. In other words, less deviation from the mean value in the entire operating band means that distortion is minimal, which is one of the key requirements of UWB systems.

2.14.7 Equivalent Isotropically Radiated Power (EIRP)

According to IEEE standard Definitions of Terms for Antennas [85], definition of EIRP is: "In a given direction, the gain of a transmitting antenna multiplied by the net power accepted by the antenna from the connected transmitter."

Another definition, particulary related to UWB systems, is explained by FCC in the Title 47 Part 15, subpart F (15.503) as follows: Equivalent isotropically radiated power, i.e., the product of the power supplied to the antenna and the antenna gain in a given direction relative to an isotropic antenna. The EIRP, in terms of dBm, can be converted to a field strength, in dBV/m at 3 meters, by adding 95.2. As used in this subpart, EIRP refers to the highest signal strength measured in any direction and at any frequency from the UWB device, as tested in accordance with the procedures specified in 15.31(a) and 15.523 of this chapter."

The EIRP value is obtained by

$$EIRP = P_t + G_t \tag{2.29}$$

where EIRP is given in dB, P_t is the power in dBm measured at the antenna terminal, and G_t is the antenna gain in dBi at a given direction.

2.14.8 Regulations

UWB can be used in radio technology if its frequency bandwidth is limited to 500 MHz or 20% of the mean centre frequency, according to Federal Communications Commission (FCC). In 2002, FCC allowed unlicensed use of extremely wideband spectrum ranging from 3.1- 10.6 GHz. The power spectral density emission limit for UWB entities is -41.3 dBm/MHz inside the UWB band. However, while these limits are only applicable in the USA, this was the first administrative ruling to define UWB terminology.

The UWB communication framework have been endorsed by several administrations

around the world since 2002. Europe and the Asia-Pacific region have also accepted the framework and conform to spectrum masks and operational conditions in order to protect existing radiocommunications services. However, the spectrum mask vary from country to country (especially United States and Europe) and they will be explained in more detail below.

United States

The United States was the pioneer in releasing a regulatory framework for open use of UWB technology. A number of compatibility studies were done to verify the impact of UWB emission with other sharing spectrum services.

The FCC's First Report and Order defined UWB transmitter in the following way [36]:

"An intentional radiator that, at any point in time, has a fractional bandwidth equal to or greater than 0.20 or has a UWB bandwidth equal to or greater than 500 MHz, regardless of the fractional bandwidth".

This spectrum is available from 3.1 GHz to 10.6 GHz with maximum power emission limit of -41.3 dBm/MHz, as shown in Fig. 2.11. This FCC spectrum allows open use of indoor or outdoor communication devices with allowed emission limits. These limits ensure unlicensed use of UWB that does not interfere with existing radio devices operating from 3.1-10.6 GHz. However, to provide additional protection to GPS devices, the FCC further restricted the emission power to -75 dBm/MHz between 0.96 GHz and 1.61 GHz.

Europe

The ETSI (European Technical Standard Institute) and CEPT (European Conference of Postal and Telecommunications Administration) are the two organizations which deal with radio frequency allocation. Following the FCC, Electronic Communications Committee (ECC) of the CEPT also regulates the framework of UWB communication for short range

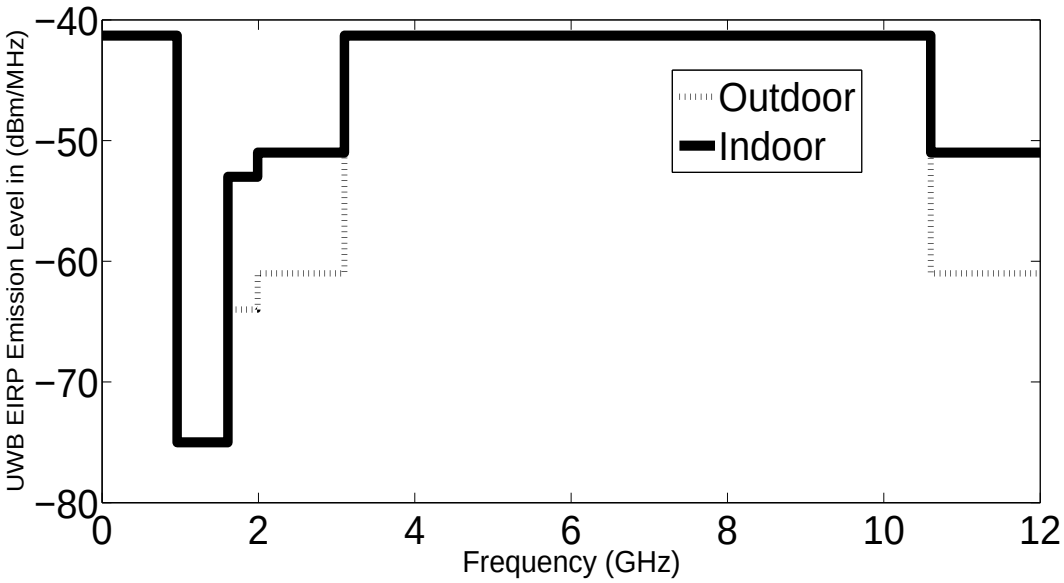

(a)

Figure 2.11: FCC mask for outdoor and indoor UWB applications in USA [11]

devices. It has imposed more strict regulations than the USA. The main focus of CEPT was to ensure UWB technology was used mainly for indoor communication devices in order to avoid interference. In addition, UWB transmitter must stop sending information if no acknowledgement is received in 10 seconds. The regulation also states that outdoor use of UWB technology should not be allowed for fixed outdoor locations or be connected to fixed outdoor terminals.

The first UWB regulation in Europe was published in 2007 and it laid laid out the final emission limit used for UWB communication. This regulation also makes provision for the utilization of mitigation techniques including low duty cycle and other operational conditions. In order to compare the FCC and ECC indoor mask, both EIRP limits are shown in Fig. 2.12. It is evident that EIRP regulation of ECC is more stringent than the FCC mask. The only common feature in both is that limits are from 6.0 GHz - 8.5 GHz.

Other than that the ECC emission level is far less than of the FCC, especially from 3.1 GHz to 10.6 GHz. Fig. 2.13 shows the spectrum allocation of different countries in the aforementioned frequencies.

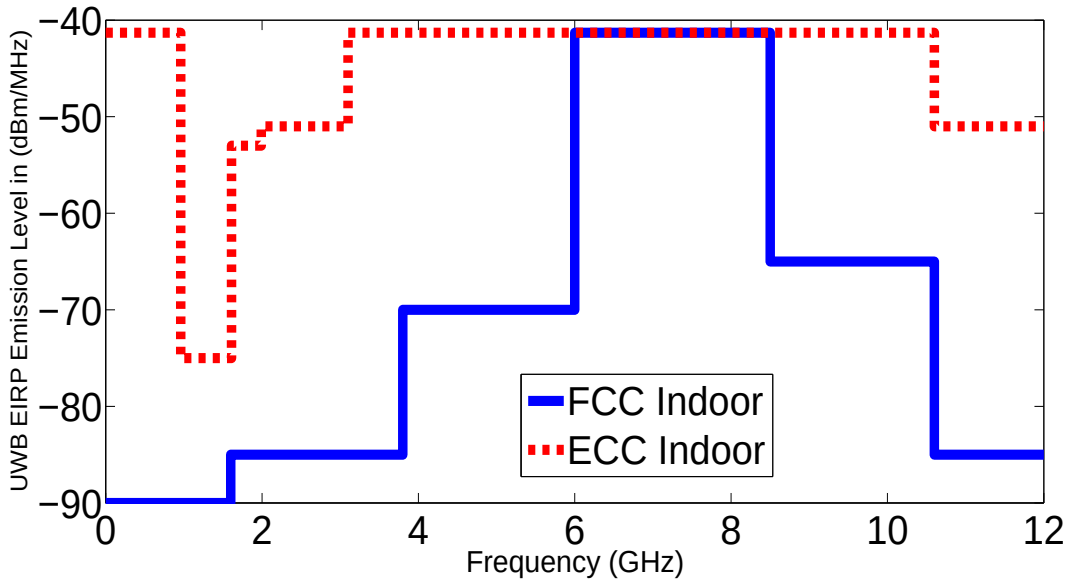

(a)

Figure 2.12: FCC and ECC masks for indoor UWB applications [11]

2.14.9 Standards

The use of the FCC approved UWB band (3.1 to 10.6 GHz) reduce the usage of crowded 2.4 GHz band. Compared to Bluetooth, Wi-Fi and digital enhanced cordless telecommunications (DECT) phone technology, UWB technology significantly minimises interference from the other systems. The main advantage of UWB band is that it can be used without needing any approval and therefore it is free. UWB systems operating in the UWB band have a larger bandwidth compared to the other systems.

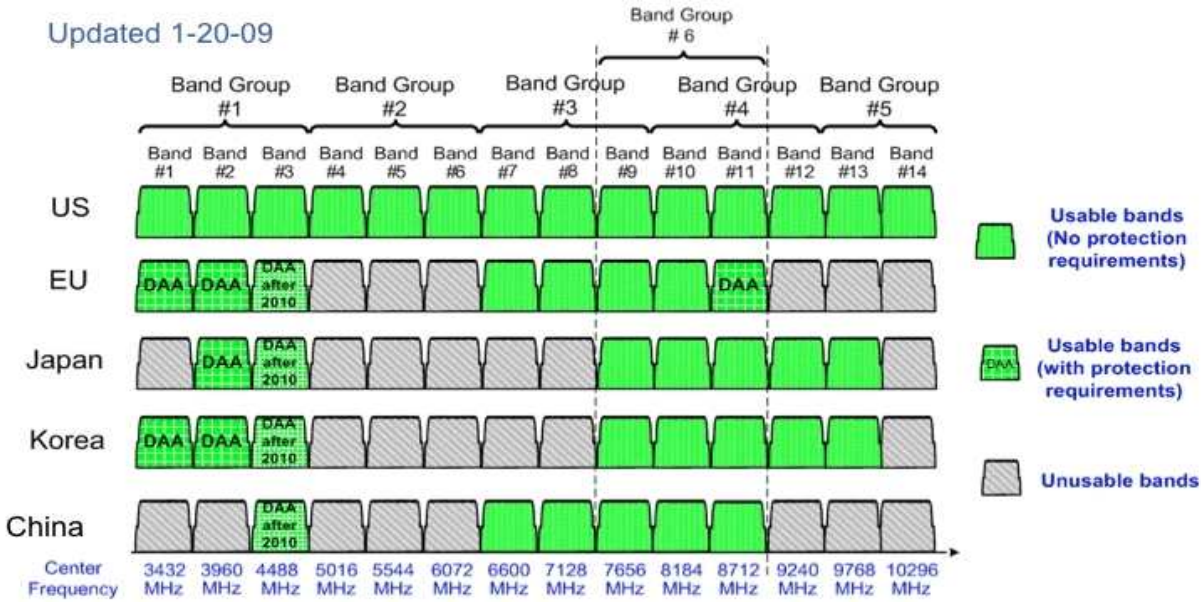

(a)

Figure 2.13: Spectrum allocation in the 3.1 to 10.6 GHz band [12]

2.14.10 Power Consumption

Low power consumption and long battery life are essential parameters for all portable battery-operated electronic devices. However, circuitry's complexity and its software play a pivotal role in increasing the power consumption. Conversely, UWB-enabled electronic devices have the lowest power consumption compared to IEEE 802.11 g and IEEE 802.11n standards. The range of these standards is less than 50 mm and maximum throughput for later standard is greater than 100 Mbps.

The power consumption for UWB is 1 mW/Mbps which is substantially less than IEEE 802.11 g (15-20 mW/Mbps) and IEE 802.11n (6-7 mW/Mbps) standards [81].

2.15 Advantages of UWB

In today's market, UWB communication applications play an active role because they have various advantages. These are useful for the antenna engineer and the consumer. Below are the major advantages which make the UWB system unique compared to other radio systems.

- There is no need for additional RF mixing stage for UWB transmitter and this reduces the complexity of circuitry and cost;
- Less interference between impulse radio and existing radio systems enables the UWB system resistant to resist multipath and jamming;
- UWB transmitted signal has a noise-like spectrum, unique timing code, and low spectral density and these traits unintended detection difficult;
- Time-domain signal has a much better resolution for finding the location and tracking of an application; and
- High speed, large bandwidth, high processing gain are inherent advantages of the UWB system.

2.15.1 UWB Application

Recent research studies reveal expanded use of UWB technology due to the above-mentioned advantages. UWB technology is mainly categorized into three different areas: communication, radar, and positioning. In order to account for all the applications, below are the major applications which are essential UWB facets of technology:

- Radar imaging systems

  - Ground penetrating radar systems
  - Wall radar imaging systems
  - Surveillance systems
  - Medical systems

- Vehicular radar systems
- UWB measurement systems
- UWB communication systems

UWB characteristics for medical applications

We are well aware that UWB technology transmits very short pulses and therefore its spectrum has the capacity to send 10 Gpbs speed. It is very useful application for short-range high-data-rate communication applications [86, 87]. These characteristics of UWB technology do not require any IF processing because it is processing on baseband. This feature of UWB communication is highly desirable for medical applications. Some of the major medical applications which apply UWB technology are: penetrating through obstacles; high precision ranging at the centimetre level; low electromagnetic radiation; and low processing energy consumed.

Applications of Ultrawideband Medical Engineering

Due to the characteristics we have discussed in the previous section, UWB technology is ideal for medical applications, for example, medical monitoring and medical imaging [88–91].

Firstly, due to highly intense pulses used in UWB technology, it is possible to monitor the patient's motion in over a short distance. Moreover, it can be used to monitor the

patient remotely. For instance, monitoring function can be applied to intensive care units, emergency room, etc.

Secondly, UWB technology has a great potential in medical imaging. The transmission of very short pulses to the human body and the reflected pulses from the area under monitoring, such as heart, arrived at UWB receiver and then results is recorded. After extensive signal processing of these recorded pulses, the impedance difference between the input pulse and received pulse represents the status of the heart. Similarly, we can examine the respiratory pattern, dynamic chest diameters measurement, allergy and asthma crisis monitoring, chest imaging, obstetrics imaging, and ear-nose-throat imaging.

Some of the other medical application are of UWB are: space medicine measurements; sport medicine measurements; military medicine; and underwater medicine measurements.

2.16 Summary

This chapter described the DRAs in details by highlighting their basic characteristics, shapes of different dielectric materials and the merits of employing DRAs in ultrawideband communication. Then the chapter explained DRA and its working principle regarding how it has achieved a wide impedance bandwidth capabilities. Moreover, the fundamental mode was explained with reference to understanding DRAs' Q-factor. Later on, various feed structures, coaxial probe and microstrip line, were presented in order to use them with DRAs. Furthermore the chapter highlighted the MSDRA and discussed different methods to enhance its impedance bandwidth. Compactness and size reduction of DRA were examined in order to reduce the antenna's volume.

In addition, a brief historical introduction on ultrawideband technology has been documented, followed by the FCC's pivotal contribution to the proper employment of ultrawideband systems. The spectral and temporal domain methods to characterize UWB

antennas are described in greater detail in this chapter. A summary of the standards, in relation to the parameters used in the dissertation, is presented. Moreover, UWB's regulations are discussed and compared. Finally, UWB applications and their advantages are discussed where UWB technologies since 2002 have offered benefits in areas of research and practical interest.

Chapter 3

Dielectric Resonator Antenna for UWB Systems

This chapter provides an in-depth analysis of a new ultrawideband (UWB) dielectric resonator antenna (DRA) in the frequency domain. This DRA consists of a lower-permittivity insert (LPI) and a sliced dielectric resonator (DR), which reside on the ground plane in a stacked arrangement. An air region is introduced inside the DR to improve the antenna's impedance bandwidth. This chapter also examines the effect created by the air-region dimensions and the ground-plane dimensions on the impedance bandwidth of the antenna. Additionally, other characteristics such as radiation pattern and antenna gain are computed to analyse the radiation performance of the antenna.

The main objective in designing a compact UWB DRA is to fully utilize UWB band. Since 2002 the release of an UWB spectrum by the Federal Communication Commission (FCC) of USA [92] has created new opportunities for wireless applications. These include, for example, high-speed wireless personal area networks, cognitive radios, radars, pulse-based microwave imaging and next-generation networks, which operate in the UWB band and require a broadband antenna. Consequently, there is a great demand for antennas

with extremely wide bandwidth.

In this chapter a novel DRA design is presented for UWB applications. This UWB DRA represents a significant improvement in impedance bandwidth when compared to the design presented in [55, 58, 93, 94]. Furthermore, both of the above-mentioned limitations, in the previous UWB antennas, are addressed in this antenna. A rigorous analysis of this UWB DRA is described in the next section.

3.1 UWB DRA: Design and Analysis

A finalised antenna configuration is described in the first subsection. In the second subsection, an extensive investigation of the air region and the ground plane are presented to verify the effect on computed results. In particular, a tetrahedron-shaped air region which is intentionally created inside the DR, to enhance the impedance bandwidth of antenna, is analysed rigorously to achieve a good return loss bandwidth in the entire UWB band. In the third subsection, theoretical validation of the design is conducted. Lastly, a prototype of the UWB DRA is described and its measured and computed results are compared and analysed.

3.1.1 Antenna Configuration

The geometry of the new UWB DRA is illustrated in Fig. 3.1. The LPI resides on the ground plane, and the DR is attached to the LPI. A tetrahedron-shaped air region is introduced to the DR to reduce the effective permittivity of antenna. The DRA is fed using the inner conductor of an SMA connector as a probe, which protrudes through a small hole in the metallic ground plane, as shown in Fig. 3.1(b). Small holes are drilled inside the LPI and the DR to accommodate the feed probe. HFSS and CST Microwave Studio software were used to fine-tune the probe position (s_1 and s_2 in Fig. 3.1) and probe

length (h). The purpose of acquiring results from two different softwares are to validate the results before fabrication the antenna. It is found there is a slight difference in results from these softwares. The major reason is due to different size of meshing considered in the above-mentioned softwares. In addition, image theory is used to reduce the length of the antenna by approximately 50%. A conducting wall, applied to one side, creates a quasi-image for this purpose. The DRA is 15 mm tall, 12 mm long, and 8 mm wide and it is supported by a 40×40 mm^2 ground plane. The materials selected for the DR and LPI are TMM10 and RT/Duroid 5880, whose dielectric constants are 9.2 and 2.2, respectively.

In this section, starting from the preliminary analysis reported in [95], the compact DRA is further investigated to enhance its return loss bandwidth for the UWB band. Based on the DRA's basic characteristics, impedance bandwidth is inversely proportional to the Q-factor. The idea is to introduce an air region inside DR to reduce the effective permittivity of the antenna, and subsequently lead to wide impedance bandwidth. However, the formation of the air region inside DR needs to be further investigated so that contiguous impedance bandwidth in the UWB band can be achieved.

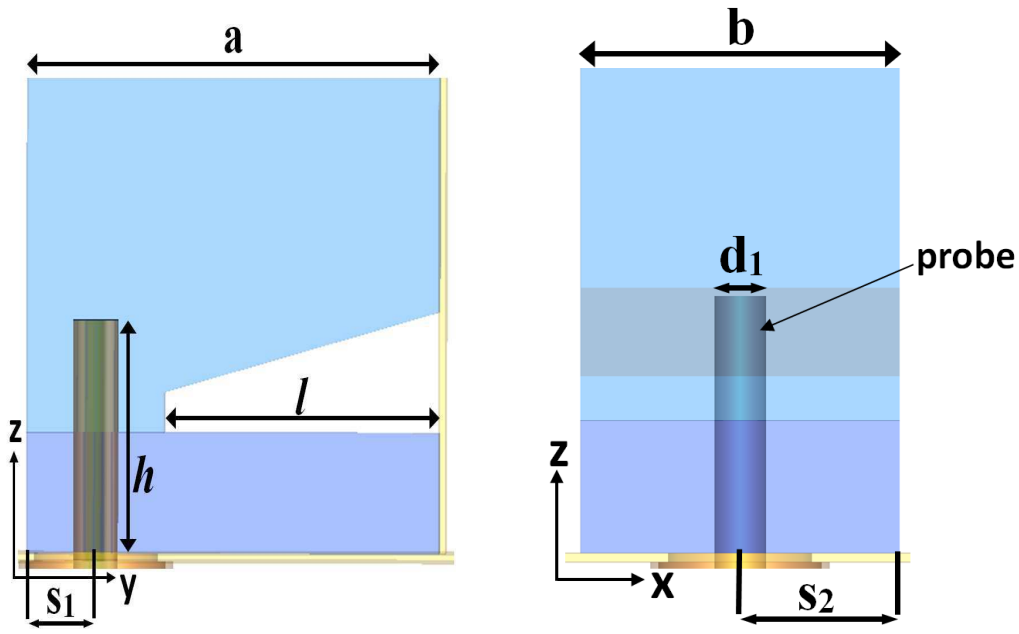

(a)

(b)

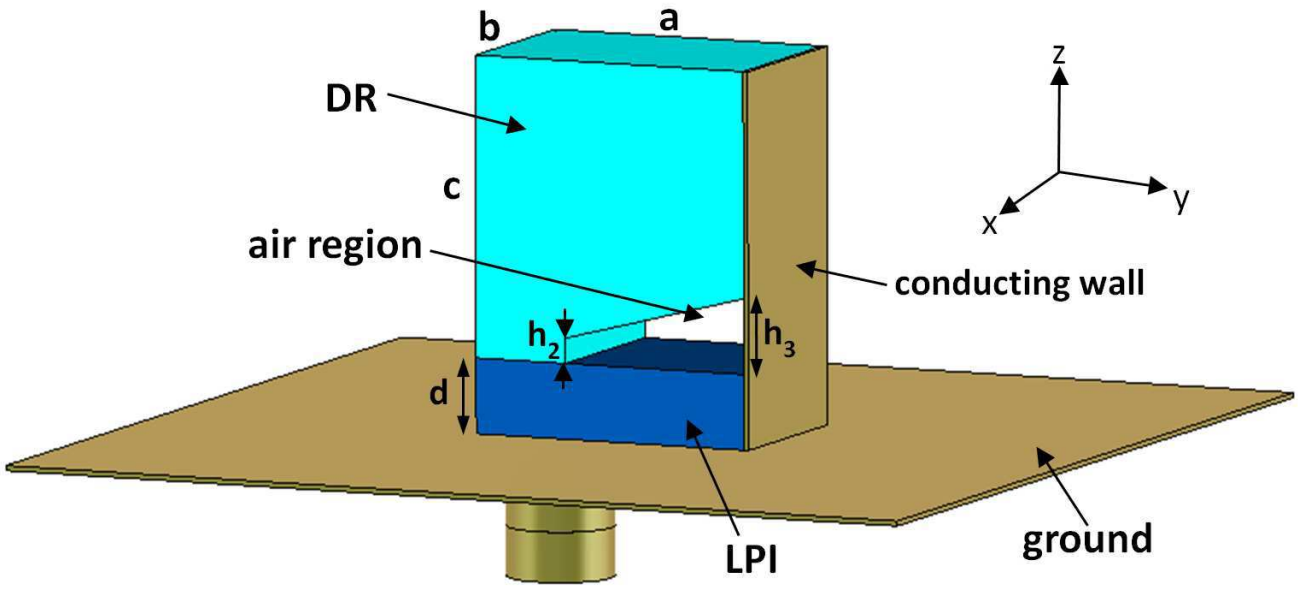

(c)

Figure 3.1: Ultrawideband dielectric resonator antenna configuration

3.2 Parametric Study

In this section, a detailed parametric study was executed to analyse the results of this UWB DRA by varying the following design parameters: placement of ground plane and conducting wall; the air region in the UWB DRA; and the dimension of the ground plane. The corresponding response for each of the above situations is presented and discussed in more detail below.

3.2.1 Ground plane and Conducting wall

Fig. 3.1 illustrates that the UWB DRA is placed on the ground plane. The placement of the ground plane validates the concept of image theory and therefore volume of an antenna can be reduced to half. The boundary conditions at the ground plane and the DRA interface require that the electric fields will be normal to the conductor, while magnetic fields will be tangential. An orientation of the electric fields in a cross-sectional view of the full-volume rectangular DRA and half-volume DRA, are shown in Fig. 3.2(a) and (b), respectively. Analogously, a conducting wall to one side of the half-volume dielectric block behaves as a mirror and creates a quasi-image of the half-volume dielectric block, effectively doubling the length of the DRA. Fig. 3.3 shows the comparison of computed return loss bandwidth of full-volume DRA and half-volume DRA. It can be seen that adding a metallic wall to half-volume DRA significantly improves input matching at lower band of frequency. Although half-volume DRA has a mismatch at 10 GHz, it can be improved by reducing the permittivity of DRA (by adding optimised air-region inside the DRA).

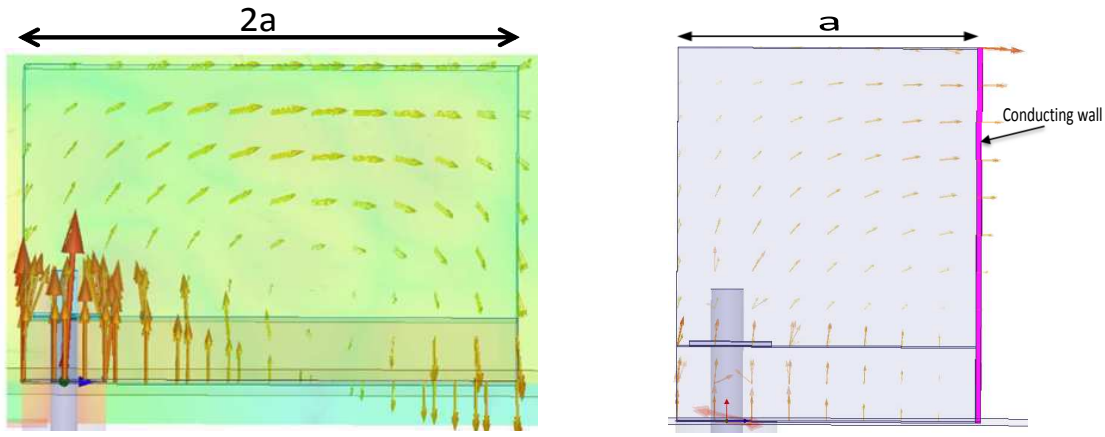

(a) DRA without conducting wall (b) DRA with conducting wall

Figure 3.2: Application of the shortening conducting wall to reduce volume: (a) a full-volume DRA; (b) a half-volume DRA with finite conducting wall on one face

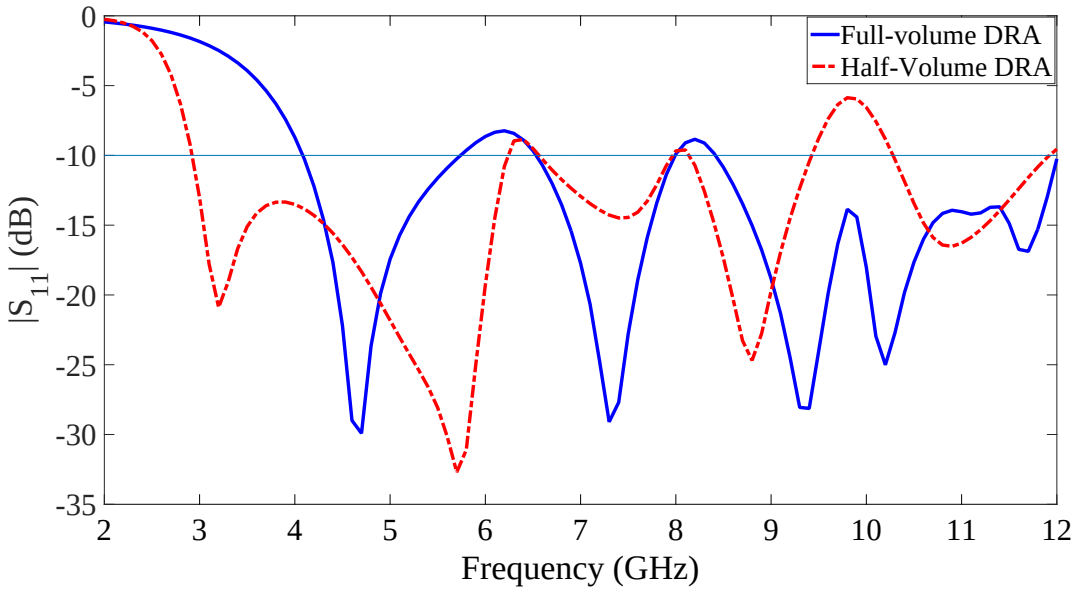

Figure 3.3: Return loss bandwidth of full-volume DRA and half-volume DRA

3.2.2 Air-Region Optimization

Studies on the effect of introducing the air regions have found that a significant change in the resonant frequency and Q-factor can occur, especially if the dielectric constant

of the DRA is relatively high [21, 39, 96]. The introduction of the air region inside DR significantly reduces the Q-factor of the antenna and increases the resonance frequency, which results in an improved impedance bandwidth. Furthermore, the air region changes the input impedance of the DRA, and therefore air gap can be used to better match the impedance of the DRA to that of the feed [46].

Based on the studies mentioned above, an arbitrary-shaped air region is introduced inside the UWB DRA to minimize the antenna's effective permittivity. Several computations have been done by creating air region at different antenna locations to observe the frequency response. Those locations include: a) air region between the ground plane and the LPI, (b) air region between the LPI and the DR (c) air region inside the upper position of the DR and (d) air region inside DR and LPI . It was found that at location *'a'*, *'c'* and *'d'*, the antenna has a return loss less than 10 dB at a number of frequency points over the entire FCC UWB band.

On the other hand, the location of an air region between the LPI and the DR (location *'b'*) showed significant improvement in return loss bandwidth compared to the latter locations. Although location *'d'* almost covered entire UWB, due to instability of structure it is not considered in the following investigations. Therefore, location *'b'* is used to estimate the precise location and shape of the air region to obtain a contiguous 10 dB return loss bandwidth. Due to this reason, only the optimization of the air-region dimensions has been extensively examined. To investigate the effects of the air region on DR, a parametric analysis was carried out by sweeping l, h_2, and h_3 respectively. After exploiting these parameters, optimized values have been chosen.

Fig. 3.4 shows the effect of the length l, starting from the conducting wall to near the probe feed, on the reflection coefficient for the UWB DRA. It can be seen that UWB DRA shows a slight variation in the reflection coefficient magnitude results regardless of the variation of l from 3 mm to 9 mm. It is noted that there is a minimal mismatch at

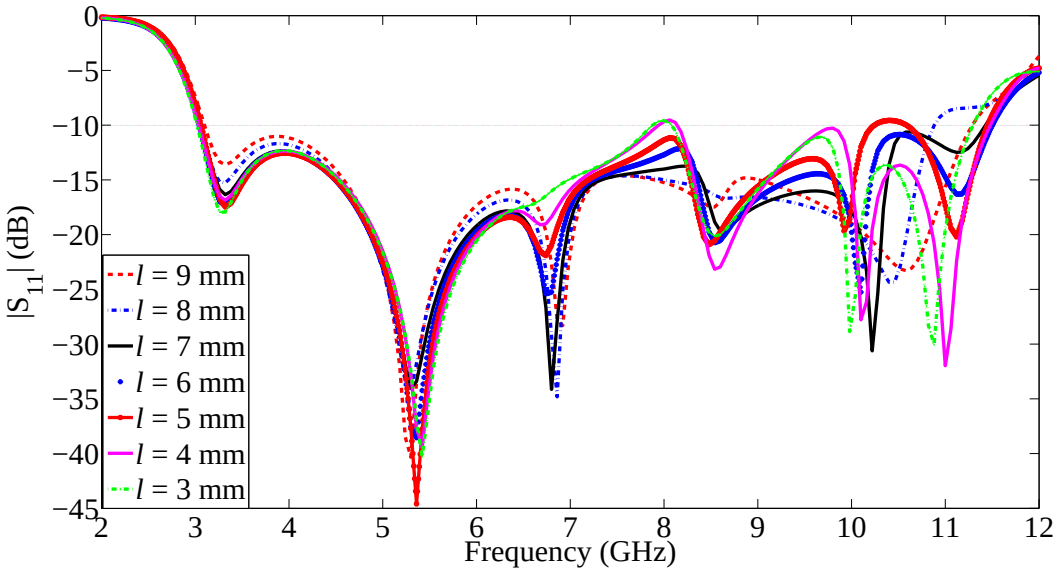

Figure 3.4: The effect of the air region on input reflection coefficient; h_2= 1 mm, h_3 = 3 mm

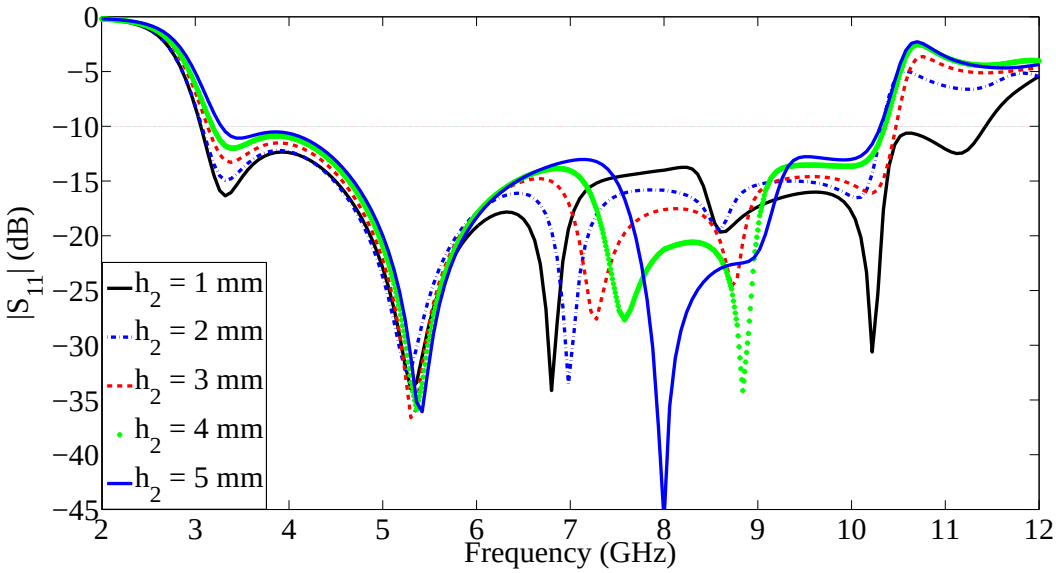

Figure 3.5: The effect of the air region on input reflection coefficient; h_3= 3 mm, $l = 5$ mm

8.0 GHz and 10.2-10.6 GHz for l = 3-4 mm and l = 5 mm, respectively.

Furthermore, sweeping l from 6 mm to 9 mm shows good input matching at the above-mentioned frequency points. However, the impedance bandwidth for l = 8 mm is limited up to 10.8 GHz whereas l = 7 mm shows the best input matching from 3.1 - 11.7 GHz, while the other two parameters are kept constant.

The air region is further analyzed by carrying a parametric sweep of h_2 from 1 mm to 5 mm. As shown in Fig. 3.5, h_2 represents the height of the air region near to the probe feed. The reflection coefficient magnitude of the UWB DRA has the widest bandwidth from 3.1-11.7 GHz at h_2 = 1 mm, as indicated in Fig. 3.5. However, increasing the air region from h_2 = 2 mm to h_2 = 5 mm leads to a deterioration in the input matching at the frequencies' lower and upper band. As a result, h_2 = 1 mm is used in final design of the UWB DRA

Lastly, the third parameter h_3 is analyzed by varying the height from 1 mm to 7 mm, as shown in Fig. 3.6. The variation in h_3 from 4 mm to 7 mm degrades the resonance at high frequencies. However, a return loss bandwidth has widened at the upper band while changing h_3 from 1 mm to 4 mm. Therefore, h_3 = 3 mm is selected for both computational and measurement experiments. The optimization of the air region inside the DR has been computed using three variables. The results clearly indicate that h_3 has a maximal effect on the $|S_{11}|$. Therefore, in order to understand the physical insight of the h_3 parameter, input impedance magnitude is computed by sweeping h_3 = 2 mm to 7 mm and comparing the results with DRA without an air region.

This variation in h_3 changes the input impedance of the DRA and it is used as a technique to improve input matching. As can be seen in Fig. 3.7, antenna input impedance magnitude ($|Z_{11}|$) has the minimum variation for h_3 = 3 mm, which will potentially lead to the widest bandwidth. For this study, h_2 and l were kept constant. Fig. 3.8 compares input matching of a DRA without an air region and that of a DRA with the optimal

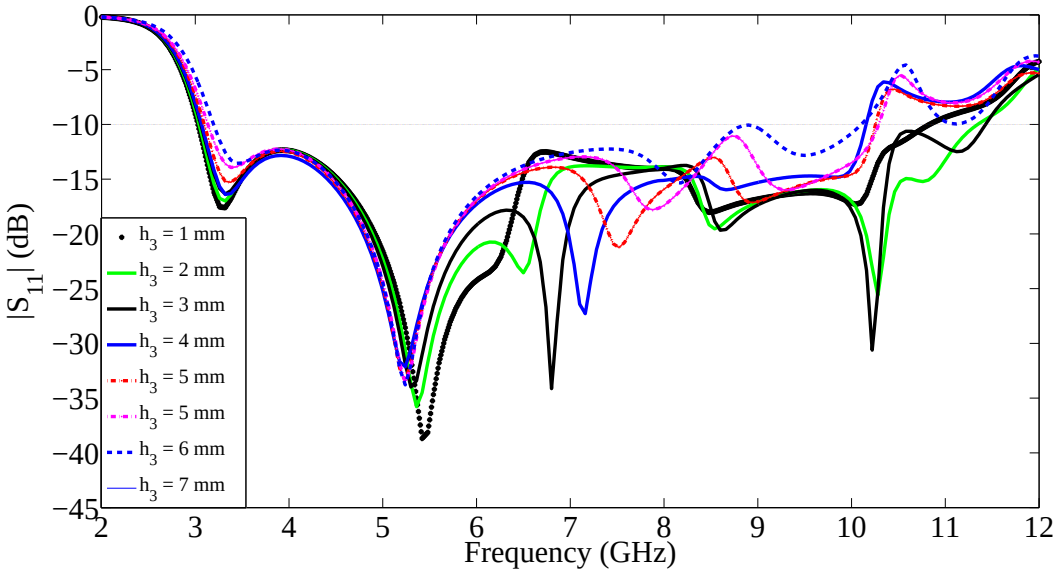

Figure 3.6: The effect of the air region on input reflection coefficient;h_2= 1 mm, $l = 5$ mm

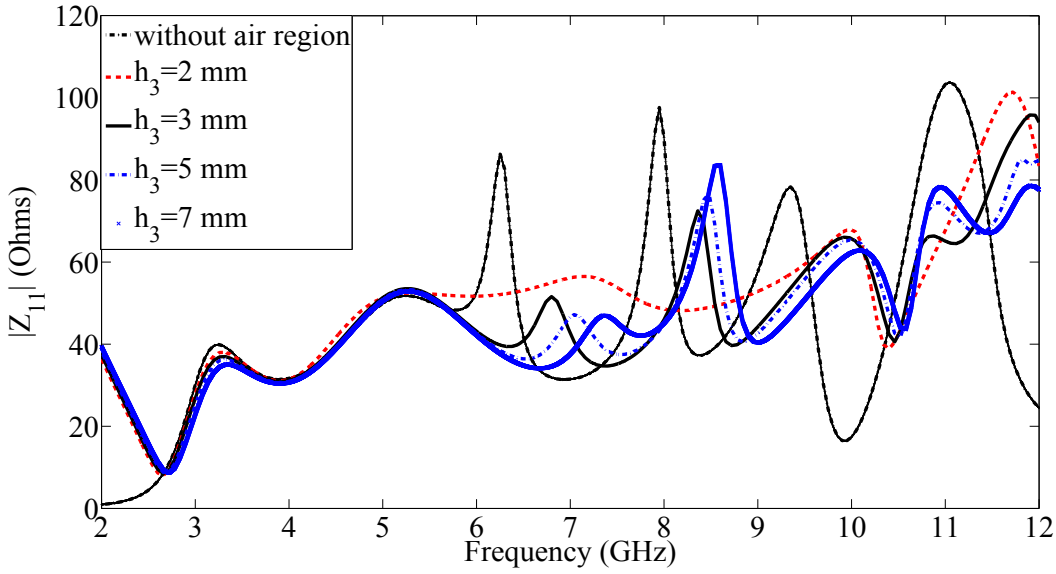

Figure 3.7: The effect of the air region on antenna input impedance; $l = 5$ mm, $h_2 = 1$ mm

tetrahedron-shaped air region ($h_3 = 3mm$). It can be seen that at 6.38 GHz, 8 GHz, and from 9.43 to 10.27 GHz, this air region helps to improve matching significantly. Hence impedance bandwidth is also improved.

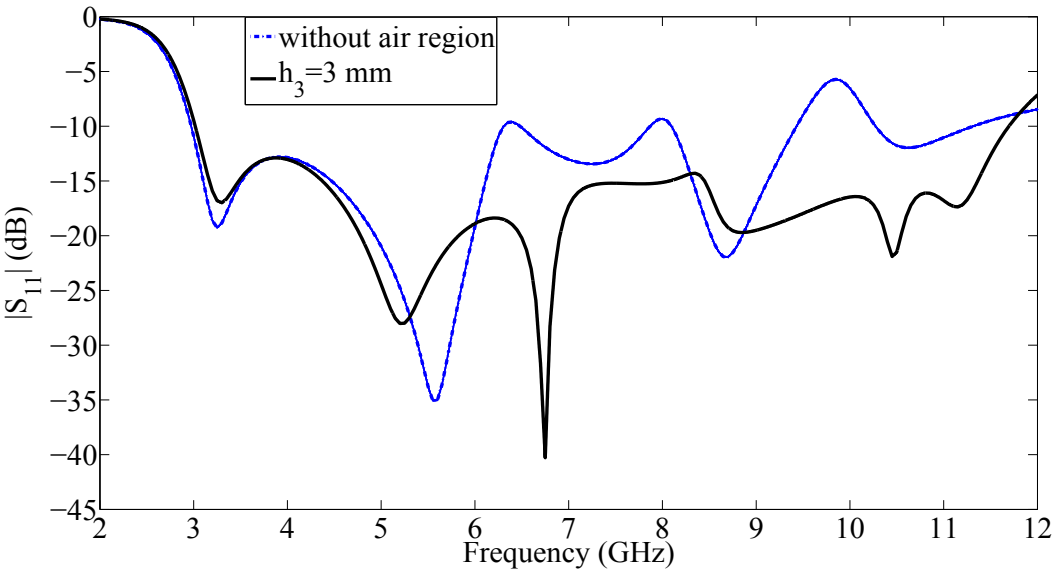

Figure 3.8: The effect of the air region on input reflection coefficient; $l = 5$ mm, $h_2 = 1$ mm

3.2.3 Ground Plane Effect

Most of the UWB planar antennas do radiate in both directions, however, many electronic devices need the antenna to be unidirectional. This means that half of the radiated power is wasted in unwanted directions. In contrast, the UWB DRA has a full ground plane which is used to direct the radiated power in the upper hemisphere, minimizing the radiated power in the lower hemisphere (unwanted directions).

In order to examine the full ground plane with the UWB DRA, Fig. 3.9 shows the reflection coefficient of UWB DRA by changing the ground-plane dimensions. The length

and width of the ground plane (G_l) are swept from 20 mm to 40 mm whereas both h_2 and h_3 of air region are kept constant. It is illustrated in Fig. 3.9 that for all ground plane sizes larger than 25 x 25 mm^2, the antenna has a return loss greater than 10 dB over the entire FCC UWB band. With 20 x 20 mm^2 ground plane, return loss is slightly below 10 dB between 3.5 and 4.5 GHz. In this investigation, it was found that increasing the size of the ground plane from 40 mm to 100 mm exhibits contiguous impedance bandwidth. These results show that the ground plane has a nominal effect on the impedance bandwidth greater than 25 x 25 mm^2.

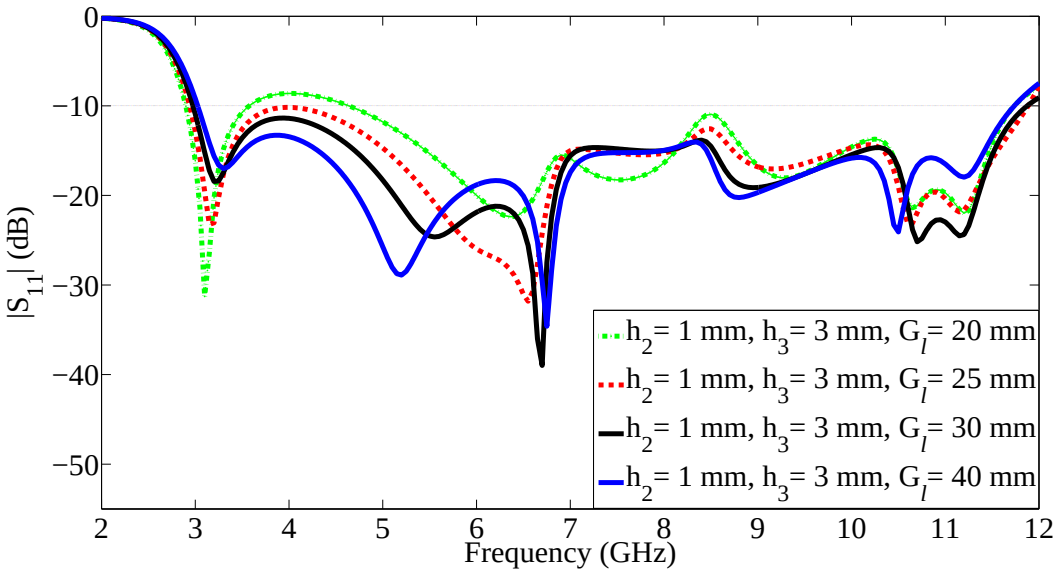

Figure 3.9: The effect of the ground plane on input reflection coefficient

In addition, in another investigation,a rectangular-shaped ground plane is employed to a UWB DRA. Fig. 3.10 shows the input matching of two ground plane sizes ($G_x = 16$ mm, $G_y = 20$ mm and $G_x = 20$ mm). It is evident that input matching is significantly disturbed at lower frequencies (3.1-5.5 GHz) by using the rectangular ground plane. Similarly, a circular-shaped ground plane is used to examine the effect on input matching of UWB DRA. It can be seen from Fig. 3.11 that reducing the ground plane's size less than 20

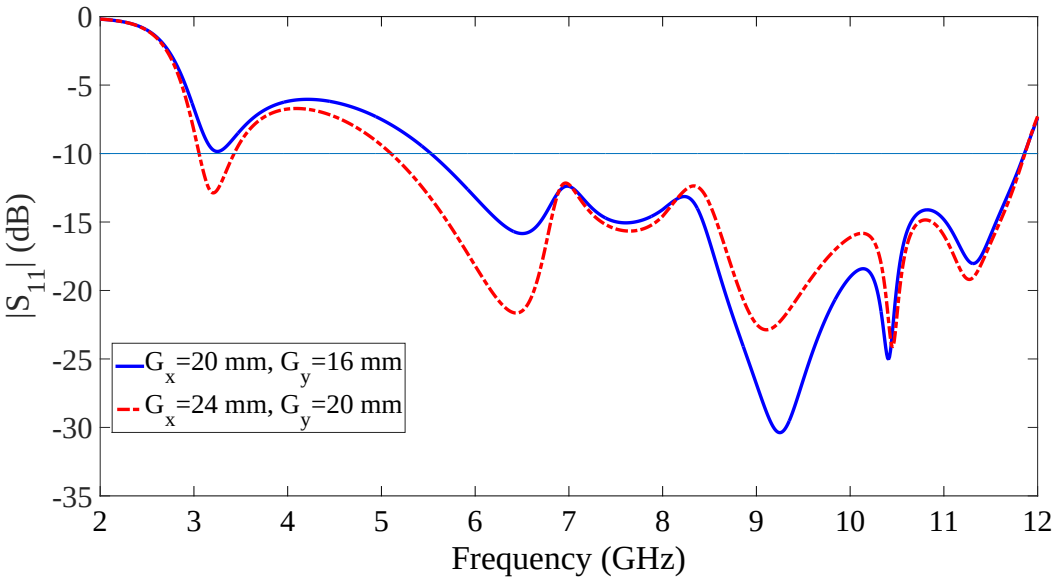

Figure 3.10: The effect of rectangular-shaped ground plane on input reflection coefficient

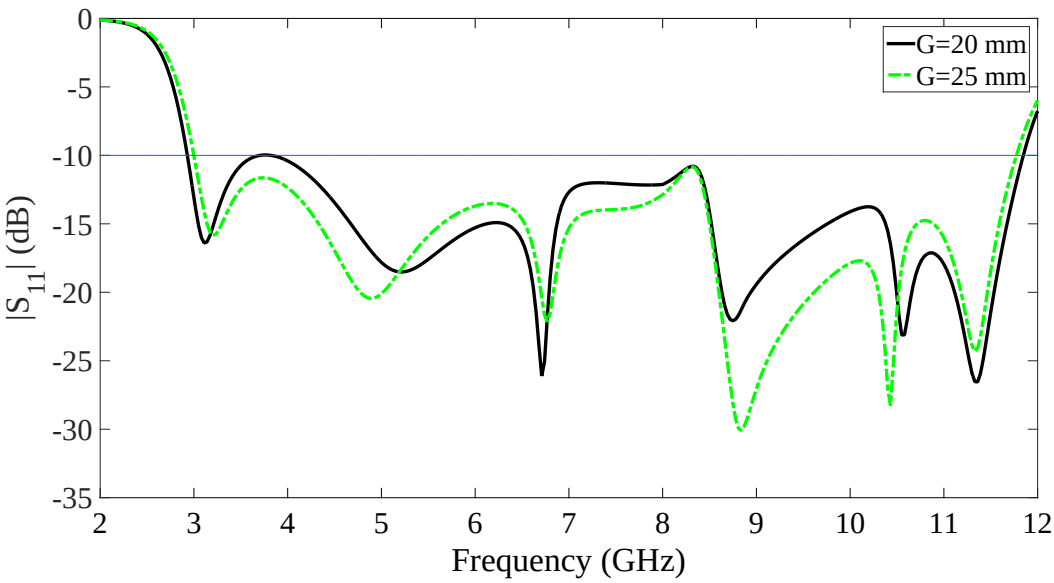

Figure 3.11: The effect of circular-shaped ground plane on input reflection coefficient

mm deteriorates the impedance bandwidth at 3.7 GHz.

It also emerged that this is a reasonable ground plane (40 x 40 mm^2) even at the lower frequencies. Even at the lowest frequency of 3.1 GHz, it gives a reasonable front-to-back

ratio greater than 7 dB and the percentage of power radiated into the upper hemisphere at 3.1 GHz is 87%.

3.3 Theoretical Validation of Resonant Frequency

Although tetrahedron-DRA is a UWB antenna, theoretical computation is performed in order to obtain the resonant frequency of the DRA. This information can be useful for other type of DRAs in which it is difficult to predict the initial dimensions of wideband antenna.

For a rectangular DRA with a dielectric constant of ϵ_r and dimensions a, b and c, mounted on a perfect infinite ground plane, the resonant frequency can be predicted using the following transcendental equation [59]:

$$k_x \tan(\frac{k_x b}{2}) = \sqrt{(\varepsilon_r - 1)k_0^2 - k_x^2} \tag{3.1}$$

where

$$k_0 = \frac{2\pi f_0}{c}, k_y = \frac{m\pi}{a},$$
$$k_z = \frac{n\pi}{c} \;\; and \;\; k_x^2 + k_y^2 + k_z^2 = \varepsilon_r k_0^2$$

Table. 3.1 show the calculated resonant frequency of the rectangular DRA. It should be noted that the dielectric waveguide model (DWM) does not take into account the actual excitation source, effect of the ground plane, LPI, and the effect of air region. Therefore it can only be used to estimate the resonant frequency of the antenna. The value of $a = 24$ mm was used to theoretically compute the resonant frequency, however the actual size of the antenna is half due to use of conducting wall on the side of the antenna.

Table 3.1: Theoretical Resonant Frequency of the UWB DRA

ϵ_r	a (mm)	b (mm)	c (mm)	Resonant Frequency (GHz)
9.2	24	8	12	6.85

3.4 Prototype Design and Measured Results

A prototype, as shown in Fig. 3.12, was fabricated. The tetrahedron-shaped air region was precisely cut off the DR, using computer controlled engraving machine at Macquarie Engineering and Technical Services (METS), to avoid undesirable changes in Q-factors and resonance frequencies [97]. In addition, it has been found that slightly excessive drilling of the ground plane when making the hole for the probe has a significant effects on measurements. Similarly, a thin air gap between the feed and the DR has a significant effect on the measured results. Therefore, the ground plane should be appropriately attached to the LPI to minimize impedance mismatch at lower frequencies. Further, if the copper tape, which is used as a conducting mirror, is not properly bonded to the DR, LPI and ground plane, an undesirable air gap will be formed that could compromise antenna operation at higher frequencies [39].

3.4.1 Input Matching

The voltage standing wave ratio (VSWR) was measured using a N5242A Vector Network Analyser. The measured and predicted VSWR values of the antenna are shown in Fig. 3.13. The predicted VSWR bandwidth (VSWR < 2) is 118%, i.e from 3.0 to 11.8 GHz and the measured VSWR bandwidth is 115%, i.e from 3.1 to 11.6 GHz. The measured VSWR agrees well with the predicted values. Minor discrepancies between the two are attributed to fabrication tolerances including possible air gaps between the different materials.

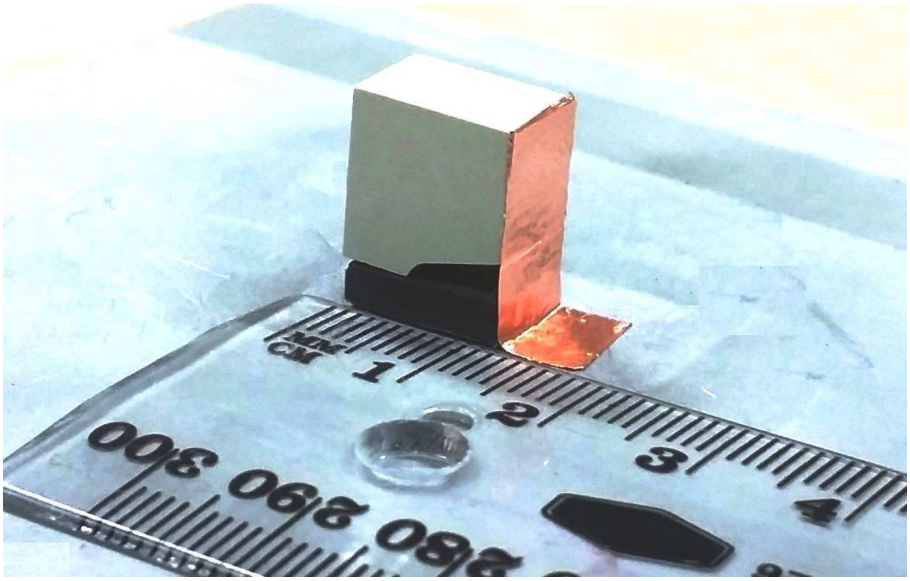

Figure 3.12: A prototype of the UWB dielectric resonator antenna

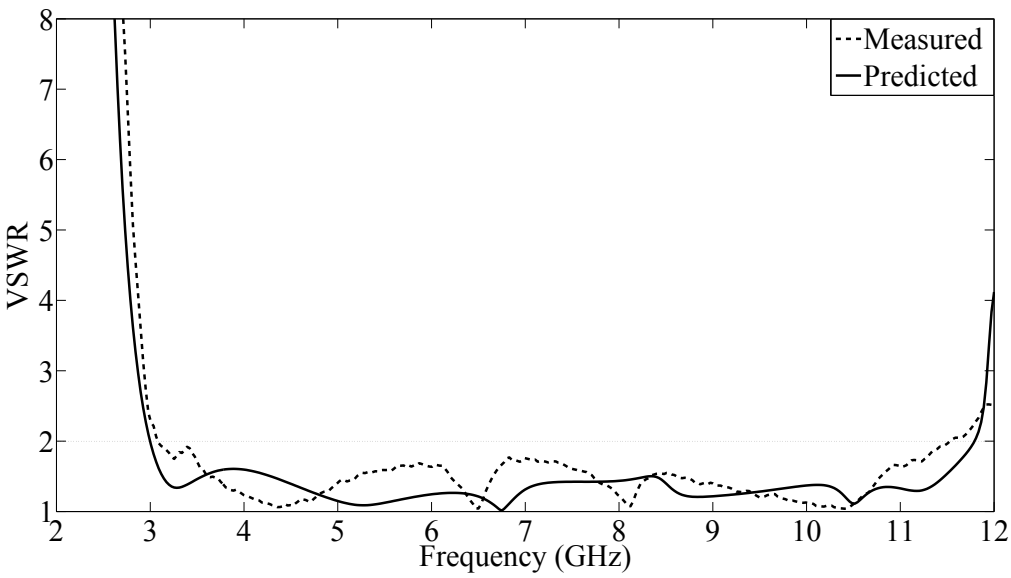

Figure 3.13: The effect of the air region on input reflection coefficient

3.4.2 Gain and Radiation Patterns

The gain and radiation characteristics were measured in the NSI-700S-50 spherical near-field measurement system at the Australian Antenna Measurement Facility (AusAMF).

The peak realized gain of the DRA, measured from 2 to 12 GHz, is shown in Fig. 3.14. The measured gain varies between 4.9 and 7.05 dBi across the operating frequency band. Such a variation is common in UWB antennas. In addition to this, Fig. 3.15 shows the realized gain computed in some favorable directions, in upper hemisphere ($-90^o \leq \theta \leq 90^o$), and it is found that the average realized gain is in between 3.6 dBi and 5.22 dBi. Another parameter which is useful to assess the gain of UWB antennas is mean realized gain (MRG). The mean realized gain (MRG) of the DRA [13], computed from 2 to 12 GHz, is shown in Fig. 3.16 in polar form. The computed MRG has a maximum value of 4.85 dBi and 4.91 dBi in XZ and YZ planes, respectively. The larger fluctuation of MRG in the YZ plane is due to the asymmetry of the structure.

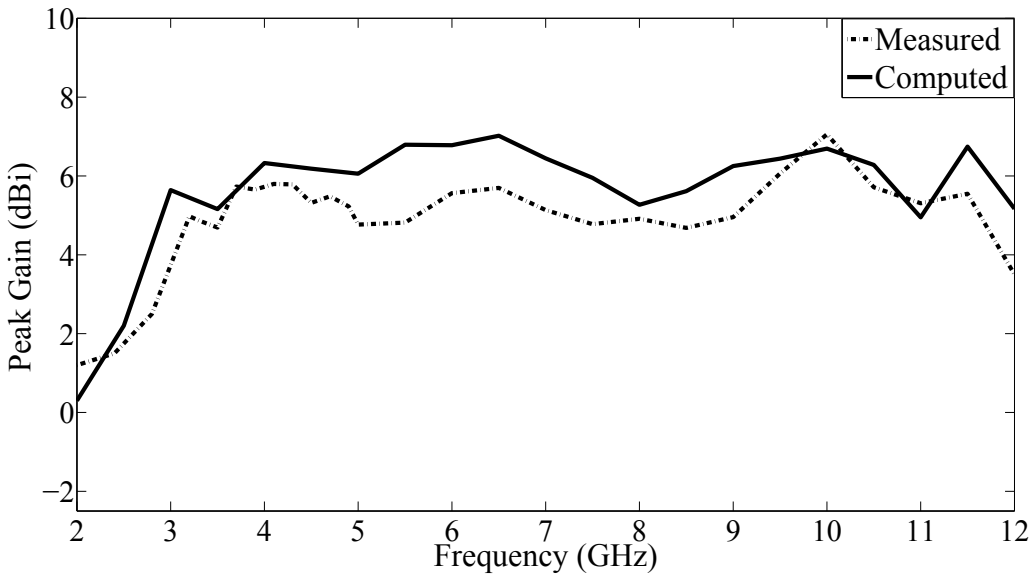

Figure 3.14: Measured and predicted realized peak gain of the UWB DRA

Fig. 3.17 and Fig. 3.18 show the computed and measured radiation patterns, respectively, in XZ and YZ planes at 3.3, 6, and 10 GHz. It is clear that this DRA radiates reasonably well in all directions in the upper hemisphere. When one polarization component is weak (e.g., E_θ in $\theta = 0^o$ direction), the orthogonal component is sufficiently

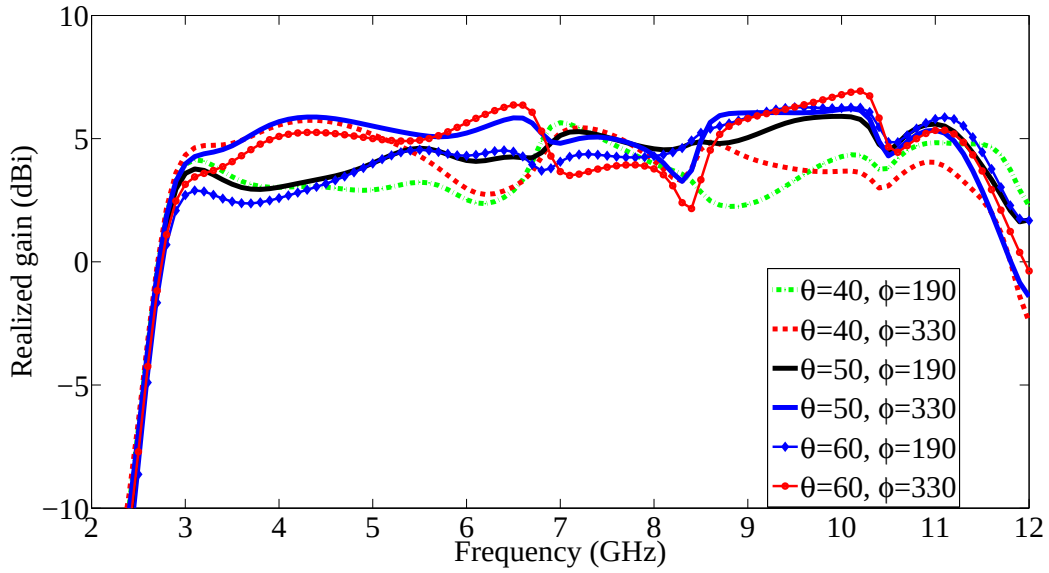

Figure 3.15: Predicted realized gain of the UWB DRA in favorable directions

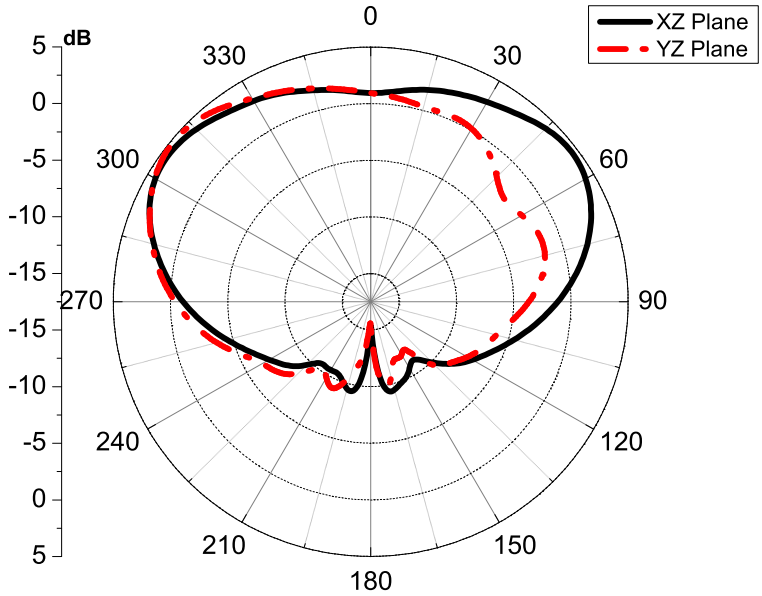

Figure 3.16: Predicted mean realized gain of the UWB DRA

strong. It was found that the total power radiated into the upper hemisphere is almost 90%, which is significantly greater than the 10% of power radiated into the lower hemisphere. One may recall that nearly all printed planar UWB antennas (e.g. [8]) have partial or no ground planes, and therefore they do radiate significantly to the lower hemisphere because the partial ground plane does not act as a shield to block this radiation. When such an antenna is integrated to the top of a wireless device (such as wireless-enabled Blu-Ray player), radiation into the lower hemisphere is wasted inside the device. Such antennas cannot be placed close to and parallel to conducting surfaces unless an UWB reflector is inserted in between [98]. This UWB DRA has been designed with a full ground plane to reduce this wastage.

In the XZ plane, E_θ pattern is almost symmetrical in the operating frequency range. However, the pattern on the orthogonal XZ plane changes with frequency because different dielectric resonance modes become dominant as frequency is swept. In the YZ plane, owing to the asymmetry of the structure and the excitation, the E_θ patterns are not symmetrical. In addition, the conducting wall also affects the radiation patterns.

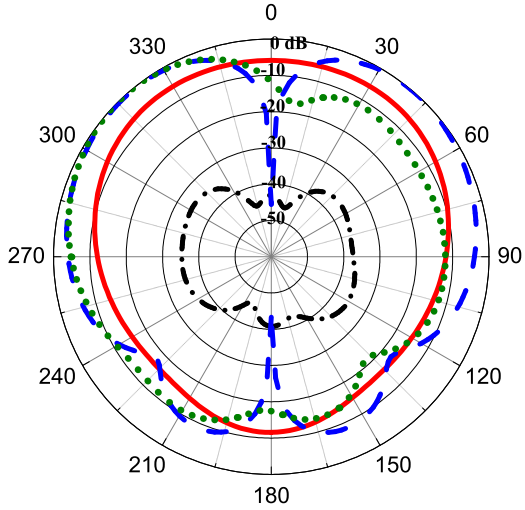

(a) 3.3 GHz

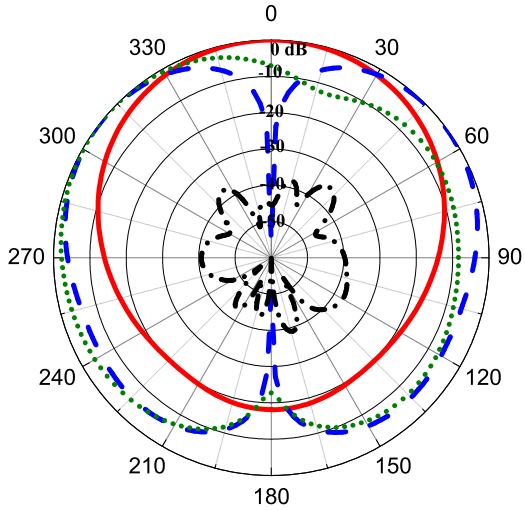

(b) 6 GHz

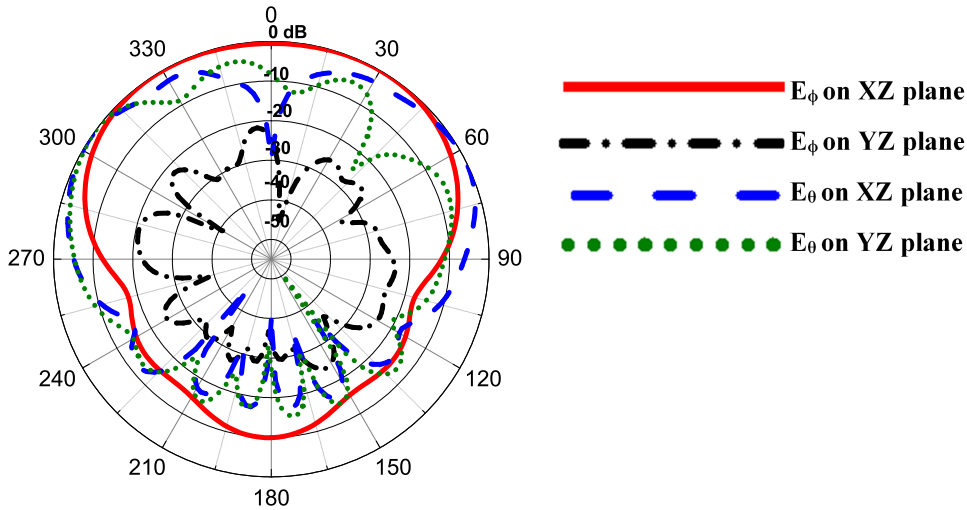

(c) 10 GHz

Figure 3.17: Computed normalized radiation patterns of the DRA

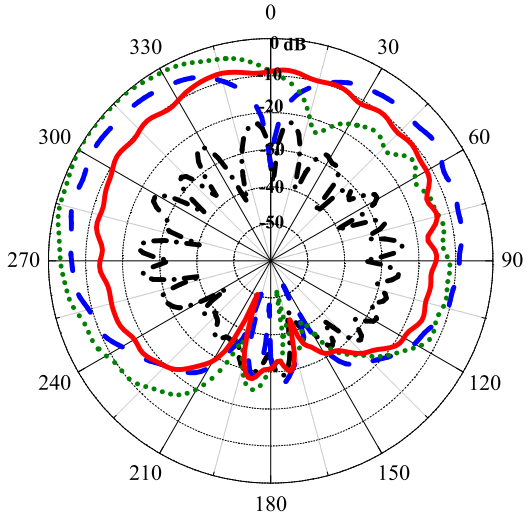

(a) 3.3 GHz

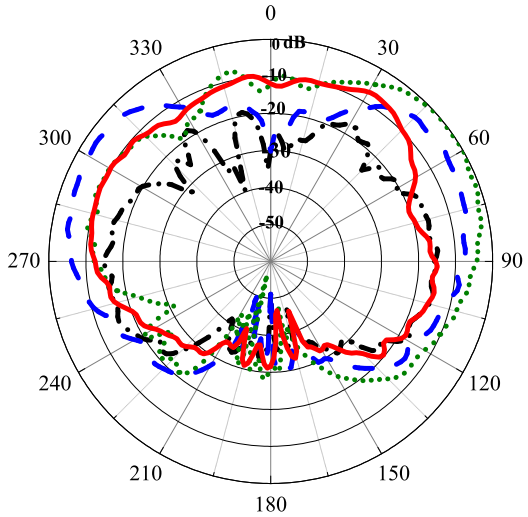

(b) 6 GHz

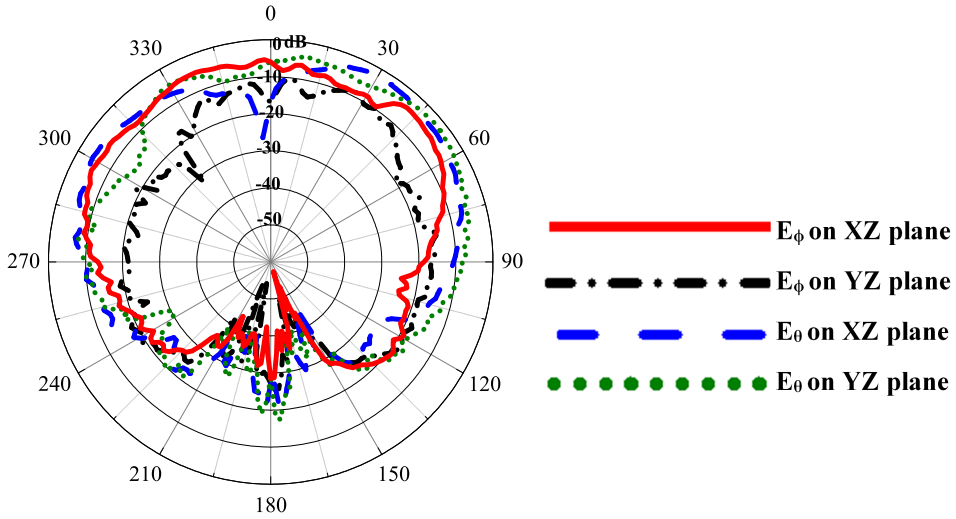

(c) 10 GHz

Figure 3.18: Measured normalized radiation patterns of the DRA

3.5 Modes of DRA

Fig. 3.19 illustrates the resonance at most interesting frequencies (3.25 GHz, 6.72 GHz and 10.44 GHz).

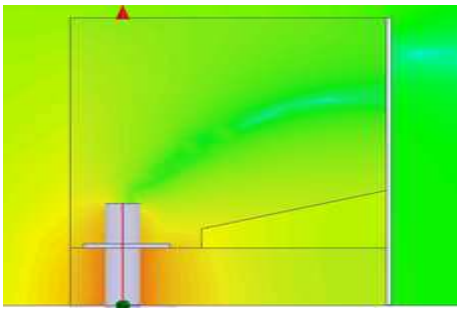

(a) 3.25 GHz

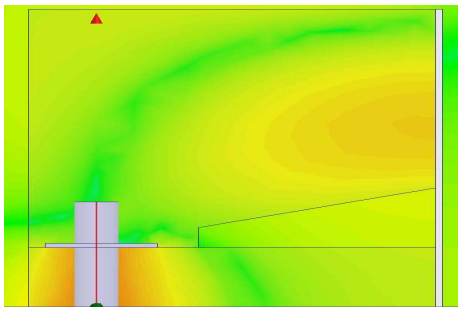

(b) 6.72 GHz

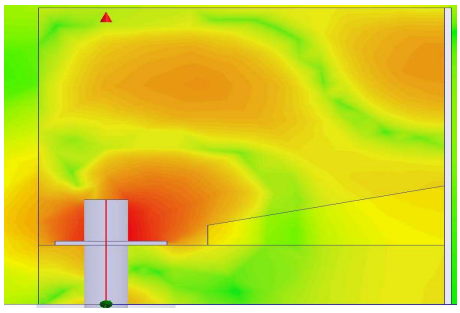

(c) 10.44 GHz

Figure 3.19: Modes of DRA

3.6 Summary

A UWB DRA with a full ground plane is investigated in frequency domain. The measured 2:1 VSWR bandwidth of this DRA is 115%, and it covers the whole FCC UWB band. It has a small footprint of 12×8 mm^2, or $0.124 \times\ 0.083\,\lambda_0^2$ at the lowest operating frequency of 3.1 GHz. Its dielectric volume is 1318.8 mm^3, or $1.45 \times 10^{-3}\,\lambda_0^3$, and its overall height is 15 mm or $0.155\,\lambda_0$.

The shape and location of the air region have a significant effect on antenna performance. Without an air region the best measured return loss is less than 10 dB at 6.2 and 8.3 GHz but with an air region it is greater than 10 dB in the entire FCC UWB band. In addition, the impedance bandwidth of the DRA improves from 109.5% to 115% due to the air region.

The mean realized gain of the UWB DRA is 4.85 dBi and 4.91 dBi in the YZ and XZ planes, respectively. Radiation characteristics reveal that 90% of the power is radiated to the upper hemisphere and this subsequently reduces the unwanted radiation in the lower hemisphere. Compared to printed UWB antennas with partial or no ground plane, this UWB DRA does not have a null in the boresight direction. Due to above reasons and also its compactness, ease of excitation, minimal surface wave losses and excellent radiation characteristics, this design is suitable for high-data rate consumer electronic devices, which are intended to transmit only in unidirectional mode.

Chapter 4

Time-Domain Analysis of UWB DRA

This chapter describes time-domain characteristics of a new UWB DRA in order to assess its suitability for impulse radio (IR) UWB systems. Time-domain characteristics and effective isotropically radiated power (EIRP) spectra of the antenna are investigated for linearly-chirped Gaussian pulse and fifth-order Gaussian pulse. The correlations between the input pulses and the radiated pulses in many directions were found to be excellent when the antenna is excited by a linearly-chirped Gaussian pulse or a fifth-order Gaussian pulse. Nevertheless, EIRP spectrum calculations indicate that none of those pulses efficiently fill the FCC UWB mask when applied to this DRA. Hence a third-order Rayleigh pulse is introduced and tuned to make efficient use of the allowed spectrum limits while radiating highly correlated pulses. Therefore, the EIRP of the DRA is increased up to 52% without exceeding FCC bounds. In addition, improvement of pulse performance is investigated by varying antenna design parameters.

4.1 Pulse Preserving Capabilities of the UWB DRA

The pulse-preserving capabilities of this antenna were evaluated in the scope of correlation factors, which describe the similarity between the input signal and the radiated electric field waveforms of a transmitting antenna. The computation of electric field waveforms can be possible in two different ways: 1) placing virtual probes located at a distance of 150 mm from the feed point of the DRA antenna; the corresponding radiated $e_\theta(t)$ components of the electric field intensity signals were recorded. 2) post-processing the radiated field components in the far-field region. Both methods were applied to compute the correlation factor of the antenna in different directions. One may note that a distance of 150 mm is not fully in far-field region according to the classical criterion of $d \geq 10\lambda$ for electrically small antennas, therefore latter method was used to verify the results already computed by the virtual probe method. Later it was found by investigation that CST software already considered those virtual probes in the far-field. Therefore, there is no significant difference between the results obtained using this method to the virtual probe method.

Following the definition in [84], the correlation factor, which is also known as fidelity factor and is a function of θ and φ, was calculated between a radiated-field waveform, $R_s(t)$, and the input excitation signal, $I_s(t)$, to evaluate the pulse preserving capability of the UWB DRA using

$$\rho(\theta,\varphi) = \max_{\tau}\left\{\frac{\int\limits_{-\infty}^{\infty} I_s(t)R_s(t-\tau)dt}{\sqrt{\left[\int_{-\infty}^{\infty}|I_s(t)|^2\,dt\right]}\sqrt{\left[\int_{-\infty}^{\infty}|R_s(t)|^2\,dt\right]}}\right\} \tag{4.1}$$

where τ is the time lag used to align input and radiated pulses, and hence to maximize correlation factor ρ in (4.1). For a thorough time-domain analysis and comparison, three different broadband pulses were chosen to excite the antenna. They are linearly-chirped Gaussian, fifth-order Gaussian, and third-order Rayleigh pulses.

4.1.1 Radiated Pulses and Spectra

Linearly-Chirped Gaussian Pulse

A Gaussian-based amplitude modulated signal that also has a linear frequency modulation, also known as a linearly-chirped Gaussian signal, is given by [99]:

$$s_2(t) = A(t)\cos(2\pi(\frac{\beta_o}{2})t^2 + 2\pi f_o t) \tag{4.2}$$

where

$$A(t) = e^{-t^2/2\sigma_1^2}$$

and

$$\beta_0 = \frac{(f_1 - f_o)}{\triangle t}$$

where $f_\circ$ and f_1 are initial and final frequencies of the signal, $\triangle t$ is the time the pulse takes to change the frequency from $f_\circ$ to f_1, and σ_1 is the width of a pulse. The following values have been assigned to pulse parameters: $f_\circ$ =3.1 GHz, f_1 =10.6 GHz, $\triangle t$ = 1.42 ns and σ_1 = 140 ps. The linearly chirped Gaussian pulse and radiated field waveforms are shown in Fig. 4.1(a), and their spectra are illustrated in Fig. 4.1(b). It can be seen from Fig. 4.1(b) that group delay is consistent over the frequency band which gives very good correlation factor. Detailed analysis of correlation factor is described in the following section.

Fifth-Order Gaussian Pulse

Perhaps the most commonly used pulse for time-domain analysis of UWB antennas is the fifth-order Gaussian pulse, given by [100]:

$$s_3(t) = C(-\frac{t^5}{\sqrt{2\pi}\sigma_2^{11}} + \frac{10t^3}{\sqrt{2\pi}\sigma_2^9} - \frac{15t}{\sqrt{2\pi}\sigma_2^7}) \times e^{-(\frac{t^2}{2\sigma_2^2})} \tag{4.3}$$

where C is a constant and σ_2 has to be 51 ps to ensure that the shape of the spectrum complies with the FCC spectral mask. The input pulse and the radiated pulses in the time

domain and their spectra are shown in Figs. 4.2 (a) and (b), respectively. Compared to the linearly-chirped Gaussian pulse, fifth-order Gaussian pulse's spectrum covers larger area under the FCC mask which is one of the reasons that UWB DRA has better correlation factor by using fifth-order Gaussian pulse.

4.1.2 Correlation Factors for Different UWB Pulses

Results in the previous subsection are limited to few directions. For a through comparison, correlation factor ρ was computed in many directions (in 5° steps) in XY, YZ and XZ planes, for each input pulse. It was found that the fifth-order Gaussian pulse has best overall results with this DRA as compared to linearly-chirped Gaussian pulse. To describe this in details, the computed ρ in the XY, YZ, and XZ planes are shown in Fig. 4.3. It can be seen from Fig. 4.3(a) that in the XY plane, the fifth-order Gaussian pulse and the linearly-chirped Gaussian pulse have nearly the same ρ, with best values of 0.978 and 0.988, respectively, in $\phi = 0^o$ and 180° directions. At $\phi = 90^o$ and $\phi = 270^o$, ρ decreases to 0.924 and 0.847 for the fifth-order Gaussian pulse, and 0.793 and 0.819 for the linearly-chirped Gaussian pulse, respectively. Overall, the fifth-order Gaussian pulse has the best average ρ of red 0.938 over the azimuthal plane.

In YZ and XZ planes, only the θ range between -90° and 90° is considered here because most of the energy is radiated into the upper hemisphere due to the presence of the full ground plane. It can be seen from Fig. 4.3(b) that the fifth-order Gaussian and the linearly-chirped Gaussian pulses have the best ρ of 0.979 and 0.973, respectively, at $\theta = -40^o$. In Fig. 4.3(c), the linearly-chirped Gaussian has the best ρ of 0.987 at $\theta = -90^o$, on the XZ plane. Between $\theta = -28^o$ and $\theta = 28^o$ directions on this plane, E_ϕ is the major polarization and therefore ρ was calculated for E_ϕ in addition to E_θ. The average ρ of E_ϕ in these directions is 0.825 and 0.815 for the fifth-order Gaussian and the linearly-chirped Gaussian pulse, respectively.

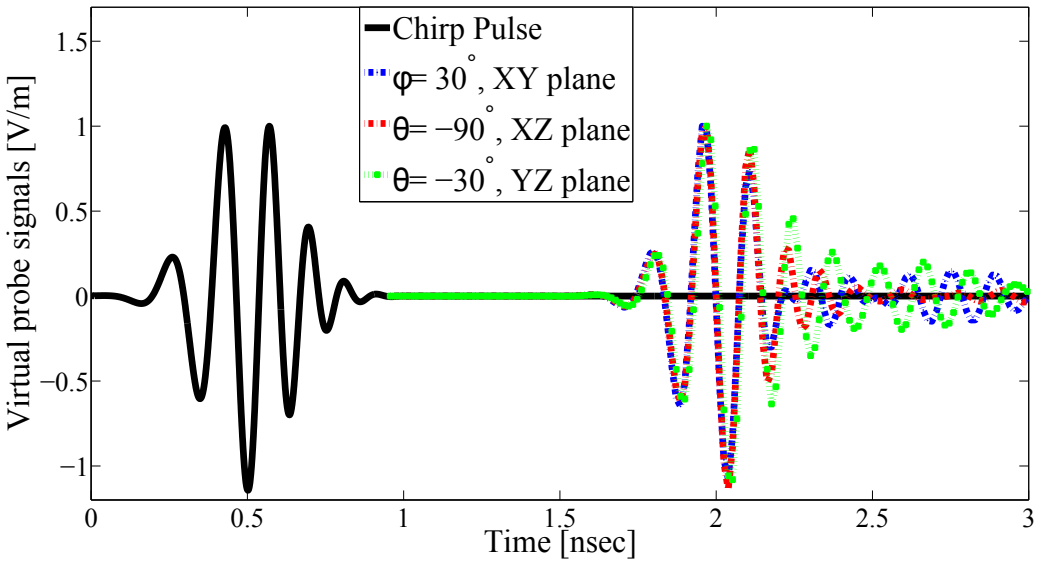

(a)

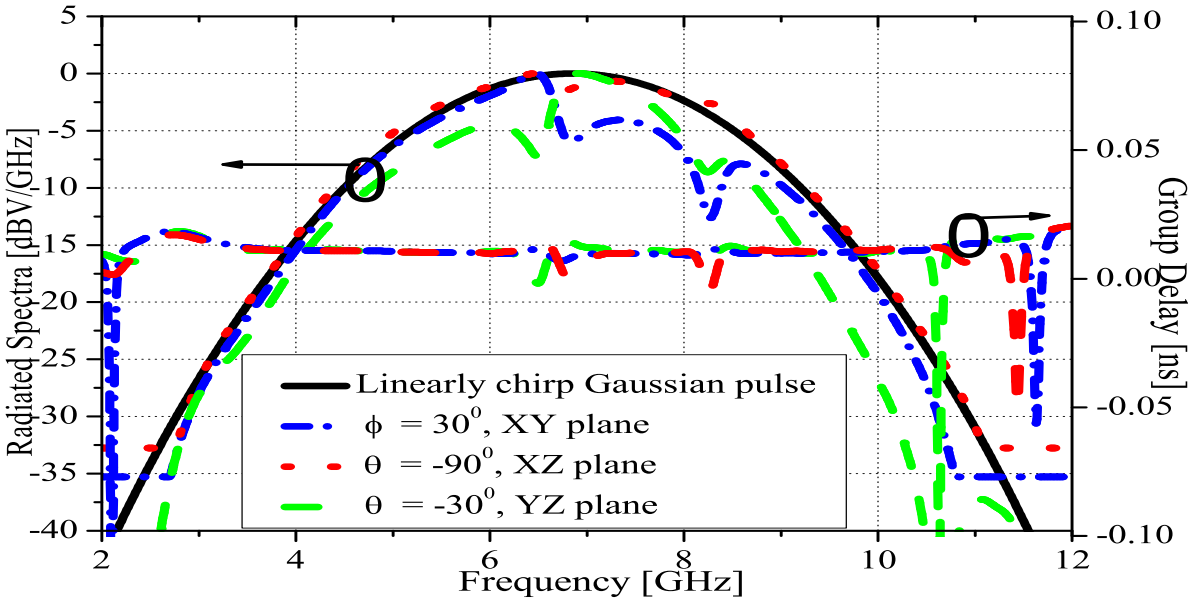

(b)

Figure 4.1: Input and radiated signals for a linearly-chirped Gaussian pulse (a) signals and (b) Spectra

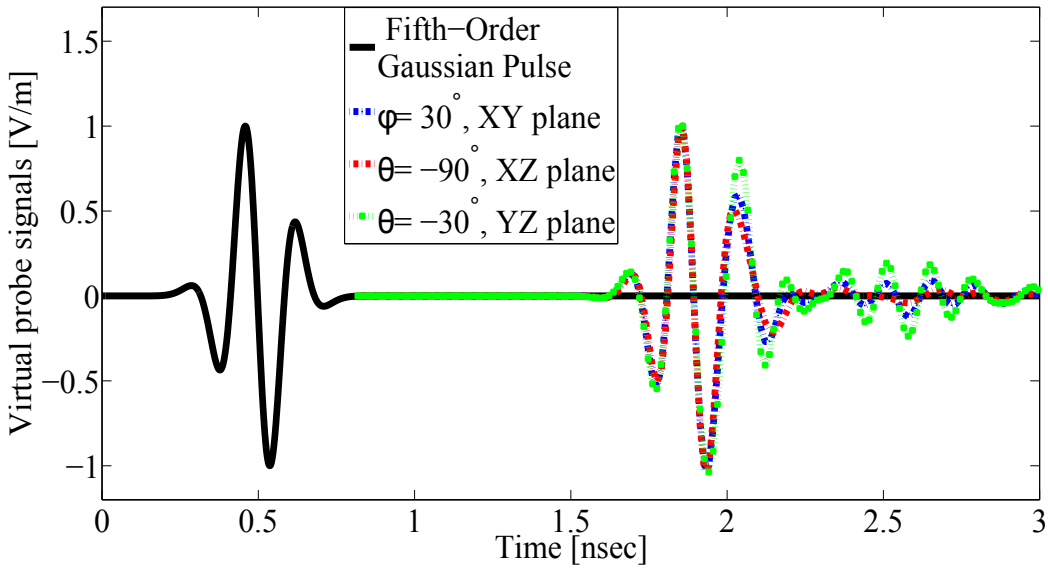

(a)

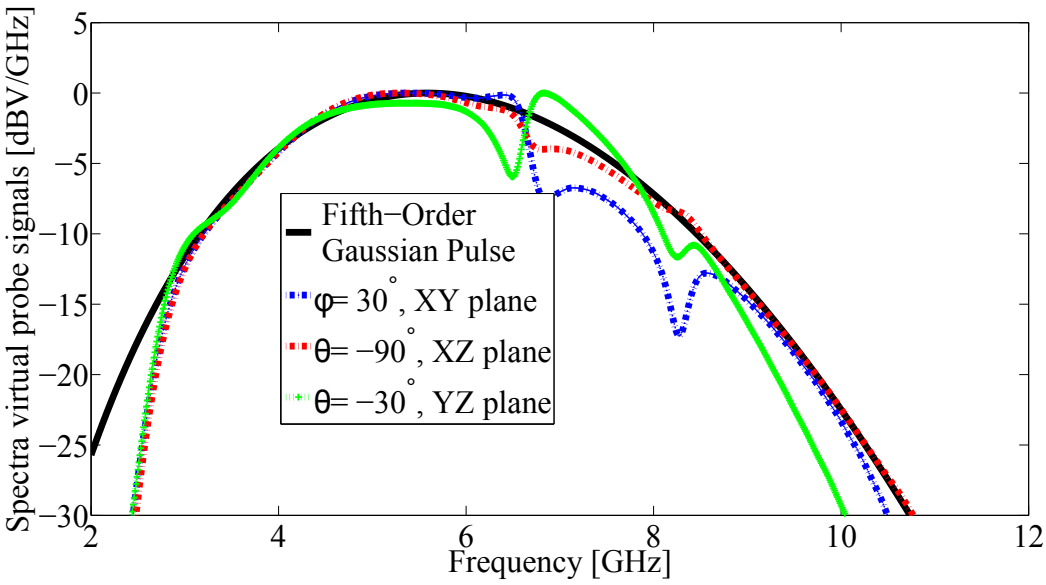

(b)

Figure 4.2: Input and radiated signals for a fifth-order Gaussian pulse: (a) Signals and (b) Spectra

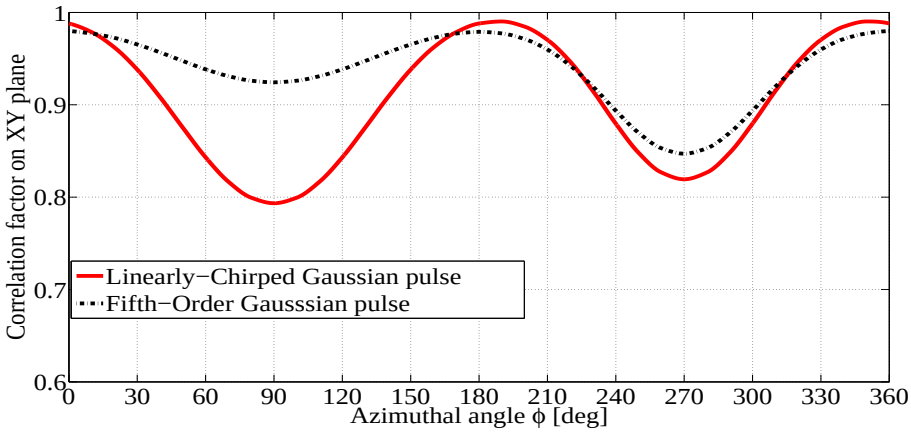

(a)

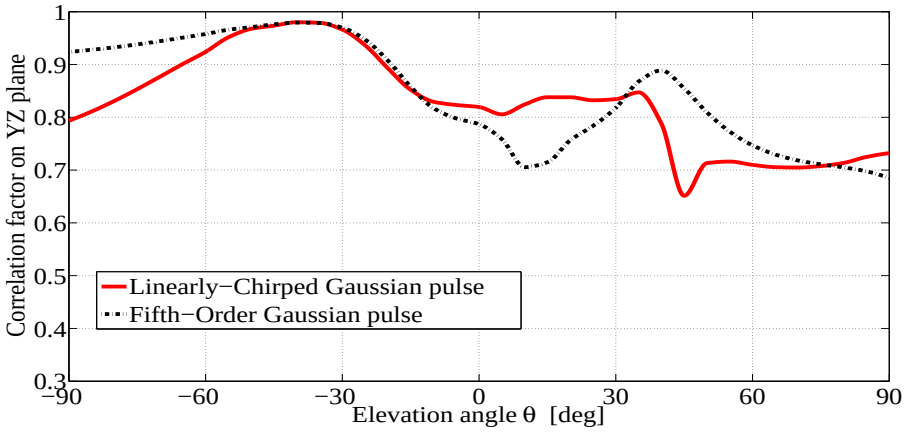

(b)

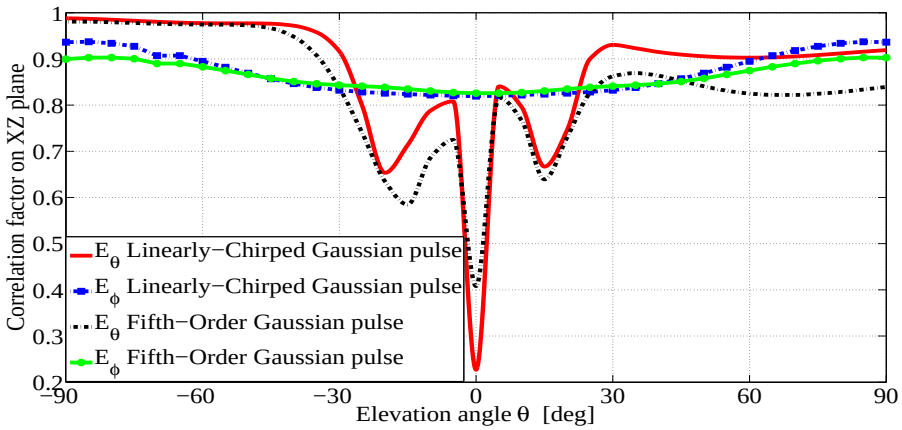

(c)

Figure 4.3: Correlation factors of the UWB DRA with linearly-chirped Gaussian pulse, and fifth-order Gaussian pulses: (a) XY plane, (b) YZ plane, and (c) XZ plane

4.1.3 Effective Isotropically Radiated Power

In order to avoid the potential interference with existing radio systems, the FCC of USA has imposed a spectral mask for UWB indoor systems. This allows a maximum transmitted EIRP of -41.3 dBm/MHz within the band and even less near band edges, as shown in Fig. 4.4. EIRP of an antenna in general is a function of frequency, which is defined as [101]:

$$EIRP(f) = P_T(f)G_T(f) \tag{4.4}$$

where $P_T(f)$ is the radiated power spectrum and $G_T(f)$ is the peak gain at frequency, f. If the antenna is frequency independent, G_T is a constant and $P_T(f)$ spectrum has the same shape as the power spectrum of the input pulse. Most antennas and in particular UWB antennas have frequency dependent properties and therefore EIRP spectrum can significantly differ from the input pulse spectrum. Fig. 4.4 shows the EIRP spectra of the UWB DRA for the aforementioned pulses. They are compared with the FCC indoor mask in the same figure. For each pulse, the magnitude of the input pulse is maximized to the extent possible while confining the corresponding EIRP spectrum to the FCC mask. It can be observed that the EIRP spectra for the Chirp and the fifth-order Gaussian pulses touch the FCC mask only at one frequency. Their EIRP levels are well below the limit allowed by FCC for most of the frequencies in the 3.1-10.6 GHz band. On the other hand, the EIRP spectra produced by this DRA with a first-order Rayleigh pulse (not shown) touches the FCC limit at 3.1 GHz and it is well below the -41.3 dBm/MHz peak limit for all other frequencies in the said band.

It is clear from Fig. 4.4 that, when used to excite the UWB DRA, none of these three pulses efficiently makes use of the FCC limit of -41.3 dBm/MHz allowed between 3.1 and 10.6 GHz.

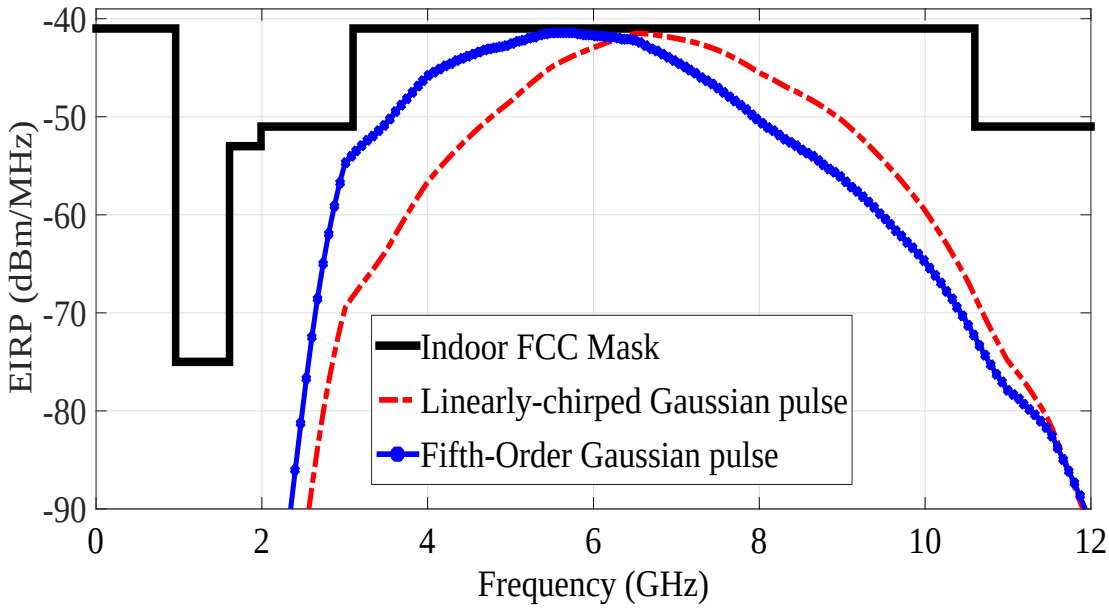

Figure 4.4: EIRP spectra of the UWB DRA for two different input pulses

4.1.4 EIRP & Pulse Performance with Third-Order Rayleigh Pulse

To rectify the EIRP limitation raised in the previous subsection, let us introduce a third-order Rayleigh pulse to excite the UWB DRA. The third-order Rayleigh pulse is given by

$$s_4(t) = C(\frac{4t^4 + 3\sigma_3^4 - 12t^2\sigma_3^2}{\sigma_3^8} e^{-(\frac{t}{\sigma_3})^2}) \tag{4.5}$$

where C is a constant, and σ_3 is chosen to ensure that the EIRP spectrum complies with the FCC spectral mask.

Our computations showed that, for the UWB DRA, a third-order Rayleigh pulse leads to better utilisation of the FCC limits as compared to the three pulses mentioned in the previous subsection. A parametric analysis was conducted to find the optimal value for σ_3 and the results are compared in Fig. 4.5.

For efficient utilisation of FCC limit, our selected value for σ_3 is 70 ps. One may note that the EIRP spectrum for $\sigma_3 = 70$ ps fills the FCC mask much better than spectra in Fig. 4.4.

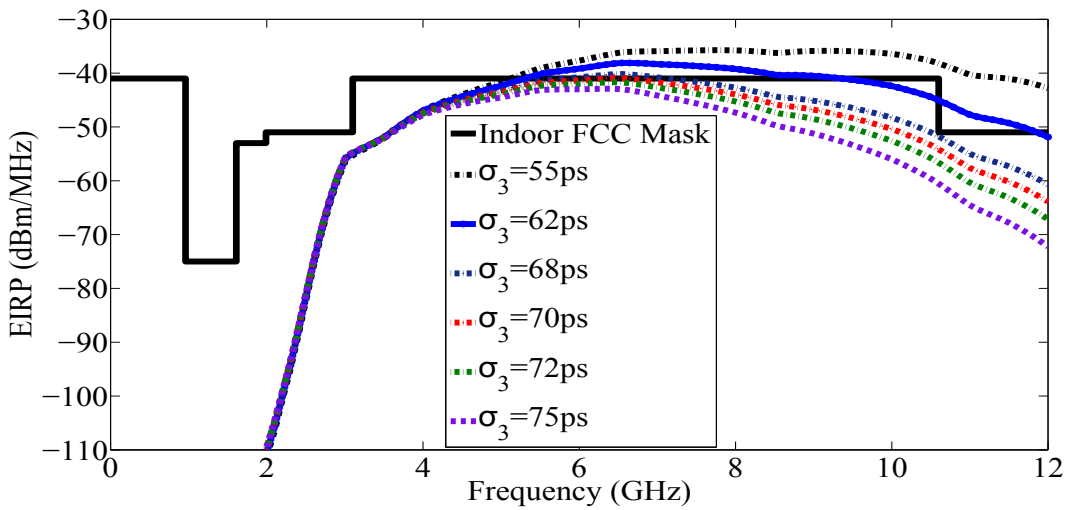

(a)

Figure 4.5: EIRP spectra of the UWB DRA for third-order Rayleigh pulses with different values of σ_3

In order to evaluate spectral efficiency (SE) of the above-mentioned pulses for the UWB DRA, SE is calculated using

$$SE = \int_{BW} EIRP(f)\, df \Big/ \int_{BW} S_{FCC}(f)\, df \tag{4.6}$$

where S_{FCC} is the FCC spectral mask. The SE is calculated over the 3.1-10.6 GHz FCC UWB band.

It was found that SE is 52% for a third-order Rayleigh pulse with $\sigma_3 = 70$ ps. This is a significant improvement over the SE values of 34% and 40% for the linearly-chirped Gaussian pulse and fifth-order Gaussian pulse, respectively. In addition to this, Table. 4.1 shows the calculated EIRP value of aforementioned pulses.

Table 4.1: Total EIRP of the input pulses

Input Pulse	EIRP (mW)
First-order Rayleigh	0.05
Linearly-chirped Gaussian	0.17
Fifth-order Gaussian	0.20
Third-order Rayleigh	0.26

For a third-order Rayleigh pulse with $\sigma_3 = 70$ ps, the radiated signal waveforms and their spectra are shown in Figs. 4.6 (a) and (b), respectively. Furthermore, it is found that in all considered planes, the third-order Rayleigh pulse has excellent pulse-preserving characteristics. We have also investigated the performance of DRA for a first-order Rayleigh pulse and found that in general performance is worse. The pulses considered in the thesis lead to better performance because their spectra are more compatible with antenna VSWR bandwidth whereas first-order Rayleigh pulse has a significant amount of low-frequency energy below the antenna bandwidth.

4.1.5 Effects of ground plane and air region on pulse performance

In this section, we attempt to enhance pulse performance of the UWB DRA further by changing the dimensions of the ground plane and the air region. The third-order Rayleigh pulse with $\sigma_3 = 70$ ps is applied as the excitation. The length and width of the ground plane (G_l) are swept from 20 mm to 40 mm whereas both h_2 and h_3 of air region are swept from 1 mm to 5 mm. In this investigation, it was found that reducing the size (G_l) of the ground plane below 25 mm significantly deteriorates the matched bandwidth.

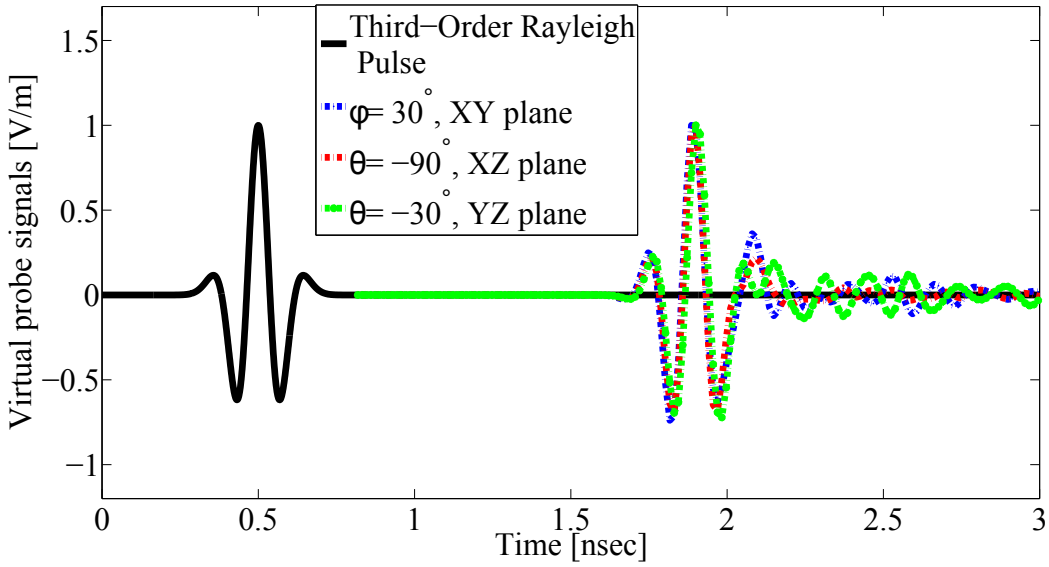

(a)

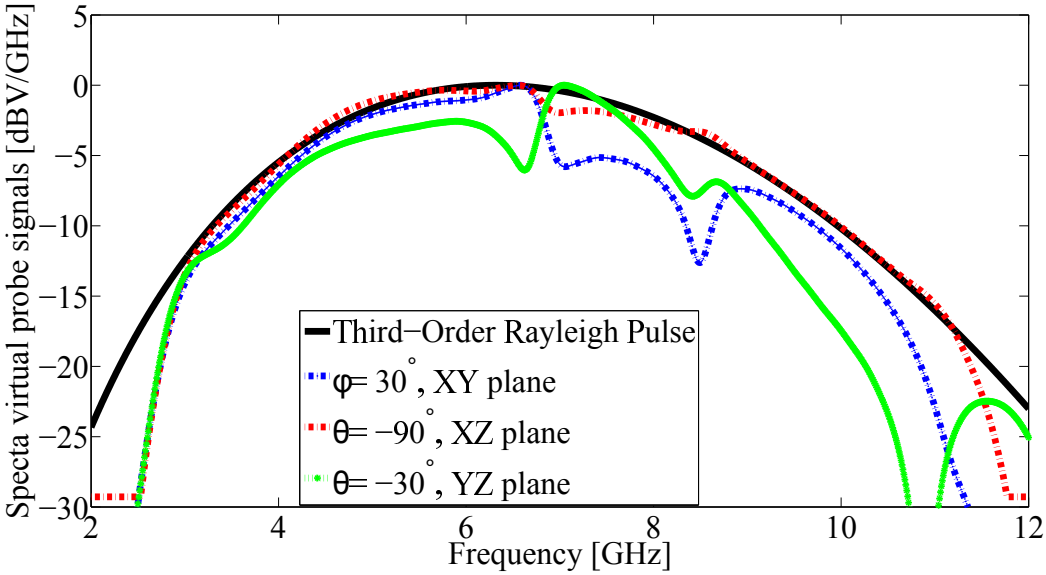

(b)

Figure 4.6: Third-order Rayleigh input pulse and corresponding radiated signals: (a) signals, (b) Spectra

Similarly, the dimension of air region, h_2, is restricted to the range of 1 - 3 mm, and the h_3 dimension is restricted to the range of 1 - 4 mm, in order to obtain a good return loss bandwidth in the FCC UWB band. Pulse performance and EIRP of the UWB DRA was further investigated for those ranges of design parameters that produce impedance matching in the entire UWB band.

From Fig. 4.7 (a), it is evident that variation of the size of the ground plane between 25 mm and 40 mm has a negligible effect on pulse performance of the UWB DRA in XY plane. However, changing (h_2, h_3) dimensions of the air region from (1 mm, 3 mm) to (3 mm, 4 mm) improves the minimum correlation factor from 0.76 to 0.85 at $\phi = 90^o$. Similarly, there is a slight improvement of correlation between $\theta = -90^o$ and -40° directions in the YZ plane, as shown in Fig. 4.7 (b). Between 0° and 90° directions on this plane, average correlation is approximately the same for all considered cases but minimal fluctuation is noticed for the dimensions of $G_l = 40$ mm, $h_2 = 3$ mm, $h_3 = 4$ mm.

As discussed in 5.1.2, E_ϕ component is more appropriate than E_θ between $\theta = -28^o$ and $\theta = 28^o$ directions on the XZ plane. In Fig. 4.7 (c), it can be seen that correlation factor for E_ϕ is approximately 0.81 in the aforementioned range of directions. Again the size of the ground plane has a negligible effect on pulse-preserving capabilities on this plane. By comparing the correlation factors in all planes, it is noticed that overall performance of the antenna can be slightly improved by increasing h_2 to 3 mm, and h_3 to 4 mm. Nevertheless these changes to h_2 and h_3 have a minimal effect on the EIRP spectra of the UWB DRA.

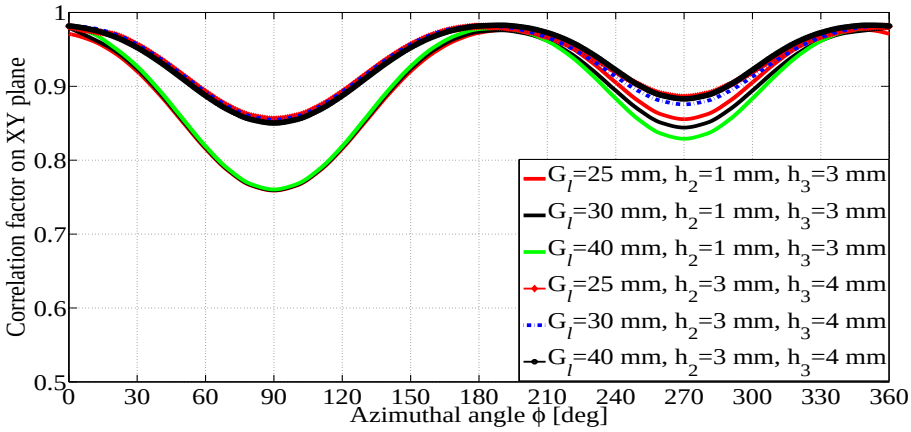

(a)

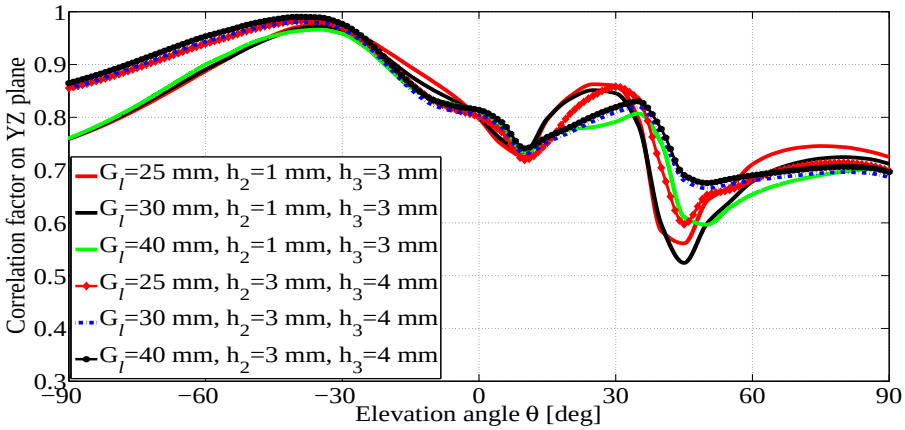

(b)

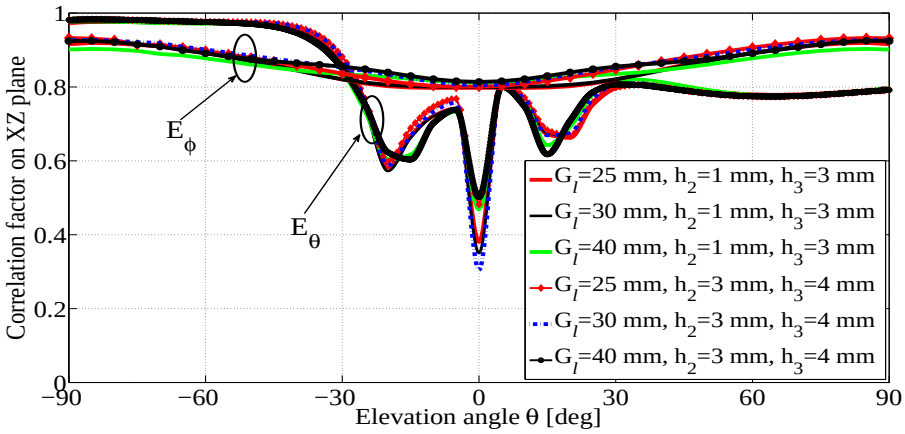

(c)

Figure 4.7: Correlation factors for different ground plane sizes and air-regions (a) XY Plane, (b) YZ Plane, (c) XZ Plane

4.2 Comparison of Results

Table. 4.2 shows an improvement in the state of the art tetrahedron-DRA design. It can be seen that bandwidth performance has improved from 109% to 116% whereas time-domain characterisation of UWB DRA has been analysed first time in literature, and it showed excellent pulse-preserving characteristics.

Table 4.2: Comparison of overall performance between the classical DRA and tetrahedron DRA

Structure	Dimensions a x b x d (mm^3)	Surface Area (mm^2)	Volume (mm^3)	Measured Imepdance Bandwidth (GHz), %	Fidelity Factor	Spectrum Efficiency
Classical DRA	12 x 8 x 15.3	804	1468.8	3.1-10.6, 109 %	---	---
Tetrahedron-DRA	12 x 8 x 15	792	1440	3.1-11.6, 116 %	Third-Order Rayleigh Pulse (0.981)	52.00%

4.3 Summary

For both linearly-chirped Gaussian and fifth-order Gaussian pulses, the correlation between the radiated pulses and the input pulse is excellent in most directions. Nevertheless, when either of those pulses are radiated by this DRA, the EIRP spectrum produced by the antenna does not efficiently fill the FCC UWB mask. This limitation has been addressed by introducing a third-order Rayleigh pulse and tuning it to generate an EIRP spectrum that fills the FCC mask well. This way, total spectral efficiency of the antenna is significantly increased to 52% without overstepping FCC mask limits. When analytical input pulses are considered, this is a significant improvement over the excellent 40% spectral efficiency from a monopole antenna reported in [102]. Ground plane size has no

significant effect on correlation as long as it is greater than 25 mm but overall correlation can be improved by optimising the dimensions of the air region. The best correlation factor found with the optimal air region is 0.981. The average correlation in the two elevation planes is 0.823, and the average correlation factor in the azimuth plane is 0.931. To the best of our knowledge, no other DRA has better pulse-preserving characteristics in all important directions. It is expected that the high correlation factor in these directions will result in good bit-error-rate (BER) of IR UWB systems. This DRA is suitable for both impulse radio (IR) UWB systems and carrier-based UWB systems.

In the next chapter, in order to differentiate the DRA's name from the Chapter 4 and 5, tetrahedron DRA will be used instead of UWB DRA.

Chapter 5

A Low-profile Multi-segment Dielectric Resonator Antenna for Wideband Communication

In the previous chapter, the tetrahedron DRA was presented for UWB applications. This chapter presents a low-profile dielectric resonator antenna for wideband communication. The main contribution of this chapter is to enhance the bandwidth-to-volume ratio of DRA to make them more useful in volume-critical applications. It is demonstrated that the size of the tetrahedron DRA can be reduced by using multi-segment dielectric materials. For this reason it is called a Multi-Segment Dielectric Resonator Antenna (MSDRA). Analogous to the tetrahedron DRA, a full ground plane is employed with MSDRA to radiate most of the radiation in the upper hemisphere. In addition, a conducting wall is applied to halve the size of MSDRA. Overall, the MSDRA's bandwidth-to-volume ratio is substantially enhanced over the wide impedance bandwidth. Hence, this antenna can be easily integrated with many communication devices. Promising applications include ground penetrating radar, high-resolution microwave imaging, personal area networks and

short-range wireless communications. This wideband MSDRA is analysed using full-wave simulations in CST MWS and Ansys HFSS, and then it is verified through prototype fabrication and testing. In this chapter, the methodology to improve the bandwidth-to-volume ratio of MSDRA is presented. Furthermore, extensive investigation is conducted to reduce the area of ground plane, and to employ the MSDRA for on-body and off-body communication.

5.1 Principle of Operation

5.1.1 Dielectric Constant, Size and Impedance Bandwidth

The dielectric constant of the material controls the size of a DR. However, by increasing its dielectric constant can significantly reduces the impedance bandwidth of a DRA. In order to enhance the impedance bandwidth of a DRA whilst retaining the low mass of a DR, three major techniques have been implemented. Firstly, permittivity of a DR can be reduced by introducing an air region inside the DR or embedded different dielectric segments to the DR. Secondly, the aspect ratio of the DRA can be optimised in a multitude of ways to lower the permittivity of the DRA [46]. Thirdly, the Quality factor, Q, of the antenna increases as $\varepsilon_r^{3/2}$, therefore a rigorous analysis of Q factor provides an insight into the overall permittivity of the antenna over the entire band of operation.

These fundamental characteristics of the DR lead to the idea of designing a wide-band antenna that is significantly smaller in volume in comparison to the tetrahedron DRA. Nevertheless, a new criterion, bandwidth-to-volume ratio, is also introduced and it incorporates a comparison of the impedance bandwidth and size of both antennas. Therefore, rigorous analysis of the tetrahedron DRA has been done using the above-mentioned techniques, specifically to examine the bandwidth performance of the antenna.

5.1.2 Computation of Effective Permittivity

The dimensions and components of the tetrahedron DRA, as shown in Fig. 4.1, are considered in this Chapter. In order to reduce the height of the tetrahedron DRA, it is essential to find the antenna's effective permittivity. This information is used to predict the resonant frequency of the antenna. The effective permittivity, ε_{eff}, of the tetrahedron DRA is calculated using [15]:

$$\varepsilon_{eff} = \frac{H_t}{h_{LPI}/\varepsilon_{LPI} + h_{DR}/\varepsilon_{DR}} \tag{5.1}$$

where ε_{LPI} and ε_{DR} are the dielectric constants of the DRA. The total height H_t is the sum of the lower dielectric segment, h_{LPI}, and upper segment, h_{DR}:

$$H_t = h_{LPI} + h_{DR} \tag{5.2}$$

Table 5.1 shows the calculated effective permittivity and resonant frequency of the tetrahedron DRA. The resonant frequency of the tetrahedron DRA can be calculated by the transcendental equations [65], already discussed in the literature review.

Table 5.1: Effective permittivity and predicted resonance frequency of the UWB DRA

Lower Segment (LPI)		Upper Segment (DR)		Effective Permittivity	Resonance Frequency
ε_{LPI}	h_{LPI}	ε_{DR}	h_{DR}	ε_{eff}	f_r
2.2	9.2	3.0	12.0	5.62	6.41

The second approach to predicting the effective permittivity of the tetrahedron DRA is made possible by calculating the Q factor of the antenna. Q factor serves as a figure of merit for assessing the performance or quality of a resonator. It can be calculated straightforwardly by using [65]:

$$Q = 2\omega_0 \frac{W_e}{P_{rad}} \tag{5.3}$$

where W_e and P_{rad} are the stored energy and radiated power, respectively, and $\omega_0 = 2\pi f_0$. These quantities can easily be computed in the EM solver by placing a bounding box around the antenna. The total stored energy used to predict the Q factor of the antenna can be calculated by applying the Poynting theorem. Q factor is mainly defined in two different ways. First there is the *unloaded Q*. This is the Q (known as Q_u) when the resonator is freely oscillating without being driven externally by an external source. When the external source is connected to the resonator and is continuously provided with energy, the appropriate Q would be the *loaded Q*. In the case of antennas, the latter definition is applicable. Generally for antennas Q factor is referred to as Q_{rad}. Nevertheless, DRAs have negligible dielectric and conductor loss compared to their radiated power. Therefore the radiated Q_{rad} is approximately equal to unloaded Q (Q_u).

Considering the same example of the tetrahedron DRA as explained earlier in this section, the Q factor is computed with respect to different permittivities of DR, as shown in Fig. 5.1(a). The main objective of this investigation was to examine the effect of a high dielectric constant on the reflection coefficient magnitude. It is clear from the graph that increasing the dielectric constant of the DR leads to high Q factors at a number of frequency points and eventually the antenna acts as a storing element.

Fig. 5.1(b) shows the antenna $|S_{11}|$ from 2-12 GHz for different permittivities. Compared to the tetrahedron DRA (black solid line), increasing the permittivity of the DR leads to high spikes of the Q factor. In order to understand the physical insight of the Q factor, mean and standard deviation of the Q factor was calculated. Table 5.2 reveals the fact that average value (mean) of Q factor for $\varepsilon_r = 9.2$ is the lowest with standard deviation of 2.49, whereas $\varepsilon_r = 35.0$ has the highest Q factor with maximum deviation of 3.51. These results clearly show that maintaining the average Q factor, in the 5 to 6 range, and minimal dispersion tends to produce a contiguous wide impedance bandwidth. Standard deviation or dispersion evaluates the fluctuation of the Q factor. Therefore,

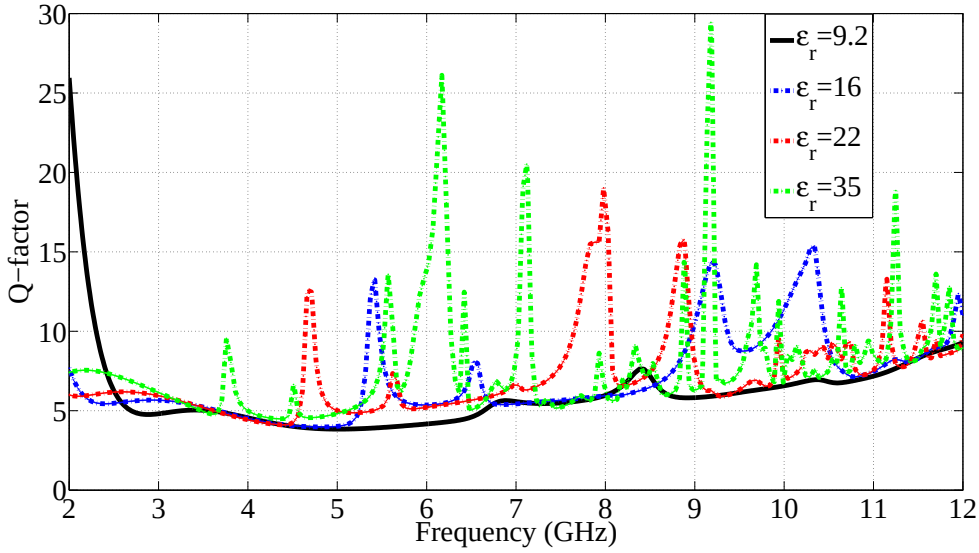

(a)

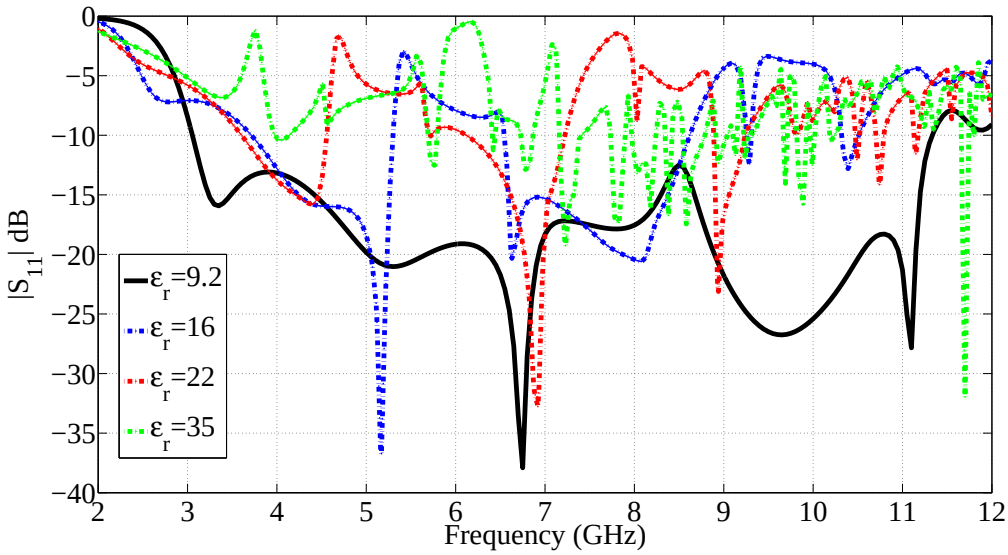

(b)

Figure 5.1: (a) Predicted Q factor of the tetrahedron DRA for different permittivities of ε_{DR}, (b) Predicted $|S_{11}|$ of the tetrahedron DRA for different permittivities of ε_{DR}

minimal dispersion of the Q factor decreases the likelihood of an impedance mismatch for wideband DRAs. This concept has been validated explicitly in the case of DRA.

Table 5.2: Mean and Standard Deviation of Q factor for different permittivities of ε_{DR}

ε_r	Mean (Q factor)	Standard Deviation
9.2	5.54	1.23
16.0	6.99	2.65
22.0	7.15	2.73
35.0	7.80	4.00

5.1.3 Aspect Ratio and Impedance Bandwidth

Last but not least, improvising the aspect ratio of DRAs can play a significant role in enhancing impedance bandwidth [59]. Since the resonance frequency is inversely proportional to $\sqrt{\varepsilon_r}$, increasing the dielectric constant increases the Q factor and the impedance bandwidth shrinks. In order to mitigate this outcome, volume-to-surface ratio of the DR is minimized. An appropriate selection of the DR shape counteracts the effect of increasing dielectric constant whilst keeping the antenna size compact.

Apart from the above-mentioned techniques, a wider bandwidth of operation can be obtained by designing a multiple segment DRA. As each dielectric segment resonates at a different frequency, the coupling of modes tends to enhance the wideband response of the DRA. However, in order to induce strong coupling, each dielectric segment should support resonant modes closely spaced in frequency.

5.2 Parametric Analysis of tetrahedron DRA

In this section, parametric analyses have been done to enhance the bandwidth-to-volume ratio of the wideband MSDRA. Three segments of different permittivities have been used in this compact design. First, in order to examine the relationship between the dielectric constant and height, a detailed investigation was undertaken by using a tetrahedron DRA in the following subsections.

5.2.1 DR Analysis

The parametric analysis of the DR segment (as shown in Fig. 5.2) was investigated first. For this study, all other parameters were kept constant to explicitly examine the impact of height on the DRA bandwidth. As can be seen in Fig. 5.2, at h_{DR}= 12 mm, impedance bandwidth is 115% (3.1-11.6 GHz), and decreases to 75% (4.58 - 10.12 GHz) at h_{DR}=6 mm. This analysis shows that lowering the DR's height has significantly disturbed the antenna's impedance bandwidth.

Secondly, it is important to examine the effect of DR's permittivity on the impedance bandwidth of the tetrahedron DRA. Therefore, three different dielectric materials have been used to examine the effect on the antenna. Fig. 5.3 shows the curves of impedance bandwidth for TMM10 (dielectric constant = 9.2) , TMM6 (dielectric constant = 6.0 and TMM4 (dielectric constant = 4.5), respectively. It is apparent from this figure that lowering the permittivity of the DR considerably deteriorated the input matching at the lower band of frequencies (3.0 - 5.4 GHz).

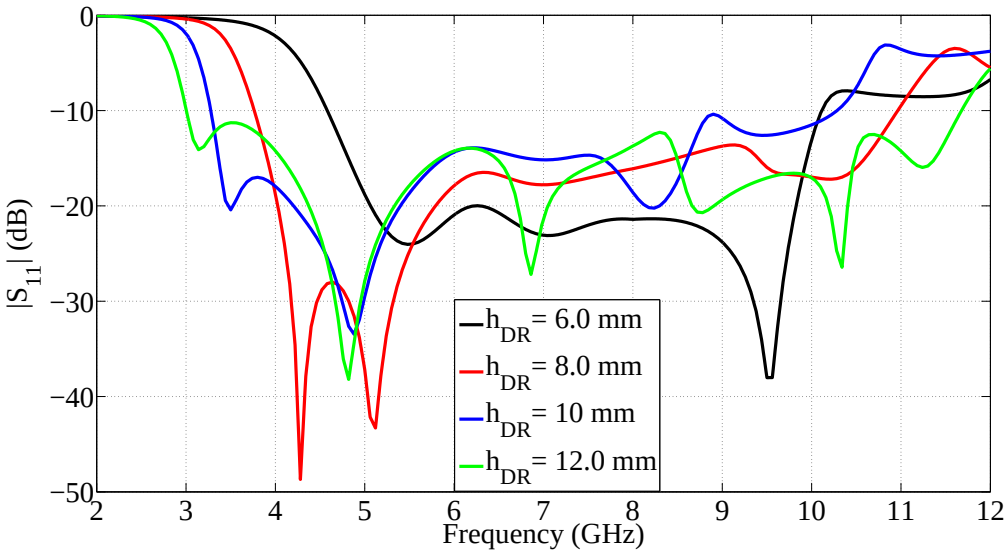

Figure 5.2: The effect of the DR height on antenna input reflection, h_{LPI}= 3.0 mm

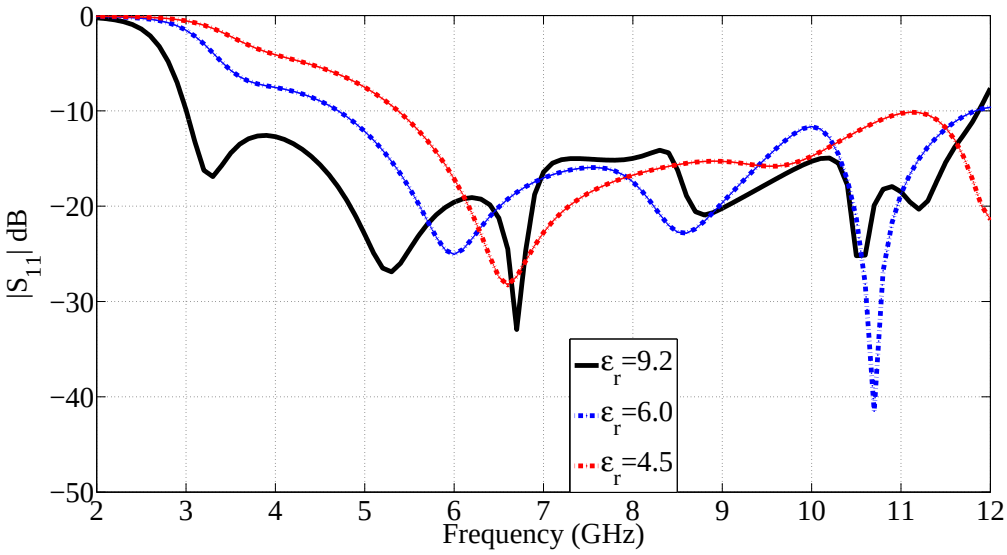

Figure 5.3: The effect of the LPI's permittivity on antenna input reflection, h_{LPI}= 3.0 mm, h_{DR}= 12.0 mm

Conversely, further increasing in the dielectric constant tends to completely compromise the impedance bandwidth of the antenna, as shown in Fig. 5.1 (b). Therefore, the evidence produced in this study suggests that reducing the height of tetrahedron DRA requires rigorous optimization with respect to aspect ratio, the permittivity of dielectric segments and the overall Q factor of the antenna.

5.2.2 LPI Analysis

In this section the LPI is investigated and Fig. 5.4 illustrates the fact that shortening its height substantially deteriorates the return loss over the entire frequency range considered. On the other hand, by changing the permittivity of the LPI to higher dielectric constant values, the return loss of the antenna reduces significantly, as shown in Fig. 5.5.

5.3 Conception of the Wideband Multi-segment DRA

Based on the previous computational evidence, it can be deduced that shortening the height or changing the permittivity of the material would not enhance the impedance bandwidth. As a result, the tetrahedron DRA was replaced by a three-segment DRA to reduce the DRA's height. In order to determine the best combination of dielectrics, three segments of different dielectrics were characterized according to the principle of operation stated in Section 5.1. In the following subsections, the final configuration of the MSDRA is discussed, and a detailed study is carried out to investigate the effects of its dielectric segments, air region and copper patches on the antenna's performance.

5.3.1 Antenna Design

The configuration of the rectangular MSDRA is shown in Fig. 5.6. It is composed of three different dielectric segments. The arrangement of these dielectric segments from bottom

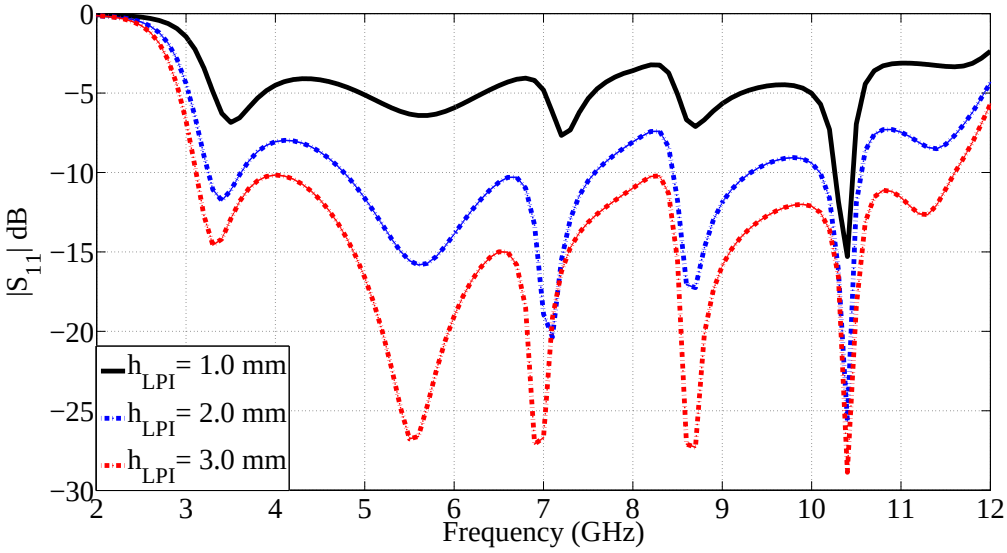

Figure 5.4: The effect of the LPI's height on antenna input reflection, h_{DR}= 12.0 mm

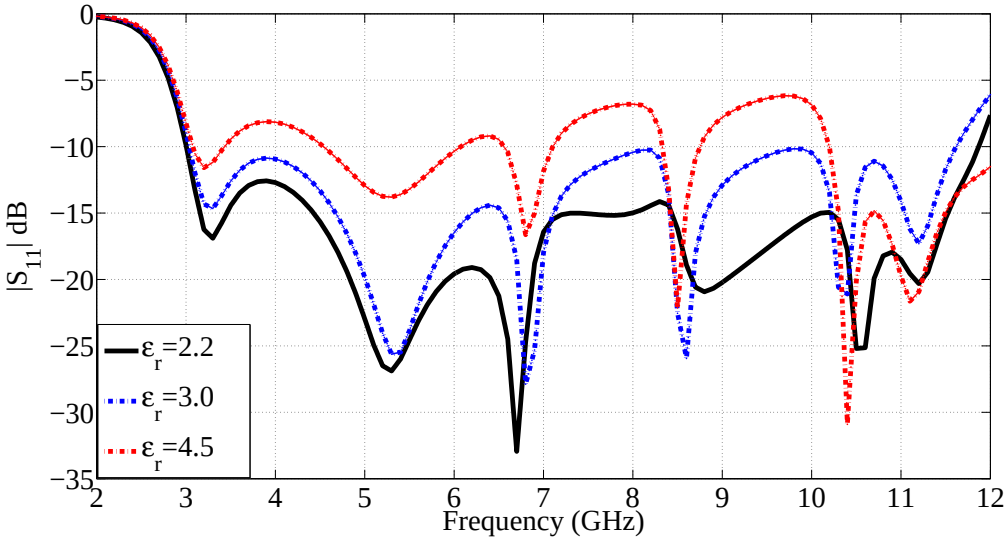

Figure 5.5: The effect of the LPI's permittivity on antenna input reflection, h_{LPI}= 3.0 mm, h_{DR}= 12.0 mm

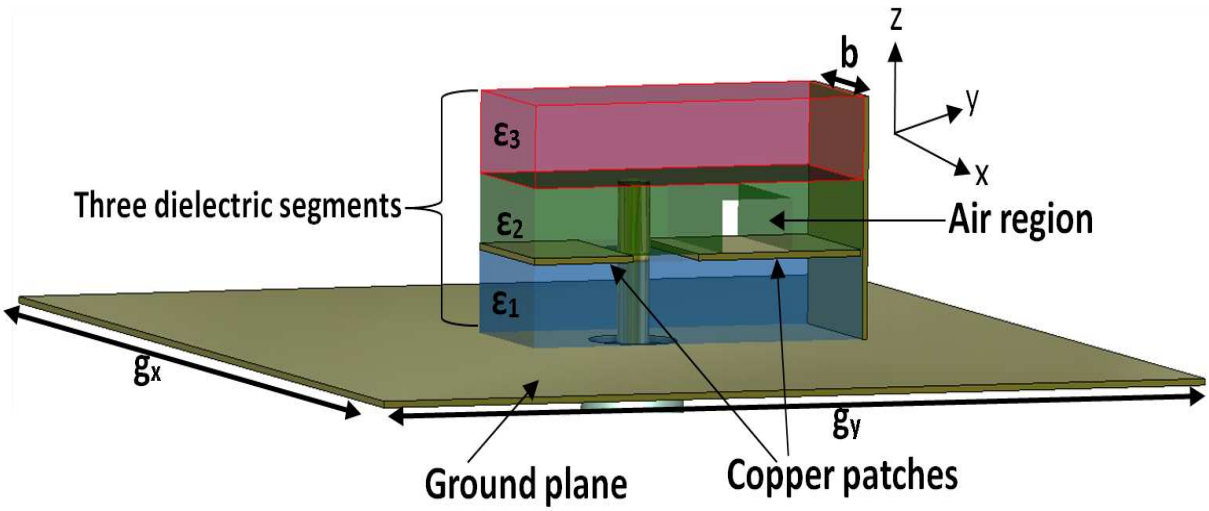

(a)

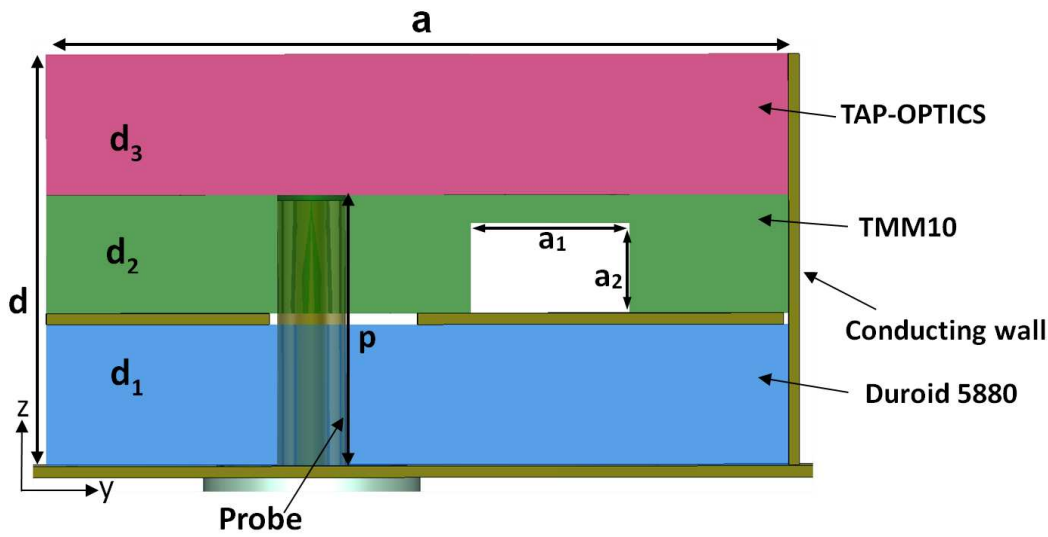

(b)

Figure 5.6: The wideband multi-segment dielectric resonator antenna

to top are Duriod 5880 ($\varepsilon_{r1} = 2.2$), TMM10 ($\varepsilon_{r2} = 9.2$) and TAP-Optics ($\varepsilon_{r3} = 16$). The lowest dielectric segment resides on a metallic ground plane. Two copper patches are sandwiched between Duriod and TMM10, without touching the probe. The copper patches' position has been optimized for better impedance matching. A rectangular groove

is introduced to form an air gap in the middle segment to reduce the effective permittivity of the DRA. The uppermost segment is chosen to improve coupling performance, resulting in higher radiation efficiency.

The DRA is fed using the inner conductor of an SMA connector as a probe, which protrudes through a small hole in the metallic ground plane. Similarly, small holes are drilled inside the Duriod 5880 and the TMM10 to accommodate the feed probe. HFSS and CST Microwave Studio software were used to fine-tune the probe length (p). In addition, image theory served to reduce the length of the antenna by approximately 50%. A conducting wall, applied to one side, creates a quasi-image for this purpose. The dimensions of the final MSDRA are shown in Table 5.3.

Table 5.3: Optimized parameters of the MSDRA

Parameter	Value (mm)	Parameter	Value (mm)
a	14	b	6
p	4.8	d_1	2.5
d_2	2.1	d_3	2.5
a_1	3	a_2	1.6
g_x	40	g_y	40

5.3.2 Parametric Analysis of MSDRA

Effective permittivity

In the previous section, the effective permittivity of two-segment tetrahedron DRA was calculated to predict the resonance frequency of the antenna. Likewise, effective permit-

tivity of three-segment MSDRA is calculated by using:

$$\varepsilon_{eff} = \frac{H_t}{d_1/\varepsilon_1 + d_2/\varepsilon_2 + d_3/\varepsilon_3} \tag{5.4}$$

where ε_1, ε_2 and ε_3 are the dielectric constants of the MSDRA. The total height H_t is the sum of the lower dielectric segment d_1, middle segment d_2 and upper segment d_3:

$$H_t = d_1 + d_2 + d_3 \tag{5.5}$$

There are many possibilities - in terms of variation in the height of segment and the dielectric constant of the segment - to analyse three-segment DRA. For brevity, only 'potential combinations' of different dielectric segments are included, and for that reason, the values of effective permittivity of the potential combinations are very close to the value of effective permittivity of the tetrahedron DRA. Fig. 5.7(a) illustrates that the predicted height of the DRA is compared and estimated by using three different dielectric segments. The height of the lower segment and the upper segment is 3.0 mm and 2.5 mm, respectively. The main focus of analysis is the middle segment, which is varied between 1 and 10 mm. On the other hand, the permittivity of the lower segment is 2.2 for all plots whereas permittivity of the middle segment is analysed by using $\epsilon_2 = 6.2$ or 9.2, alternatively. Similarly, the permittivity of the upper segment is analysed by using $\epsilon_3 =$ 12.0 or 16.0, alternatively. However, exception is the tetrahedron DRA which has only two dielectric segments.

Before initiating our discussion to analyse the effective permittivity of the MSDRA, it is important to note that in all plots shown in Fig. 5.7 and Fig. 5.8 , the same curve of the tetrahedron DRA is used to examine the relative difference between the MSDRA and the tetrahedron DRA. Additionally, the effective permittivity of the tetrahedron DRA is 5.62 (calculated in section 5.1.2) thus the expected portion ($\varepsilon_{eff} = 5.0$ to 6.0) is highlighted in order to assess the effective permittivity of the MSDRA.

Our main objective was to lessen the effective permittivity of the MSDRA in the highlighted region to reduce the total height. Consequently the main point of interest in these plots is to investigate the total height of the MSDRA on the lower boundary of the highlighted region. It can be seen that effective-permittivity curves on the lower values have effectively shortened the antenna's height. In Fig. 5.7(a), it can be seen that the curve of '$\epsilon_1 = 2.2, \epsilon_2 = 9.2, \epsilon_3 = 16.0$' (green colour) touches the highlighted region at total height of 10 mm, where d_2 has the height of 4.5 mm.

In order to further analyse MSDRA, the upper-segment's height, d_3, is varied from 1 to 10 mm, whereas height (d_2) of the middle segment is kept constant at 2.5 mm, as shown in Fig. 5.7(b). Rest of the arrangement similar as mentioned earlier. In this figure, it shows that the same curve of '$\epsilon_1 = 2.2, \epsilon_2 = 9.2, \epsilon_3 = 16.0$' (green colour) touches the highlighted region at total height of 9.3 mm instead of 10 mm.

In the Fig. 5.7(a) & (b), d_1 is kept constant at 3.0 mm. Therefore, in order to examine the effect of varying height of the lower segment ($\epsilon_1 = 2.2$), the height of d_1 in Fig. 5.8(a) & (b) is decreased to 2.5 mm. The height of the middle and upper segments, in Fig. 5.8(a), are 1-10 mm and 2.5 mm, respectively. Analogously, the height of the middle and upper segments, in Fig. 5.8(b), are 2.5 mm and 1-10 mm, respectively.

In order to choose the best combination, it is clear from all plots indicated in Fig. 5.8 that the curves of '$\epsilon_1 = 2.2, \epsilon_2 = 6.2, \epsilon_3 = 16.0$' (red colour) and '$\epsilon_1 = 2.2, \epsilon_2 = 6.2, \epsilon_3 = 12.0$' (blue colour) are approaching the effective permittivity of 5.0 at higher values of the total height of the MSDRA as compared to the other two combinations. Thus the combination of '$\epsilon_1 = 2.2, \epsilon_2 = 9.2, \epsilon_3 = 16.0$' and '$\epsilon_1 = 2.2, \epsilon_2 = 9.2, \epsilon_3 = 12.0$' will be investigated further.

Comparing Fig. 5.7 (a) and (b), it is evident that variation in upper segment, d_3, reduced the height of the MSDRA to 9.2 mm whereas middle segment, d_2, attained the lowest height of 10 mm at effective permittivity of 5.0. On the other hand, further

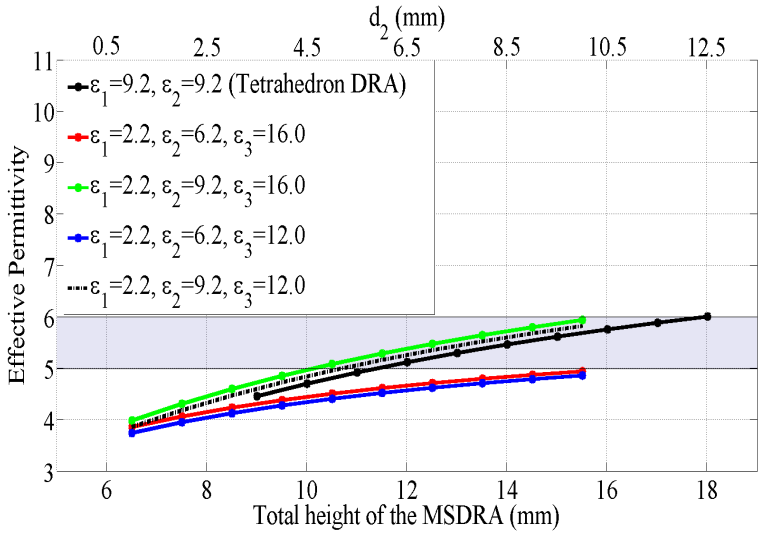

(a) d_1=3.0 mm, d_2=1 to 10 mm, d_3=2.5 mm

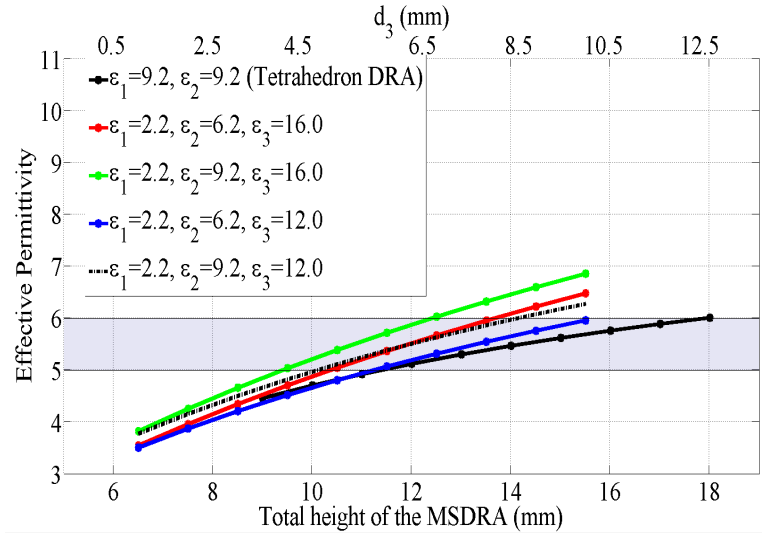

(b) d_1=3.0 mm, d_2=2.5 mm,d_3=1 to 10 mm

Figure 5.7: Total height of the MSDRA with respect to the tetrahedron DRA (a) Case 1 (b) Case 2

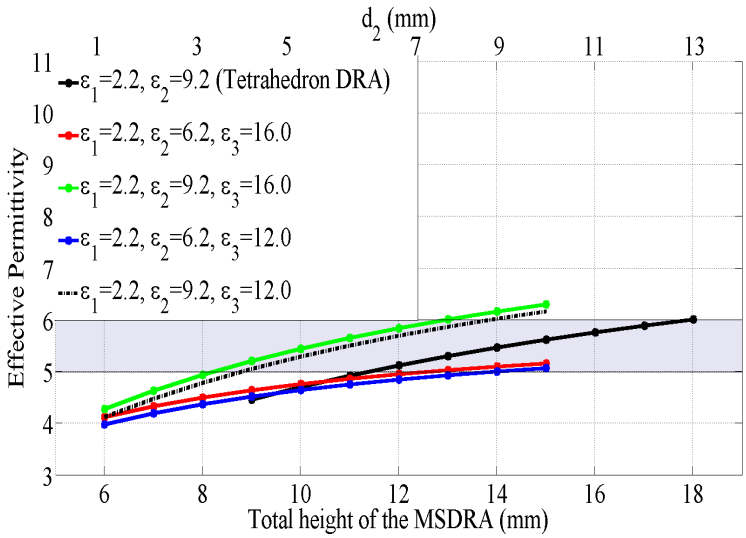

(a) d_1=2.5 mm, d_2=1 to 10 mm, d_3=2.5 mm

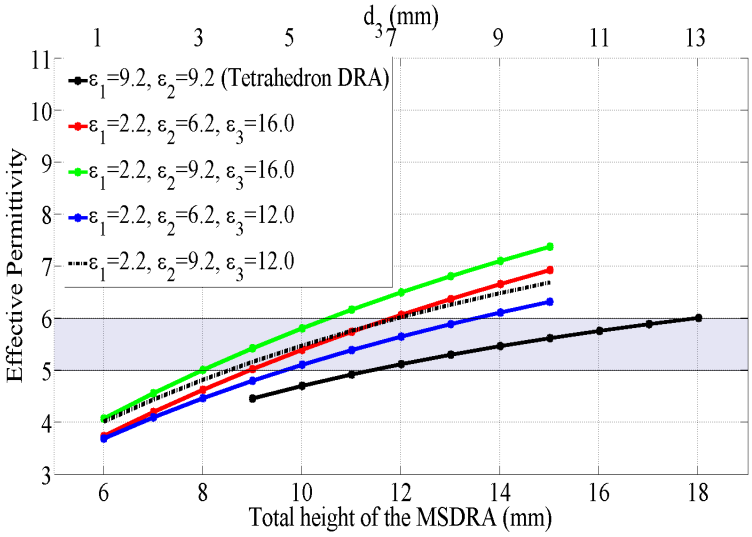

(b) d_1=2.5 mm, d_2=2.5 mm,d_3=1 to 10 mm

Figure 5.8: Total height of the MSDRA with respect to the tetrahedron DRA (a) Case 3 (b) Case 4

decreasing the height of lower segment, d_1, substantially reduced the height of the MSDRA, as shown in Fig. 5.8 (a) and (b). This study has identified that the best combination is '$\epsilon_1 = 2.2, \epsilon_2 = 9.2, \epsilon_3 = 16.0$', which leads to the total height of 8 mm. However, solely analysing the effective permittivity and height of the antenna cannot demonstrate wide impedance bandwidth characteristics. Nevertheless, this technique helps to approximate the height of MSDRA. Therefore, further investigation has been done in the following order: 1) optimisation of aspect ratio and height, 2) Q factor.

5.3.3 Aspect Ratio

The aspect ratio of the MSDRA can be used to reduce the volume-to-surface ratio, and reducing this particular ratio decreases the Q factor. In this way, the impedance bandwidth of the MSDRA can be enhanced. Before proceeding it is worth mentioning that the height of the MSDRA was further reduced from 8 mm to 7.1 mm; this consider a minor degradation in the impedance bandwidth. In addition, by applying the conducting wall the MSDRA was cut in half without compromising the bandwidth of the full-size MSDRA. Therefore the conducting wall was considered and the height of the MSDRA was kept constant while investigating its aspect ratio.

5.3.4 Q factor

Since the rectangular-shaped DRAs have two degrees of freedom, aspect ratios bandwidth performance was analysed by sweeping the length, a, and width, b. Fig. 5.9 shows the reflection coefficient magnitude of nine varied dimensions. It can be seen that increasing the length of the MSDRA enhances the return loss at lower frequencies. However, the impedance bandwidth has significantly shrunk at the upper limit. Some dimensions effectively transform the MSDRA into a dual-band antenna and - since the main objective was to attain contiguous bandwidth over a wide bandwidth of operation - only contiguous

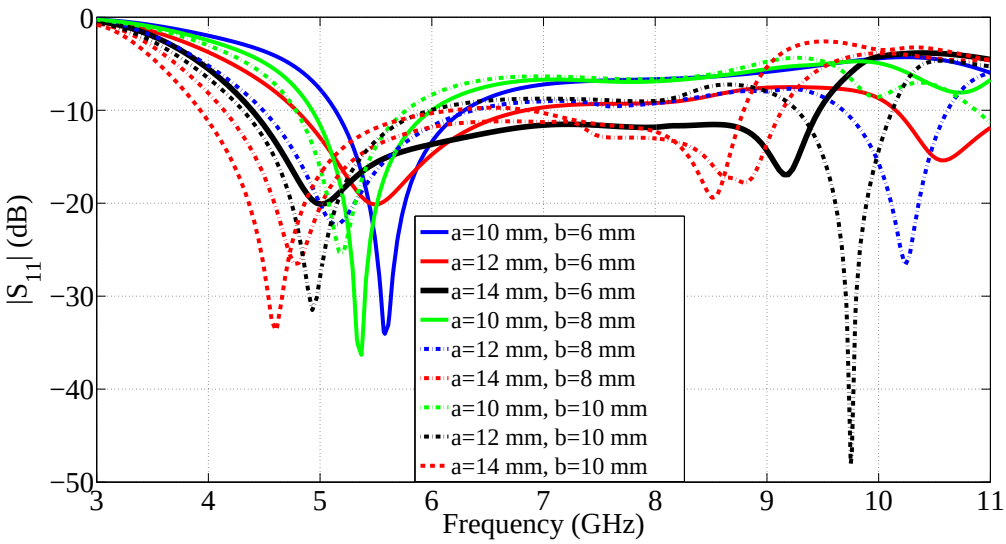

Figure 5.9: The effect of the aspect ratio on the input reflection of the MSDRA

wideband curves were considered for further investigation.

The aspect ratio of the MSDRA with 14.0 × 6.0 mm^2 cross-section is expected good matching between 4.4 and 9.47 GHz. Analogously, 14.0 × 8.0 mm^2 cross-section shows the good return loss in the 4.1-9.1 GHz range. It should be noted that as the length-to-width ratio decreases, the 10-dB return loss bandwidth shrinks with the exception of the 14.0 × 8.0 mm^2 curve. In fact, the cross-section of the 14.0 × 6.0 mm^2 curve reveals that the MSDRA has attained a wider bandwidth. Hence the optimized geometry of the MSDRA is 14.0 × 6.0 × 7.1 mm^3.

In order to validate the results of the previous section, the mean Q factor and the standard deviation was computed with different permittivities of the upper segment. As shown in Table 5.4, the MSDRA demonstrates a similar trend to the tetrahedron DRA. It is observed that increasing the permittivity of the upper segment increased both the mean Q factor of the MSDRA and the standard deviation. The Q factor's higher fluctuation leads to impedance mismatch and consequently in poorer bandwidth performance, as shown in Fig. 5.10. It emerged that a standard deviation greater than 1.55 led to a

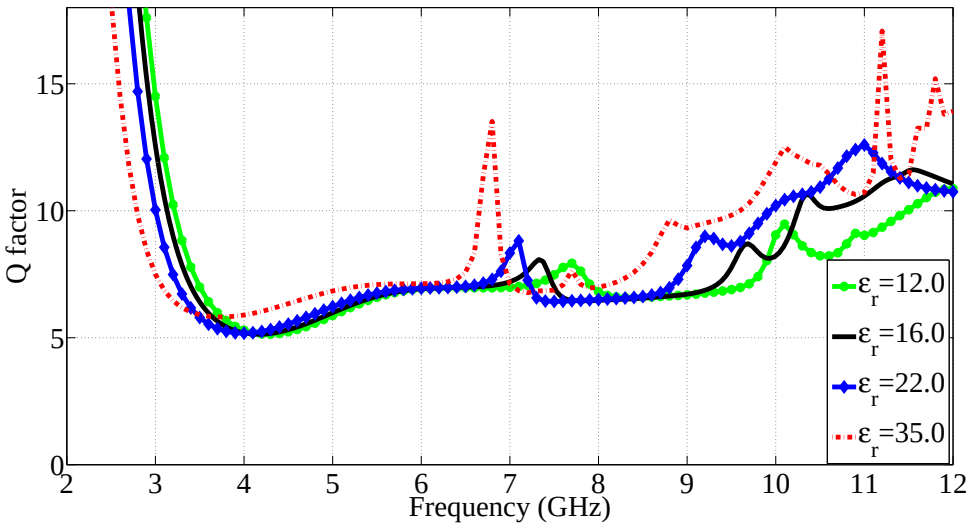

(a)

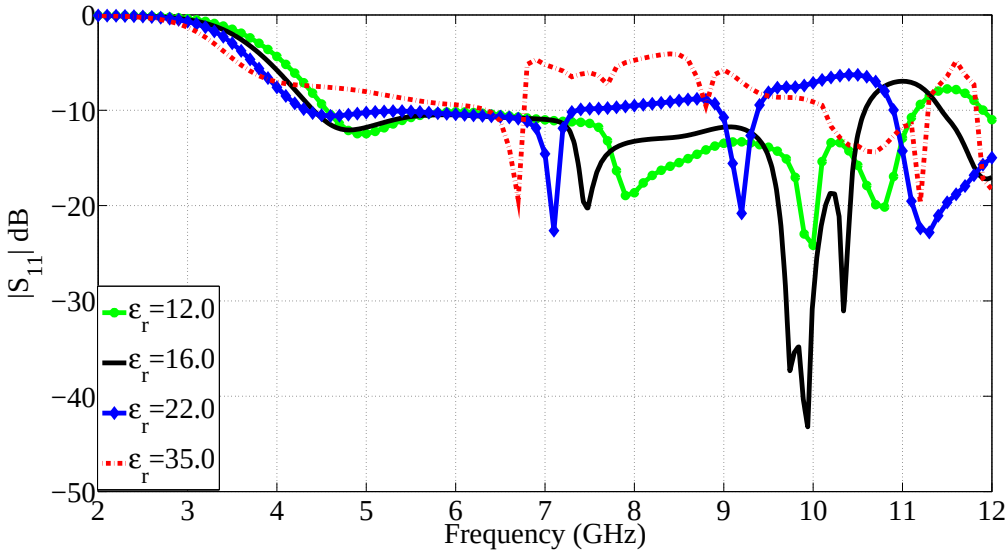

(b)

Figure 5.10: (a) Predicted Q factor of the MSDRA for different permittivities of ε_{DR}, (b) Predicted $|S_{11}|$ of the MSDRA for different permittivities of ε_{DR}

deterioration in the wide impedance bandwidth. The standard deviation is lowest at ε_3=12.0 and it is found that wide impedance bandwidth is achievable. However, due to unavailability of the material, the dielectric constant of 16.0 is used in the final design.

Table 5.4: Mean Q-factor and Standard Deviation of different permittivities of the upper segment

ε_r	Mean (Q-factor)	Standard Deviation
12.0	6.95	1.00
16.0	7.2	1.51
22.0	7.47	1.84
35.0	8.11	2.02

5.3.5 Copper Patches and Air region

Having optimized the aspect ratio, to further enhance the impedance bandwidth an air region was introduced in the middle segment of the MSDRA. The introduction of the air region is the same concept that was applied in Chapter 3 to reduce the effective permittivity of the antenna. Fig. 5.11 represents the comparison of reflection coefficient magnitude of the MSDRA without the air region, with the air region, and with the air region and the copper patches, respectively. It can be seen that introducing the air region has significantly disturbed return loss between 7.2 and 9.4 GHz.

In order to rectify this situation, two rectangular copper patches were sandwiched between the lower segment and the middle segment. This is feasible only when dielectric segments are placed in a stack arrangement. In MSDRAs, the coupling between the probe and different dielectric segments is inefficient and thus copper patches are inserted to improve the coupling between different dielectrics.Rigorous analysis was conducted to

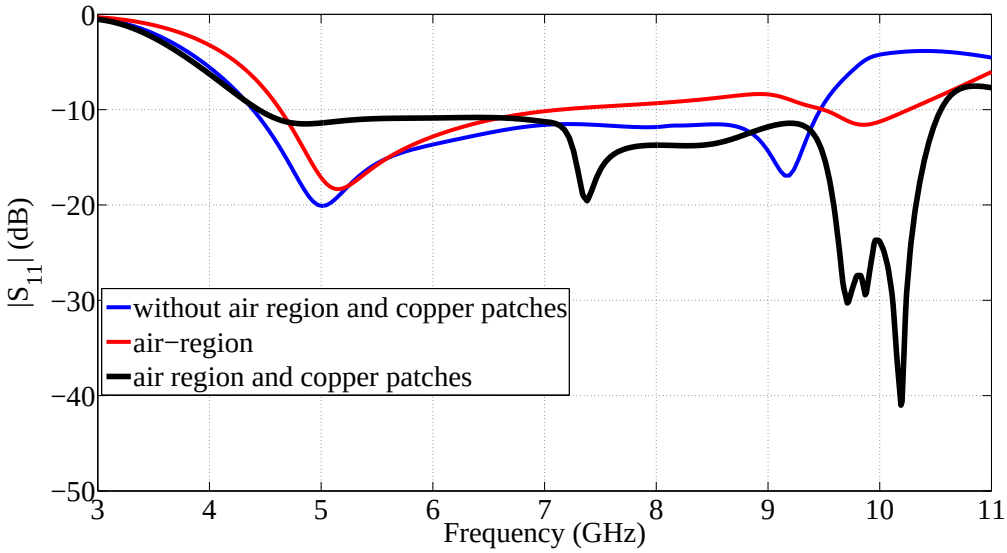

Figure 5.11: The effect of the air region and the copper patches on antenna input impedance

optimise the position of copper patches. It was found that there should be no physical contact between the copper patches and probe to achieve good impedance bandwidth. Fig. 5.12 shows the E-field distribution of MSDRA with and without Copper patches. It can be seen that placement of Copper patches allow the current to flow on the surface of MSDRA, thus improving the coupling of energy with the probe feed. Fig. 5.11 shows that a 10 dB return-loss computed with the copper patches and the air region has substantially enhanced the input matching over the entire band of operation.

During the analysis it was found that the impedance bandwidth is highly sensitive to the placement of the copper patches and the air region. For this reason a number of parametric analyses were undertaken to locate the best position of the copper patches and air region. It was found that the effect of air region in Duriod 5880 deteriorated the upper band of frequencies whereas the introduction of air region inside TAP-OPTICS significantly disturbed the impedance bandwidth from both lower and upper band of

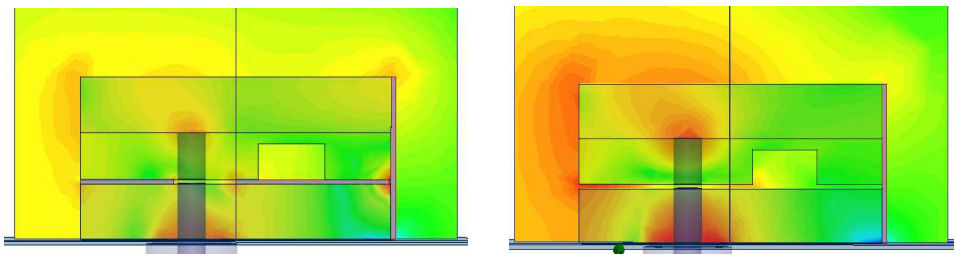

(a) With Copper patches (b) Without Copper patches

Figure 5.12: E-field distribution of MSDRA with and without copper patches

frequencies. However, air region in TMM10 showed the good return loss bandwidth, which is employed in the final design of MSDRA. Furthermore, the position and the height of probe were tuned to obtain the desired results. It was noted that physical contact between the probe and the copper patches significantly deteriorated the input matching of the antenna. As a result, copper patches have been intentionally separated from the probe.

5.4 Fabrication and measured results

A prototype as shown in Fig. 5.13, was fabricated. The shape of the rectangular air region was precisely cut from the middle segment to avoid undesirable changes in Q factors and resonance frequencies. In addition, thin air gaps between the feed and lower segment or between any two successive segments significantly degraded the antenna's bandwidth performance. The copper tape that was used as the conducting wall was evenly bonded to the dielectric segments and the ground plane. It was found that minute pockets of air gap could compromise antenna operation at some frequency points.

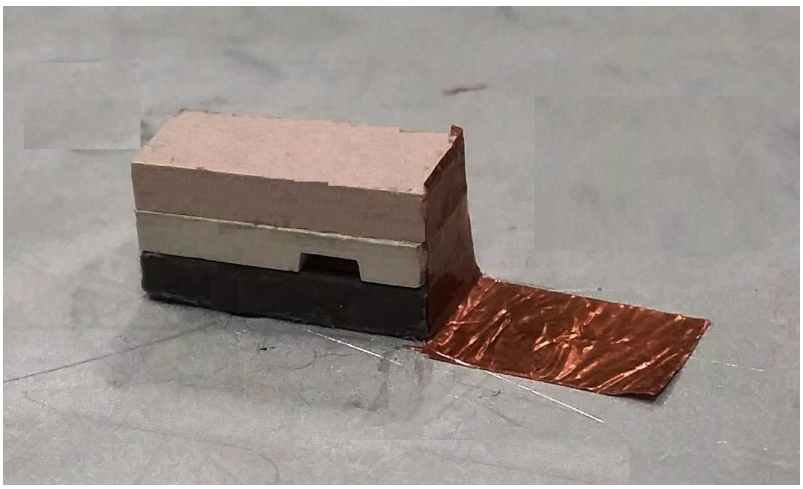

(a)

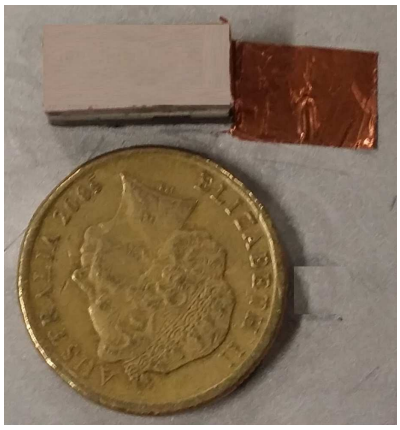

(b)

Figure 5.13: A prototype of the wideband MSDRA

5.4.1 Reflection Coefficient

The voltage standing wave ratio (VSWR) was measured using an N5242A Vector Network Analyser. The measured and predicted VSWR of the antenna is shown in Fig. 5.28. The measured VSWR bandwidth (VSWR < 2) is 82.7%, 4.4 - 10.6 GHz. Comparing the results, it can be seen that the measured VSWR agrees well with the predicted values. Unlike the predicted VSWR, the measured VSWR shows an impedance mismatch at 10.5

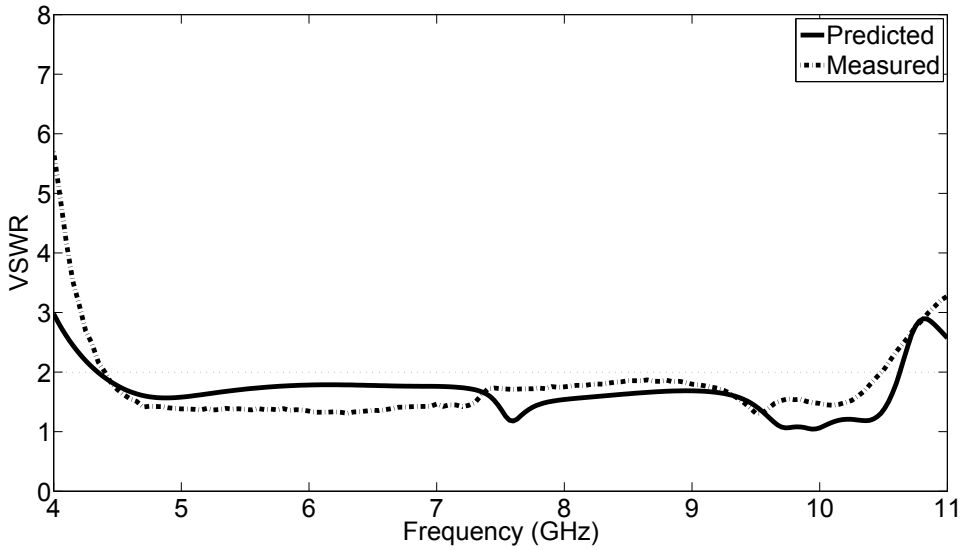

Figure 5.14: Measured and predicted VSWR of the MSDRA

GHz. Minor variations between the two are attributed to fabrication tolerances including possible air gaps between multiple interfaces.

5.4.2 Gain and Radiation Pattern

The gain and radiation characteristics were measured in the NSI-700S-50 spherical near-field measurement system at the Australian Antenna Measurement Facility (AusAMF). The peak realized gain of the MSDRA, measured from 4 to 11 GHz, is shown in Fig. 5.15. The measured gain varies between 4.5 and 7.1 dBi across the operating frequency band. The difference between the measured and predicted peak realized gain between 4.5 - 10.6 GHz is in the 1.2 - 1.7 dBi range. These varied results are there due to the fabrication imperfections and minute air gaps existing between the dielectric segments. As described in the previous chapter, mean realized gain is usually a useful measure for wideband antennas. Therefore, mean realized gain was also computed in elevation planes to assess the mean gain in different directions from 4 -11 GHz. Fig. 5.16 shows the

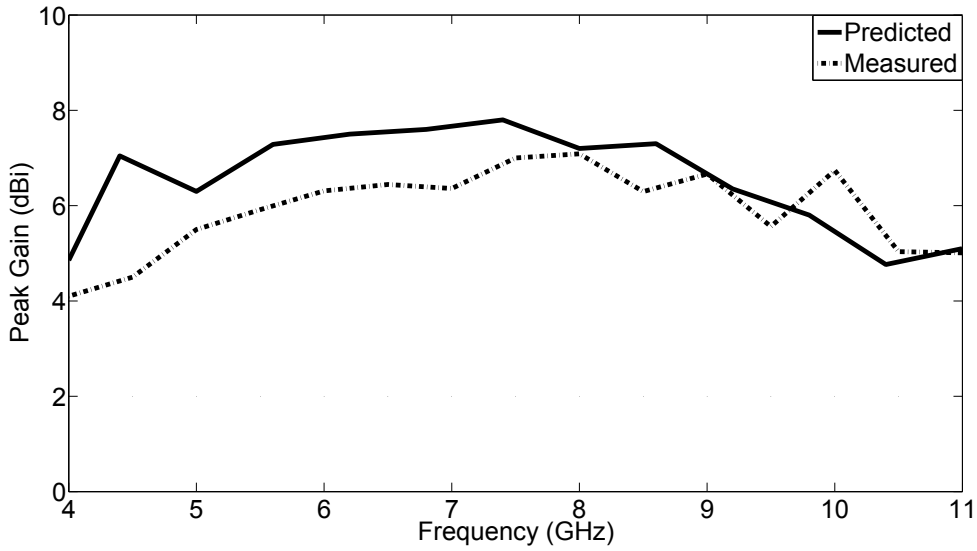

Figure 5.15: Measured and predicted realized peak gain of the MSDRA

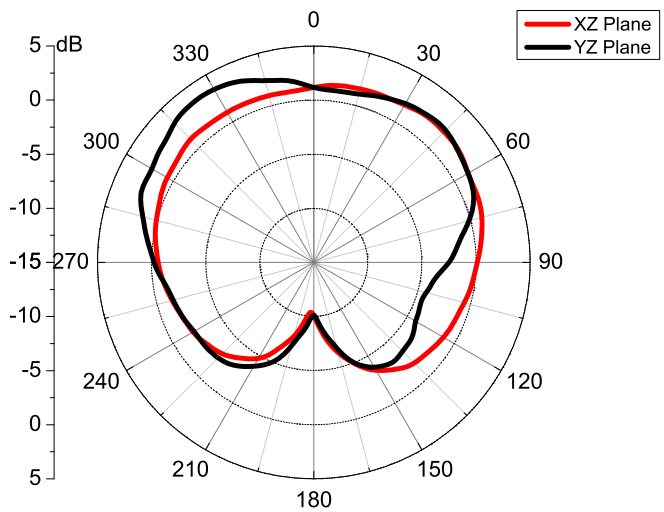

Figure 5.16: Predicted mean realized gain of the MSDRA

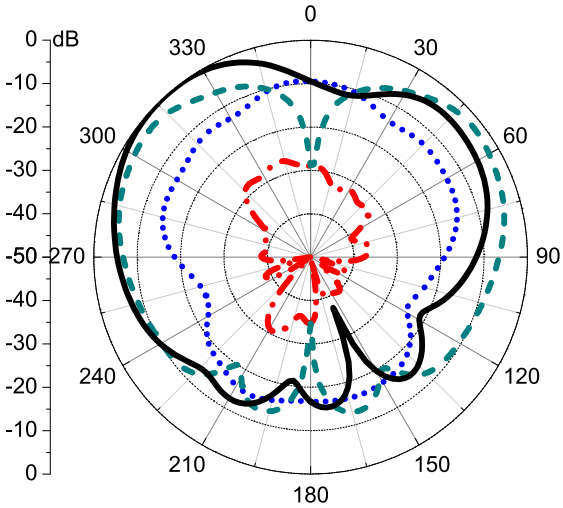

(a) Far-field pattern at 5 GHz

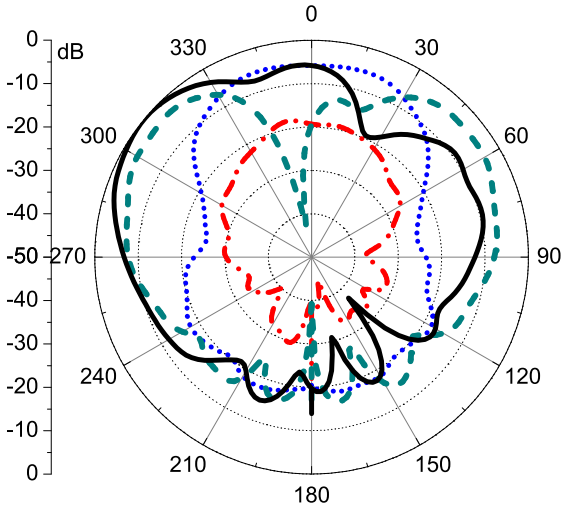

(b) Far-field pattern at 7 GHz

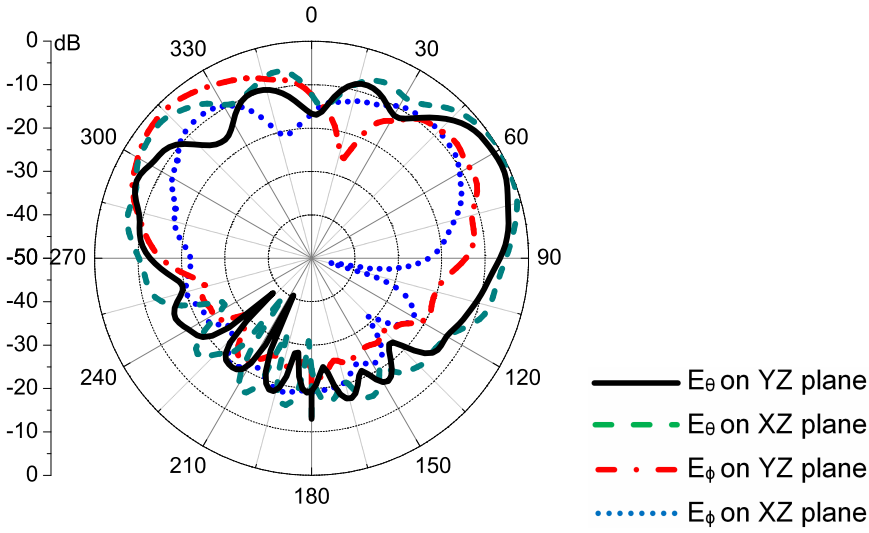

(c) Far-field pattern at 9 GHz

Figure 5.17: Computed radiation patterns of the presented DRA

computed mean realized gain in the XZ and YZ plane. It was found that mean realized gain of approximately 3.5 dBi is obtained in several directions.

Figs. 5.17 and 5.18 show the computed and measured radiation patterns at three different frequencies (5, 7, and 9 GHz), showing a reasonable agreement. It is clear that

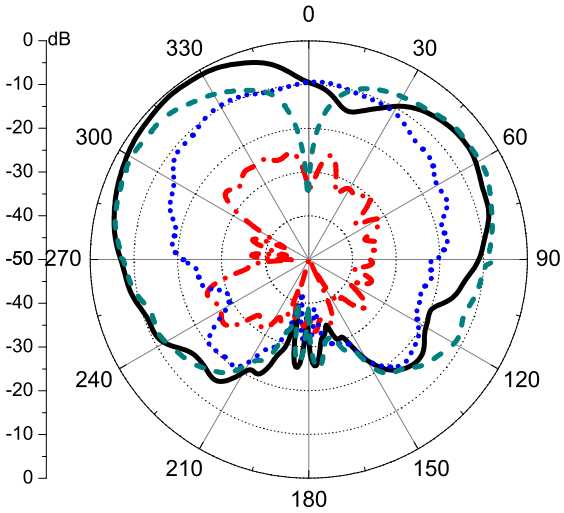

(a) Far-field pattern at 5 GHz

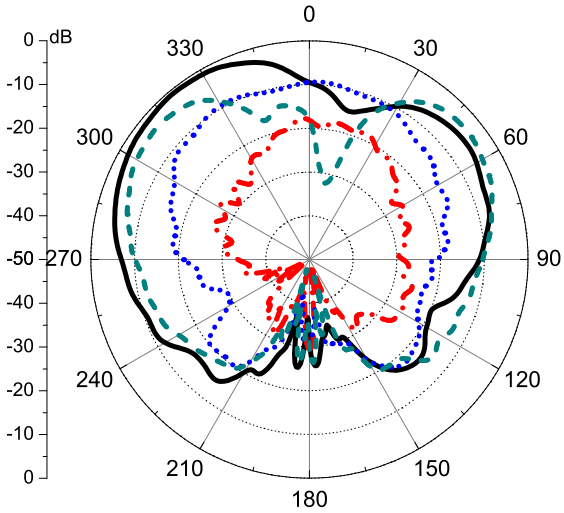

(b) Far-field pattern at 7 GHz

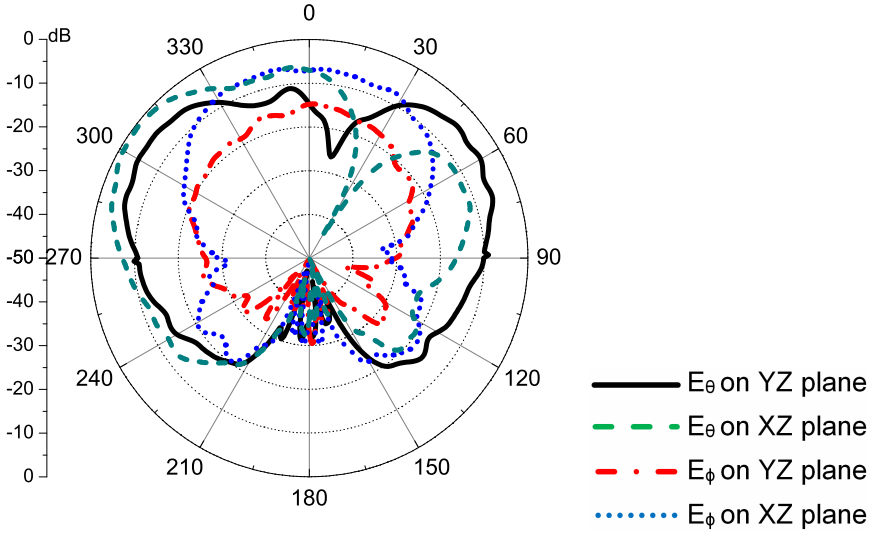

(c) Far-field pattern at 9 GHz

Figure 5.18: Measured radiation patterns of the presented DRA

this DRA radiates reasonably well in all directions in the upper hemisphere. When one polarization component is weak (e.g., E_θ in $\theta = 0^o$ direction), the orthogonal component is sufficiently strong. It can be seen that computed and measured patterns at 5 and 7 GHz are more consistent compared to the 9 GHz. At higher frequencies, the electric size of

DRA becomes larger which leads to excite higher order modes in the DRA and therefore it causes ripples and high-cross polar level.

This is unlike printed planar UWB antennas which have partial or no ground planes, and therefore they do radiate significantly and unnecessarily to the lower hemisphere. This DRA has been designed with a full ground plane to reduce this wastage.

In the XZ plane, the E_θ pattern is almost symmetrical in the operating frequency range. However, the pattern on the orthogonal YZ plane changes with frequency because different dielectric resonance modes become dominant as the frequency is swept.

So far above-mentioned sections have focused on improving the bandwidth-to-volume ratio of the MSDRA. In Table 5.5, dimensions, volume, surface area and measured impedance bandwidth values are compared between the tetrahedron DRA and MSDRA. It is evident that bandwidth-to-volume ratio of the MSDRA rose by 73.67%. Moreover, a decrease in the volume-to-surface ratio (V/S) supports the claim for a decline in the overall Q factor of the antenna.

Table 5.5: Comparison of bandwidth-to-volume ratio between the tetrahedron DRA and MSDRA

Structure	Dimensions a x b x d (mm^3)	Surface Area (mm^2)	Volume (mm^3)	V/S	Measured Imepdance Bandwidth (GHz), %	Bandwidth-to-volume ratio (GHz/mm^3)	Enhancement of Bandwidth-to-volume ratio %
Tetrahdron-DRA	12 x 8 x 15	792	1440	1.82	3.1-11.6, 116 %	0.0059	---
MSDRA	14 x 6 x 7.2	456	604.8	1.33	4.4-10.6, 83 %	0.0103	73.67

Most of the wireless electronic devices have large conducting platforms, similar to a full ground-plane, where the MSDRA can be easily installed. The main purpose of the full ground plane is to redirect most of the power to the upper hemisphere and in this

way to reduce wastage of power going to the lower hemisphere.

At this stage, the investigation of the ground plane was not part of this study. Therefore, the next section will rigorously investigate the effects of the ground plane on the MSDRA's bandwidth performance.

5.5 A Wideband MSDRA with Miniaturized Ground Plane

In this section, the effect of the ground plane on the MSDRA is analysed in order to reduce the size of the ground plane. The motivation behind for this work was to use the MSDRA for wireless electronic devices which have limited space but also requiring high-date-rate communication. Apart from examining the effect of the ground plane on the antenna performance, the size of the ground plane has been significantly reduced and a return loss bandwidth is improved from 82.7% to 94%.

5.5.1 Miniaturization of Ground Plane Size

Before proceeding to examine the MSDRA with ground plane, it should be noted that the area of the ground plane, in the previous chapter, was 40×40 mm^2. The main objective of this investigation was to reduce the area of the ground plane without any deterioration of input matching. Therefore, extensive analysis on the size of the ground plane was undertaken. However, only those sizes were selected which have good return loss bandwidth over the entire frequency range. Fig. 5.19 illustrates the computed return loss bandwidth with different sizes of ground plane (g_y and g_x represent the length and width of the ground plane, respectively, as shown in Fig. 5.20). It is evident that reducing the g_x from 30 mm to 18 mm, while the value of g_y is kept constant at 40 mm, has a slight effect on the input matching of the antenna. However, the curve of

$g_x = 6\,mm, g_y = 40\,mm$ has substantially enhanced the return loss bandwidth from 3.7 - 10.2 GHz.

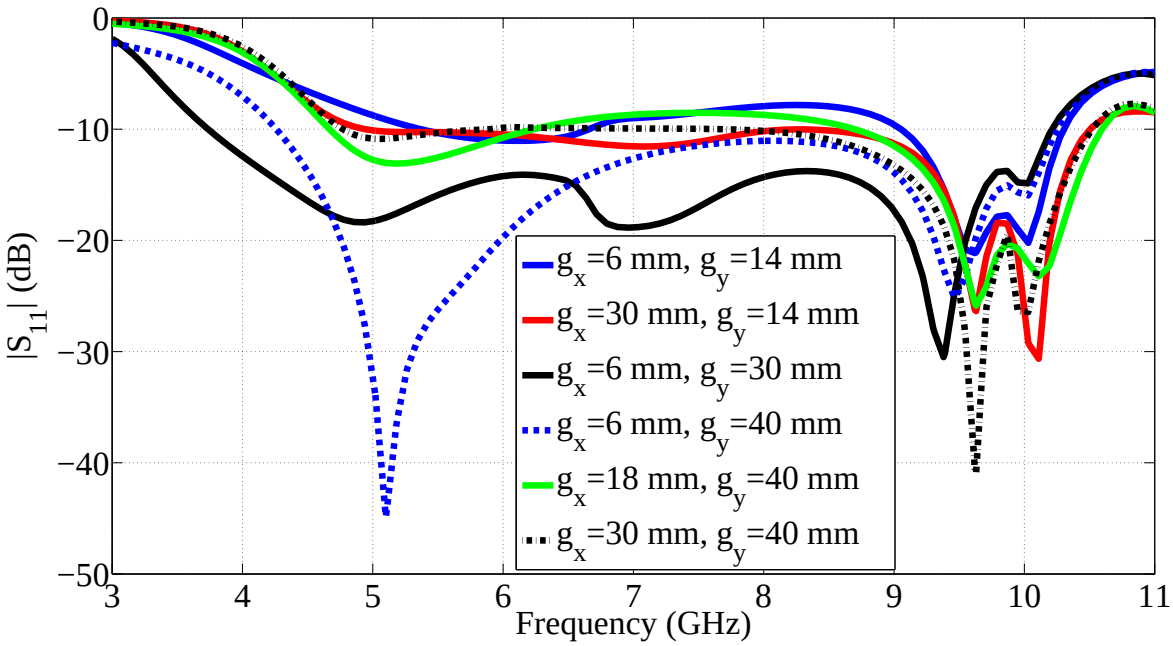

Figure 5.19: Computed return loss of the MSDRA with rectangular ground plane

On the other hand, keeping g_x constant at 6 mm and reducing g_y to less than 30 mm significantly deteriorates the return loss bandwidth. However, the ground plane with $g_x = 6\,mm, g_y = 30\,mm$ leads to the widest return loss bandwidth of 3.7 - 10.2 GHz among the ground planes considered. As a result, the length ($g_y = 30mm$) and width ($g_x = 6mm$) of the rectangular ground plane have been finalized, as shown in Fig. 5.20.

Compared to the tetrahedron DRA with full ground plane, the effect of the ground plane on the bandwidth performance of the MSDRA is less dependent on the size of the ground plane. It was found that reducing the size of the ground plane of tetrahedron DRA to less than 25×25 mm^2 considerably affected the input matching of the antenna. In fact the ground plane size of the MSDRA can be reduced up to 71 % with slight compromising of the UWB (0.6 GHz from lower band and 0.4 GHz from upper band)

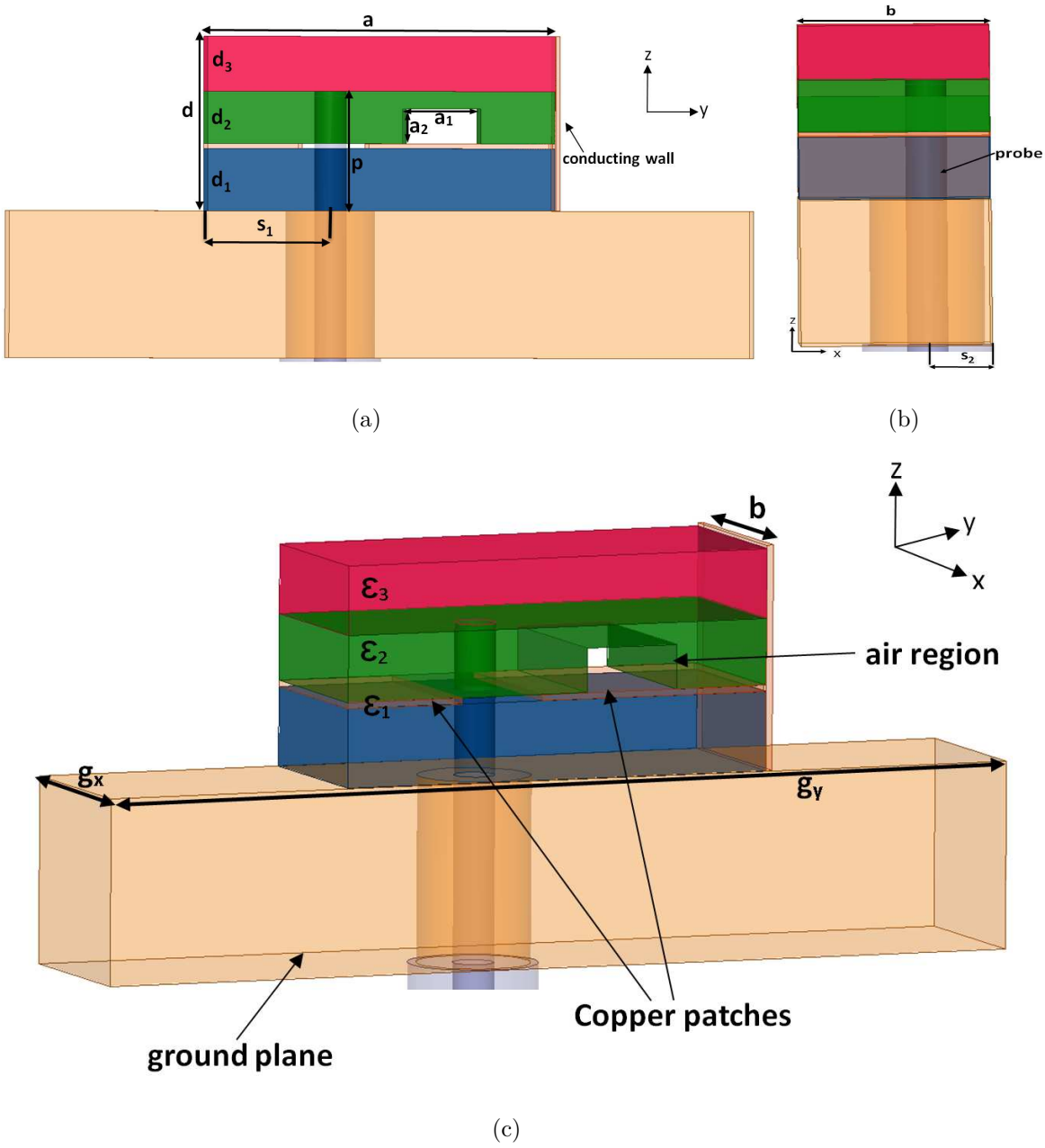

Figure 5.20: MSDRA configuration with small rectangular ground plane

return loss bandwidth. These computed results may be explained by the fact that the latter design has better coupling performance, due to a high dielectric constant of 16. Consequently a good return loss bandwidth is possible when the ground plane is of a miniaturized size.

5.5.2 Fabrication and Measured Results

To verify these results experimentally, the design of the small rectangular-shaped ground plane was fabricated and tested. The dielectric materials used for the MSDRA are Duriod 5880 ($\varepsilon_{r1} = 2.2$), TMM10 ($\varepsilon_{r2} = 9.2$) and TAP-Optics ($\varepsilon_{r3} = 16$). The uniqueness of this design is that it has a small ground plane when compared to the full ground plane. However, it can be seen from Fig. 5.20 (simulated design) and Fig. 5.21 (prototype) that the height of the ground plane is considerably large unlike the tetrahedron DRA. The reason for employing the towering ground plane was that the MSDRA required the additional height of the ground plane, to tighten an SMA connector with the help of screws. Therefore, the extra height of the ground plane has been added to the fabricated prototype.

The additional height of the ground plane has been introduced in the simulated design, and it emerged there is a negligible effect on the return loss bandwidth of the antenna. It means this antenna can be integrated into a multitude of wireless communication devices without adding more height to the ground plane. The overall size of the MSDRA is 14 mm long, 6 mm wide and 7.3 mm tall. Compared to the tetrahedron DRA with full ground plane, the height of the DRA is significantly reduced by up to 51.3%. Analogously, the area of the ground plane has shrunk by up to 71%.

Figure 5.21: A prototype of MSDRA with rectangular ground plane

Input Matching

Fig. 5.22 exhibits the computed and measured VSWR of the optimal design of the MSDRA. It can be observed that VSWR ≤ 2 bandwidth of 94% is achieved from 3.7-10.2 GHz.

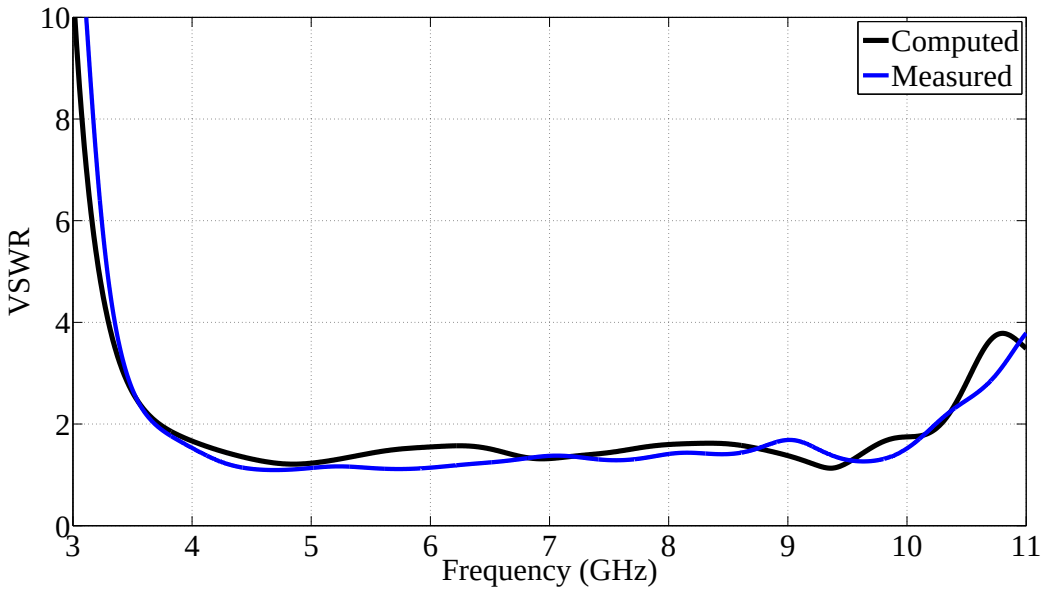

Figure 5.22: Measured and computed VSWR of the MSDRA with small rectangular ground plane

Gain and Radiation Patterns

The peak realized gain of the MSDRA with miniaturized ground plane, measured from 3 to 11 GHz, is shown in Fig. 5.23. At lower frequencies (3.7 - 7 GHz), the value of the predicted and measured realized gain lie between 2.5 and 5 dBi. From 7 GHz and onward, the peak realized gain is almost stable, hovering around 5.1 dBi, and this indicates a good agreement between the predicted and measured results.

Mean realized gain (MRG) of the MSDRA with miniaturized ground plane was computed to assess the mean gain in XZ and YZ planes, as shown in Fig. 5.24. It can be seen that MRG of 3.5 dBi is obtained in several directions. The uneven variation of MRG in YZ plane is due to the asymmetry of the structure.

Fig. 5.25 shows the computed radiation patterns of the MSDRA at 4, 7 and 9 GHz. It can be seen that in the XZ plane, E_θ has a null in boresight direction at 4 GHz and it

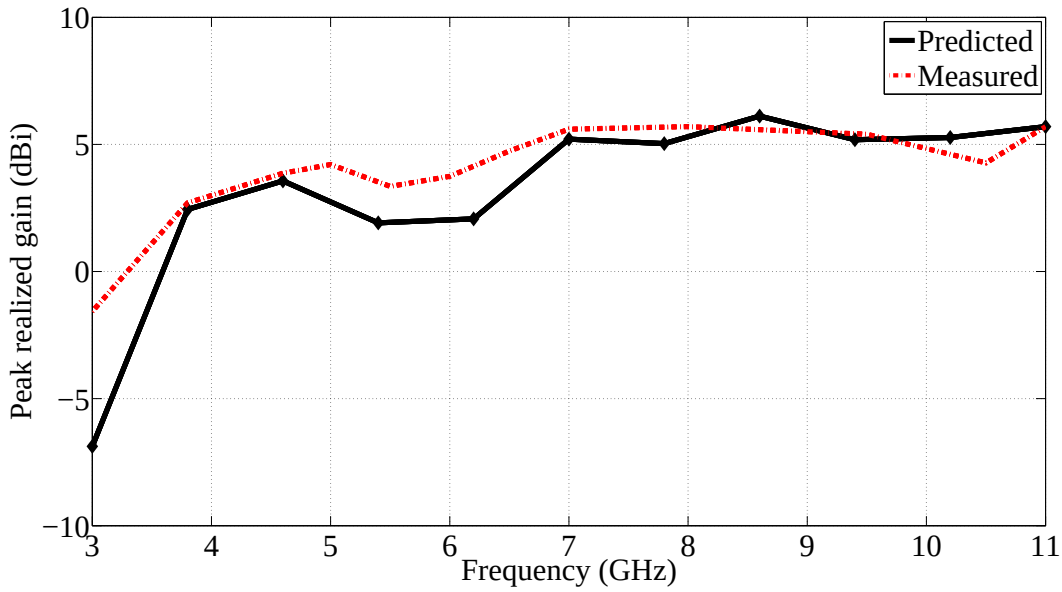

Figure 5.23: Predicted peak realized gain of the MSDRA with miniaturized rectangular ground plane

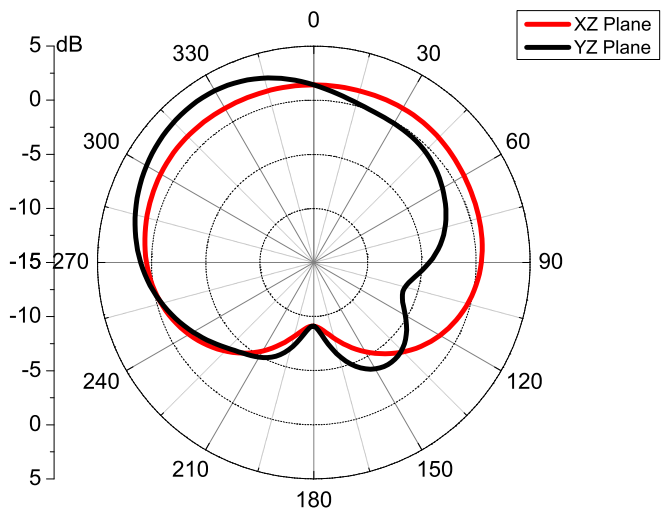

Figure 5.24: Predicted mean realized gain of the MSDRA with miniaturized rectangular ground plane

vanishes at higher frequencies. Nevertheless, E_ϕ has a strong polarization component and it is stable at the all above-mentioned frequency points. On the other hand, E_θ on YZ plane is nearly symmetrical in the upper hemisphere, however, orthogonal component of YZ changes with frequency and it becomes stronger at high frequencies. Such variation is typical in UWB antennas.

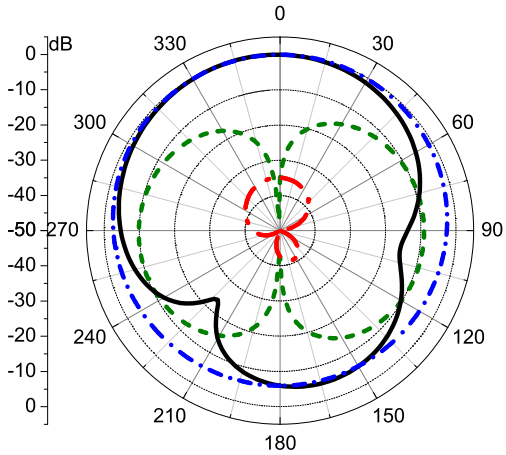

(a) Far-field pattern at 4 GHz

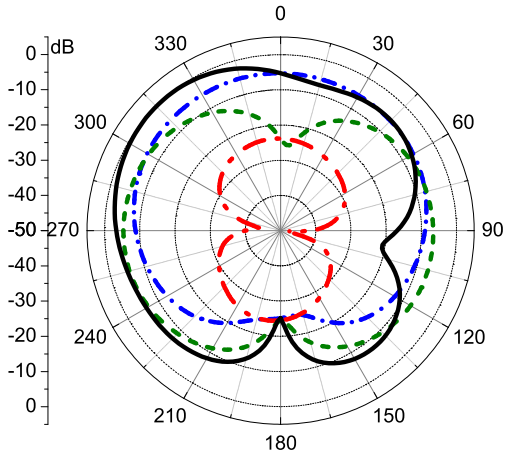

(b) Far-field pattern at 7 GHz

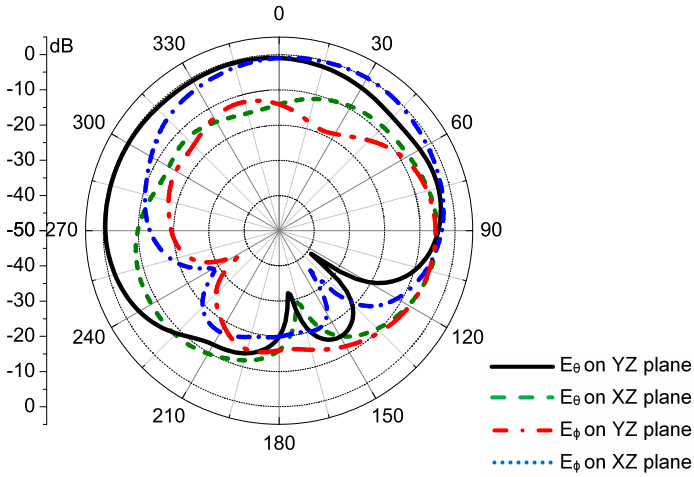

(c) Far-field pattern at 9 GHz

Figure 5.25: Computed normalized radiation patterns of the MSDRA with miniaturized rectangular ground plane

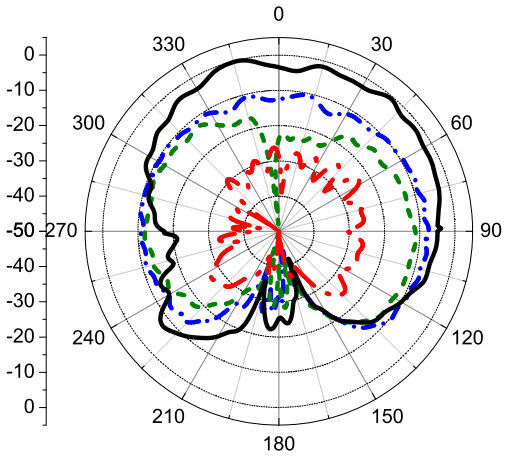

(a) Far-field pattern at 4 GHz

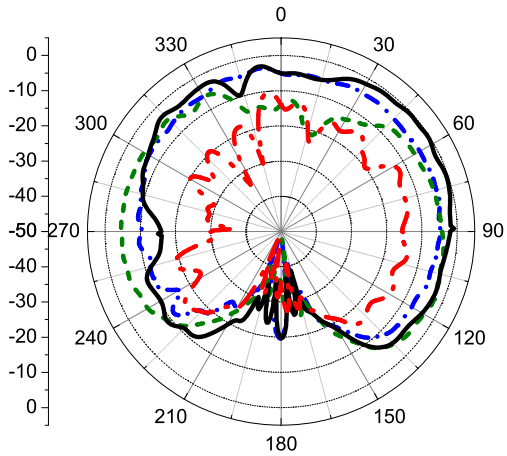

(b) Far-field pattern at 7 GHz

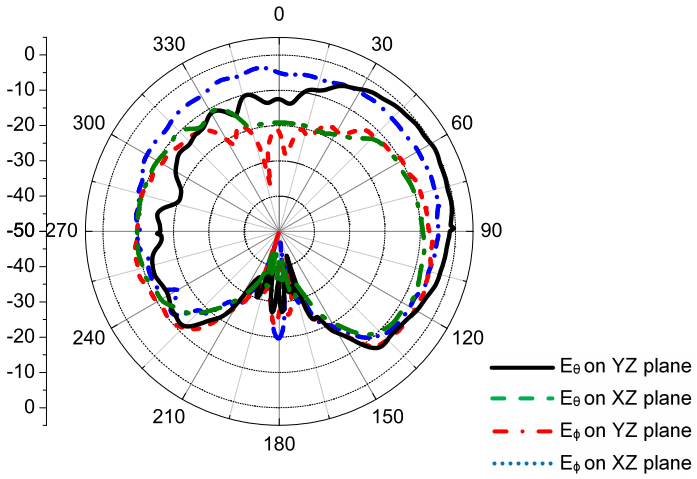

(c) Far-field pattern at 9 GHz

Figure 5.26: Measured normalized radiation patterns of the MSDRA with miniaturized rectangular ground plane

5.6 MSDRA with Miniaturized Rectangular Ground Plane for Medical Applications

5.6.1 Geometry and Antenna Design

Fig. 5.27 shows the geometry of the proposed antenna residing on a muscle phantom. The dimensions of the phantom are P_h, P_l , and P_w. The gap between the antenna and

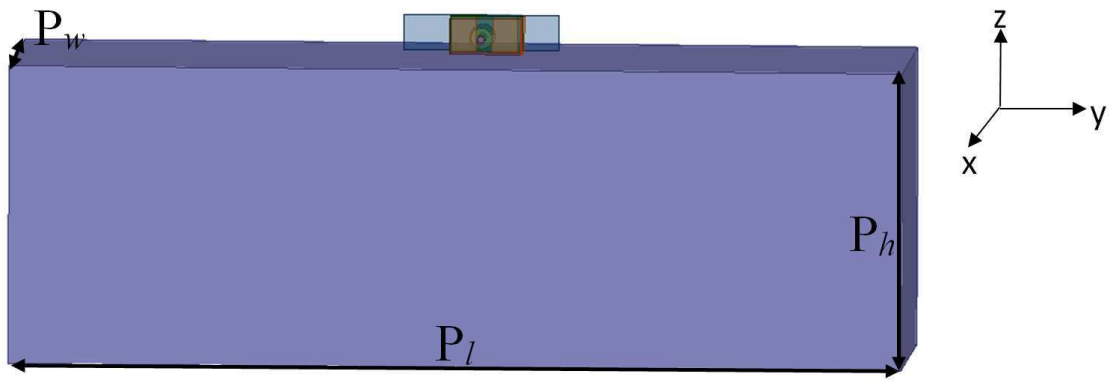

Figure 5.27: Antenna mounted on the muscle phantom

the phantom is set to 1 mm, which corresponds to a practical situation where antenna is mounted on clothes.

Modeling of phantom

In order to model accurately the antenna in the presence of the phantom, the dielectric properties of the phantom should be used in the UWB range. The muscle dielectric properties are well characterized up to 20 GHz [103]. For the numerical modeling, the complex dielectric permittivity ε^* of the phantom was expressed as a Debye dispersion given by [104]:

$$\varepsilon^* = \varepsilon_0(\varepsilon' - j\varepsilon'') = \varepsilon_0(\varepsilon_\infty + \frac{\varepsilon_s - \varepsilon_\infty}{1 + j\omega\tau}) \tag{5.6}$$

where ω is the angular frequency, ε_s is the static permittivity, ε_∞ is the optical permittivity, and τ is the relaxation time. The best fit of this theoretical model to the target values was obtained for $\tau = 12.5 \times 10^{-12}$, $\varepsilon_s = 37.1$, and $\varepsilon_\infty = 12.2$ [105]. Theoretical permittivity and conductivity model agree very well with target values over the considered frequency range.

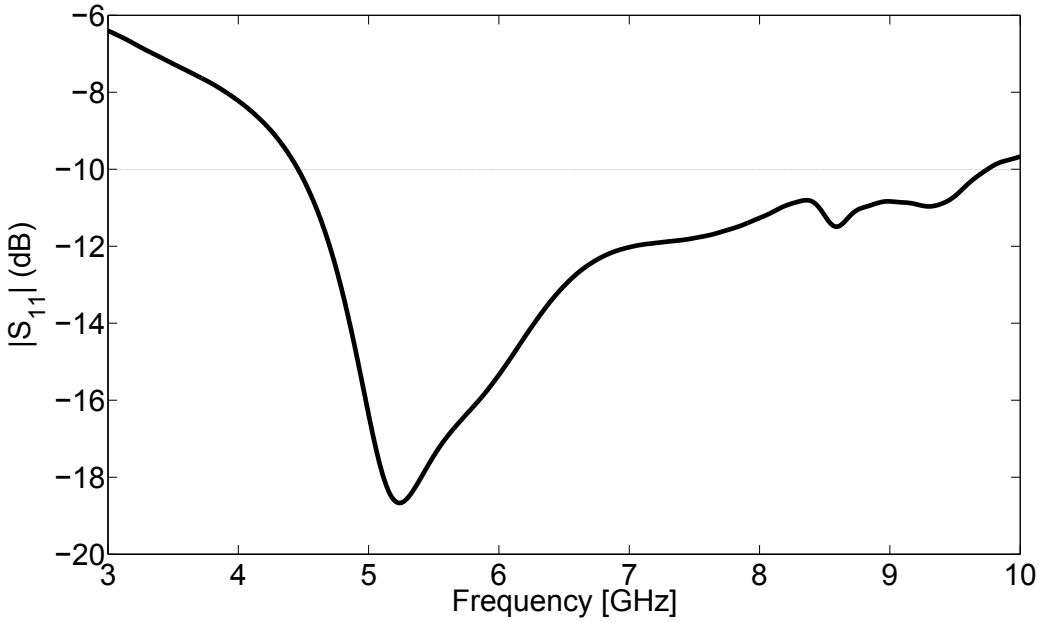

Figure 5.28: Computed input reflection coefficient of the proposed DRA mounted on the phantom

5.6.2 Results and Discussions

All calculations are carried out using the finite integration technique implemented in CST Microwave Studio [**?**]. In our investigation, the DRA was optimized to obtain a design to cover the part of the FCC UWB ($4.4 - 9.7$ GHz). The probe length of 4.8 mm ensures optimal impedance match to the 50 Ω coaxial cable. The computed reflection coefficient of the proposed antenna, shown in Fig. 5.28, indicates an impedance bandwidth of $4.4 - 9.7$ GHz with $|S_{11}| <$ -10 dB.

The proposed antenna has a peak gain of 7 dBi and its gain is between 0.2 dBi and 4.5 dBi over the impedance bandwidth, as shown in Fig. 5.29. The computed radiation patterns, with the 1 mm gap between the antenna and human body, are presented at three frequencies (5, 7, and 9 GHz) in Fig. 5.30. A constant pattern is imperative characteristics for a UWB antenna since it does not show very high dispersion associated with a pattern

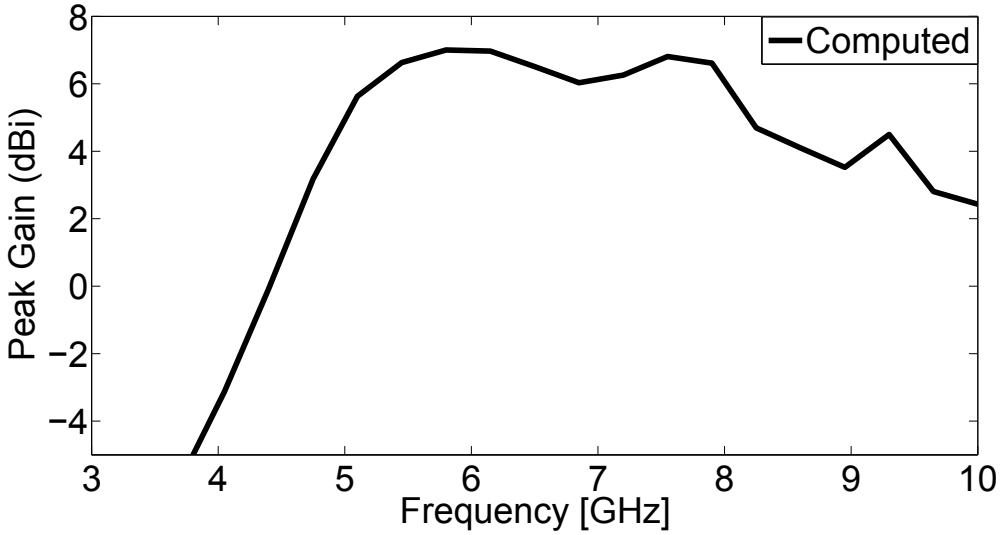

Figure 5.29: Computed realized peak gain of the proposed DRA

that varies with frequency. It can be observed that these radiation patterns are consistent over the operating band and most of the power is radiated away from the phantom.

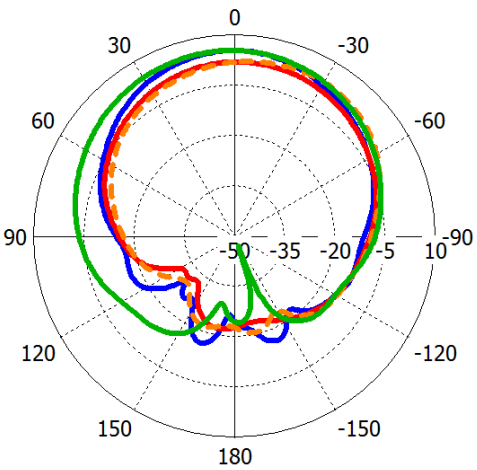

(a) Far-field pattern at 5 GHz

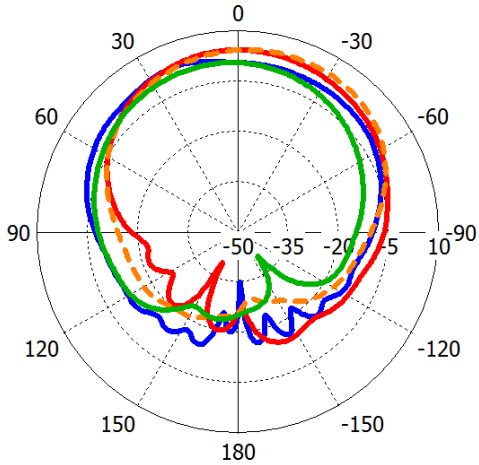

(b) Far-field pattern at 7 GHz

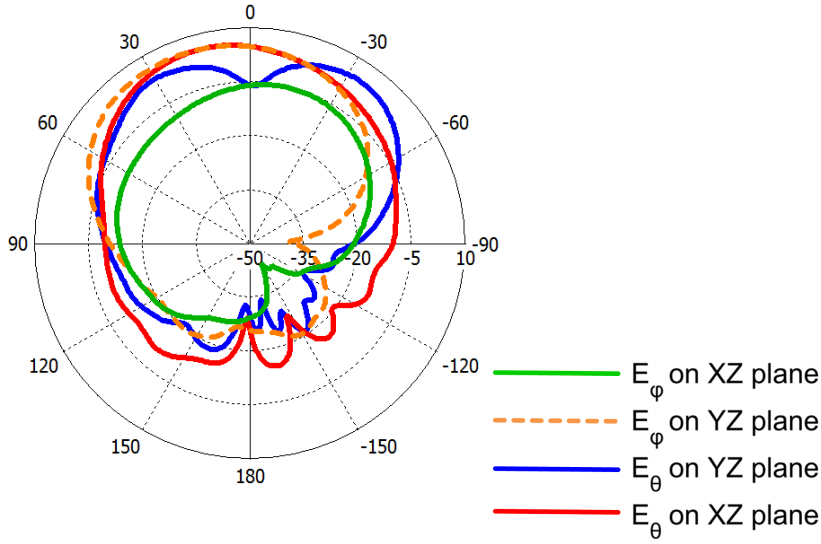

(c) Far-field pattern at 9 GHz

Figure 5.30: Computed radiation patterns of the presented DRA with phantom

5.7 Summary

This chapter described the design of a low-profile MSDRA that exhibits good antenna performance in an ultra-wide band. This MSDRA is made out of three different dielectric segments, fed by a probe, and resides on a full ground plane. Effective permittivity, Q factor and aspect ratio of the MSDRA were carried out in detail to enhance the bandwidth-to-size ratio of the MSDRA. The standard deviation of Q factor was crucial to optimize the contiguous impedance bandwidth of the MSDRA. The numerical and experimental results demonstrated a 10 dB return loss bandwidth of 82.7% from 4.4-10.6 GHz. The bandwidth-to-volume ratio of this DRA has been improved by 73.67% as compared to the UWB tetrahedron DRA. This design is suitable for high-data-rate personal area networks (PANs), especially used for consumer electronics and personal computing applications.

Furthermore, this chapter describes the design of a low-profile MSDRA with miniaturized ground plane, which demonstrates a good return loss in an ultra-wide band. This MSDRA consists of three different dielectric segments, fed by a probe, and resides on a miniaturized rectangular ground plane. A rigorous analysis has been conducted on the size of the ground plane in order to reduce its size. It is found that the MSDRA's ground plane size decreased by 71%, compared to the full ground plane used in the previous chapter. The numerical and measured results show a 10 dB return loss bandwidth of 94% from 3.7 - 10.2 GHz. In addition, this design was tested on numerical phantom for off-body communication, to cover a part of the FCC UWB band. The numerical results demonstrates a 10 dB return loss bandwidth from 4.4 - 9.7 GHz. The radiation patterns exhibit stable behaviour over the operating band. This design is suitable for high-date-rate electronic on-body devices used for off-body communication.

Chapter 6

Conclusions and Future Work

6.1 Summary and Findings

Based on the research presented in the dissertation, this chapter concludes by recapitulating key findings of the investigations and suggests potential avenues for further research.

The thesis investigated new techniques for designing and characterizing novel yet simple DRAs. It presented a comprehensive analysis of dual segment and multisegment DRAs of different sizes regarding ground plane for ultrawideband and wideband operations.

In Chapter 3, a UWB DRA with a full ground plane is investigated in terms of the frequency domain. The measured 2:1 VSWR bandwidth of this DRA is 115%, and it covers the whole FCC UWB band. It has a small footprint of 12×8 mm^2, or $0.124 \times\ 0.083\,\lambda_0^2$ at the lowest operating frequency of 3.1 GHz. Its dielectric volume is 1318.8 mm^3, or $1.45 \times 10^{-3}\,\lambda_0^3$, and its overall height is 15 mm or $0.155\,\lambda_0$. It was observed that the shape and location of an air region have a significant impact on antenna performance. Without an air region the best measured return loss is less than 10 dB at 6.2 and 8.3 GHz yet with an air region it is greater than 10 dB in the entire FCC UWB band. In addition, the impedance bandwidth of the DRA improves from 109.5% to 115% due to

the air region. The mean realized gain of the UWB DRA is 4.85 dBi and 4.91 dBi in the YZ and XZ planes, respectively. Radiation characteristics reveal that 90% of the power is radiated to the upper hemisphere and this subsequently reduces the wastage in the lower hemisphere. Compared to printed UWB antennas with partial or no ground plane, this UWB DRA does not have a null in the boresight direction. Due to the above reasons and its compactness, ease of excitation, minimal surface wave losses and excellent radiation characteristics, this design is suitable for high-data-rate consumer electronic devices, which are intended to transmit only in unidirectional mode.

Chapter 4 demonstrated time-domain characteristics of UWB DRA to assess its pulse performance through the use of several broadband pulses. It was observed that for both linearly-chirped Gaussian and fifth-order Gaussian pulses, the correlation between the radiated pulses and the input pulse is excellent in most directions. Nevertheless, when either of those pulses are radiated by this DRA, the EIRP spectrum produced by the antenna does not efficiently fill the FCC UWB mask. This limitation was addressed by introducing a third-order Rayleigh pulse and tuning it to generate an EIRP spectrum that fills the FCC mask well. In this way, total spectral efficiency of the antenna is significantly increased to 52% without overstepping FCC mask limits. Ground plane size has no significant effect on correlation as long as it is greater than 25 mm. Overall, however, correlation can be improved by optimising the air region's dimensions. The best correlation factor found with the optimal air region is 0.981. The average correlation in the two elevation planes is 0.823, and the average correlation factor in the azimuth plane is 0.931. To the best of our knowledge, no other DRA has better pulse-preserving characteristics in all important directions. It is expected that the high correlation factor in these directions will result in good bit-error-rate (BER) of IR UWB systems.

Chapter 5 presented a low-profile MSDRA consisting of three different dielectric segments, fed by a probe and residing on a full ground plane. The bandwidth-to-volume

ratio of MSDRA can be substantially enhanced by thoroughly examining its effective permittivity, Q factor and aspect ratio. The standard deviation of the Q factor was crucial for optimizing the contiguous impedance bandwidth of the MSDRA. The numerical and experimental results demonstrated a 10 dB return loss bandwidth of 82.7% from 4.4-10.6 GHz. The bandwidth-to-size ratio of this DRA has been improved by 73.67% compared to the UWB tetrahedron DRA. This design is suitable for high-data-rate personal area networks (PANs), which are especially used for consumer electronics and personal computing applications.

Furthermore, this chapter describes the design of a low-profile MSDRA with a miniaturized ground plane, demonstrating a good return loss in an ultra-wide band. This MSDRA consists of three different dielectric segments, fed by a probe, and resides on a miniaturized rectangular ground plane. A rigorous analysis has been conducted on the size of the ground plane in order to reduce its size. It is found that the MSDRA's ground plane size decreased by 71%, compared to the full ground plane used in the previous chapter. The numerical and measured results show a 10 dB return loss bandwidth of 94% from 3.7 - 10.2 GHz. Additionally, this design was tested on numerical phantom for off-body communication, to cover a part of the FCC UWB band. The numerical results demonstrate a 10 dB return loss bandwidth from 4.4 - 9.7 GHz. The radiation patterns exhibit stable behaviour over the operating band. This design is suitable for high-date-rate electronic on-body devices used for off-body communication.

The dissertation presented measured results of several antenna prototypes that were fabricated and tested to verify the design methodology. For all these prototypes, excellent input matching was achieved, however the dimensions of these antennas (DRAs) required a slight tuning, especially adjusting the probe's height and spacing between the ground plane and the DRA. Furthermore, the measured performance parameters of these antennas showed excellent agreement with the simulations. These antenna configurations are good

candidates for a myriad of advanced electronic devices, of miniaturized size, that require a high-data-rate communication for indoor communication.

6.2 Avenues for Future Work

This PhD research has resulted in a new UWB DRA, meticulously analysed in both time and frequency domains, and a low-profile MSDRA configuration. Nevertheless, further exploration needs to be done to improve the DRAs bandwidth-to-volume ratio in order to employ multifrequency, wideband and UWB communication systems. Some avenues for further research are suggested below:

- The time-domain characteristics of UWB DRA are extensively investigated by employing several analytical pulses. It has been shown that antennas pulse performance is quite well retained, however, EIRP is well below the FCC mask. It has been noted that the best EIRP mask is achieved by using third-order Rayleigh pulse. Nevertheless, EIRP performance can be improved by designing numerical pulses. Another way to effectively utilize the EIRP mask is to thoroughly investigate antennas' pulse response.

- The three-segment DRA, MSDRA, for wideband can be further reduced without compromising the impedance bandwidth. It can be made possible by further dividing the number of segments and optimising air region accordingly. The probes position is situated inside the DRA. However, the placement of the probe (in the form of a copper patch) can be employed to enhance further the impedance bandwidth.

- Work can be extended to investigate DRAs with electronic band gap (EBG) structures which can be help to achieve circularly-polarized DRA. In most cases, in order

to achieve circularly-polarized DRA, the structure of DRA is thoroughly modified to attain the axial ratio. However, using EBG, as a ground plane, with DRA can easily achieve the axial ratio bandwidth.

- Work can be extended to investigate DRAs with off-body communication, performance on real humans or complex phantoms and also DRAs in different encasing and within bigger structures.

Appendix A

Abbreviations

BER	Bit-Error-Rate
DRA	Dielectric Resonator Antenna
DR	Dielectric Resonator
EIRP	Effective Isotropic Radiated Power
FCC	Federal Communications Commission
IR	Impulse Radio
MSDRA	Multi-Segment Dielectric Resonator Antenna
MRG	Mean Realized Gain
HFSS	High Frequency Structure Simulator
LPI	Lower Permittivity Insert
UWB	Ultrawideband
VSWR	Voltage Standing Wave Ratio

Appendix B

List of Publications

Following is the list of my publications resulted from this research:

B.1 Journals:

B.1.1 Review Submit

[1] S. I. Mian and K. P. Esselle, *"Pulse-Preserving Characteristics and Effective Isotropically Radiated Power Spectra of a New Ultrawideband Dielectric Resonator Antenna"*, (Submitted in June 2015 to IEEE Transactions on Antennas & Propagation)

B.1.2 Submitting Soon

[2] S. I. Mian and K. P. Esselle, *"A low-profile Dielectric Resonator Antenna for wideband communication "*, (will be submitted in Jan 2016 to IEEE Transactions on Antennas & Propagation Letters)

B.2 Conference Paper

B.2.1 Submitted

[1] S. I. Mian and K. P. Esselle, *"A Low-profile Dielectric Resonator Antenna for Wideband Applications "*, (submitted in Jan 2015 to IEEE AP−S Symposium on Antennas and Propagation and URSI CNC/USNC 2015, Canada)

[2] S. I. Mian and K. P. Esselle, *"Comparative Analysis of broadband pulses for an UWB DRA "*, (submitted in July 2015 to IEEE International Symposium on Antennas and Propagation (ISAP) 2015, Hobart, Tasmania, Australia)

B.2.2 Published

[1] S. I. Mian, Yuehe Ge, K. P. Esselle, *"Bandwidth enhancement of Dielectric Resonator Antenna "*, (presented in Feb 2013 to Thirteenth Australian Symposium on Antennas, Sydney, Australia, 13 - 14 Feb. 2013)

[2] S. I. Mian, Yuehe Ge, K. P. Esselle, *"Miniaturization of Dielectric Resonator Antenna for Biomedical Applications "*, (presented in Jan 2013 to IEEE AP−S Symposium on Antennas and Propagation and URSI CNC/USNC 2013, Orlando, USA)

[3] S. I. Mian, Yuehe Ge, K. P. Esselle, *"An Antenna with Small Footprint, Small Volume, and Full Ground Plane for UWB Systems "*, (presented in Sep 2013 to IEEE INTERNATIONAL CONFERENCE ON ULTRA-WIDEBAND, 15-18 SEPTEMBER 2013 SYDNEY, AUSTRALIA)

[4] S. I. Mian and K. P. Esselle, *"Pulse performance of a UWB Dielectric Resonator Antenna "*, (presented in Jan 2014 to IEEE AP−S Symposium on Antennas and Propagation and URSI CNC/USNC 2014, Memphis, TN, USA)

[5] S. I. Mian and K. P. Esselle, *"A Compact Wideband Dielectric Resonator Antenna for On-Body Applications "*, (presented in Dec 2014 to IEEE MTT-S IEEE International Microwave Workshop Series on RF and Wireless Technologies for Biomedical and Healthcare Applications 8 10 Dec 2014 — London, United Kingdom)

[6] S. I. Mian and K. P. Esselle, *"A Low-profile Dielectric Resonator Antenna for Wideband Applications "*, (submitted in Jan 2015 to IEEE AP−S Symposium on Antennas and Propagation and URSI CNC/USNC 2015)

[7] S. I. Mian and K. P. Esselle, *"Time-Domain Characterization of a UWB Dielectric Resonator Antenna Excited by a Third-Order Rayleigh Pulse "*, (submitted in Jan 2015 to Fourteenth Australian Symposium on Antennas, Sydney, Australia, 2015)

Appendix C

Radiation Pattern Measurements and Setup

Several prototypes of ultrawideband and wideband DRAs were fabricated and presented in this thesis. The following sections present the radiation pattern measurement and setup. These photographs were not shown in the main body of the thesis.

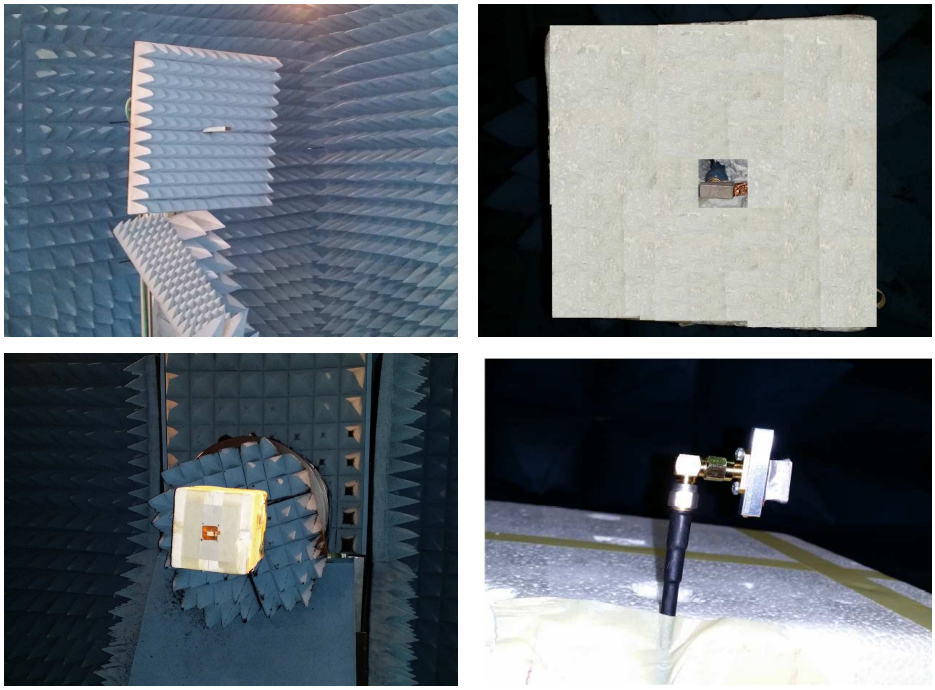

Figure C.1: Australian Antenna Measurement Facility (AusAMF) located at CSIRO ICT center in Marsfield, Sydney. Measurements are done using a NSI-700S-50 spherical near-field antenna system with standard test probes and gain horns

Bibliography

[1] R. M. T and A. M. Emergence of Ceramic Dielectric Resonators in Wireless Communication. [Online]. Available: http://www.wirelessdesignmag.com/

[2] M. Sebastian, *Dielectric materials for wireless communication*, 1st ed. Elsevier, 2008.

[3] R. Mark. FCC Approves First Commercial UWB Chipset. [Online]. Available: http://www.wi-fiplanet.com

[4] R. M. T and A. M. Belkin First in Industry to Announce Aftermarket Product Based on Certified Wireless USB. [Online]. Available: http://www.businesswire.com/

[5] [Online]. Available: http://www.audioholics.com/news/wireless-lcd-tv-announced-by-haier-freescale

[6] R. Kranenburg and S. Long, "Microstrip transmission line excitation of dielectric resonator antennas," *Electronics Letters*, vol. 24, no. 18, pp. 1156–1157, Sep 1988.

[7] A. Petosa, N. Simons, R. Siushansian, A. Ittipiboon, and M. Cuhaci, "Design and analysis of multisegment dielectric resonator antennas," *IEEE Trans. Antennas Propag.*, vol. 48, no. 5, pp. 738–742, 2000.

[8] Y. R. S. M. Abbas, A. K. Verma, and K. P. Esselle, "A Simple Ultra Wideband Printed Monopole Antenna With High Band Rejection and Wide Radiation Patterns," *IEEE Trans. Antennas Propag.*, vol. 62, no. 9, pp. 4816–4820, Sept red2014.

[9] K. P. E. Yogesh Ranga, Anand K. Verma and S. G. Hay, "An ultra-wideband quasi-planar antenna with enhanced gain," *Progress in Electromagnetics Research*, vol. 49, 59, 65, 2014.

[10] B. Peterson. Spectrum Analysis Basics. Agilent Technologies. Application Note 150. [Online]. Available: www.agilent.com/find/SA

[11] "FCC. Title 47, Section 15 of the Code of Federal Regulations."

[12] Aiello, *WiMedia Alliance*, Std., 2008. [Online]. Available: http://www.wimedia.org/en/index.asp

[13] H. Schantz, *The Art and Science of Ultra-Wideband Antennas.* Artech House Print on Demand; 1St Edition edition, July 31, 2005.

[14] A. Okaya and L. F. Barash, "The Dielectric Microwave Resonator," *Proceedings of the IRE*, vol. 50, no. 10, pp. 2081–2092, 1962.

[15] A. Petosa, *Dielectric Resonator Antenna Handbook.* Artech House Antennas and Propagation Library, 2007.

[16] A. B. P. Kumar, R.K Shukla, "An accurate determination of Q-factor of a dielectric resonator in suspended substrate enviornment," *Microwave and Optical Technology Letters*, vol. 14, pp. 128–130, 1997.

[17] S. Long, M. McAllister, and S. Liang, "The resonant cylindrical dielectric cavity antenna," *Antennas and Propagation, IEEE Transactions on*, vol. 31, no. 3, pp. 406–412, 1983.

[18] M. W. McAllister, S. A. Long, and G. L. Conway, "Rectangular dielectric resonator antenna," *Electronics Letters*, vol. 19, no. 6, pp. 218–219, 1983.

[19] M. W. McAllister and S. A. Long, "Resonant hemispherical dielectric antenna," *Electronics Letters*, vol. 20, no. 16, pp. 657–659, 1984.

[20] R. K. Mongia, A. Ittipiboon, Y. M. M. Antar, P. Bhartia, and M. Cuhaci, "A half-split cylindrical dielectric resonator antenna using slot-coupling," *IEEE Microwave and Guided Wave Letters*, vol. 3, no. 2, pp. 38–39, 1993.

[21] G. Junker, A. Kishk, A. Glisson, and D. Kajifez, "Effect of air gap on cylindrical dielectric resonator antenna operating in TM01 mode," *Electronics Letters*, vol. 30, no. 2, pp. 97–98, Jan 1994.

[22] K. W. Leung, K. M. Luk, E. K. N. Yung, and S. Lai, "Characteristics of a low-profile circular disk DR antenna with very high permittivity," *Electron. Lett.*, vol. 31, no. 6, pp. 417–418, 1995.

[23] K. P. Esselle, "A low-profile rectangular dielectric-resonator antenna," *IEEE Antennas Propag. Mag.*, vol. 44, no. 9, pp. 1296–1297, 1996.

[24] D. Kajfez, *Dielectric Resonators*, 2nd ed. SciTech Publishing, December 1998.

[25] A. Petosa, A. Ittipiboon, Y. M. M. Antar, D. Roscoe, and M. Cuhaci, "Recent advances in dielectric-resonator antenna technology," *IEEE Antennas Propag. Mag.*, vol. 40, no. 3, pp. 35–48, 1998.

[26] L. K. Hady, D. Kajfez, and A. A. Kishk, "Dual function of a dielectric resonator: A high-Q resonator and a low-Q radiator," in *Microwave Symposium Digest, 2008 IEEE MTT-S International*, 2008, pp. 1011–1014.

[27] K. S. Ryu and A. A. Kishk, "Ultrawideband Dielectric Resonator Antenna With Broadside Patterns Mounted on a Vertical Ground Plane Edge," *Antennas and Propagation, IEEE Transactions on*, vol. 58, no. 4, pp. 1047–1053, 2010.

[28] A. Petosa and A. Ittipiboon, "Dielectric Resonator Antennas: A Historical Review and the Current State of the Art," *Antennas and Propagation Magazine, IEEE*, vol. 52, no. 5, pp. 91–116, 2010.

[29] Y. Pan, K. Leung, and K. Lu, "Compact Quasi-Isotropic Dielectric Resonator Antenna With Small Ground Plane," *Antennas and Propagation, IEEE Transactions on*, vol. 62, no. 2, pp. 577–585, Feb 2014.

[30] S. Fakhte, H. Oraizi, R. Karimian, and R. Fakhte, "A New Wideband Circularly Polarized Stair-Shaped Dielectric Resonator Antenna," *Antennas and Propagation, IEEE Transactions on*, vol. 63, no. 4, pp. 1828–1832, April 2015.

[31] R. Chair, A. Kishk, and K. Lee, "Wideband stair-shaped dielectric resonator antennas," *Microwaves, Antennas Propagation, IET*, vol. 1, no. 2, pp. 299–305, April 2007.

[32] H. Wei and A. A. Kishk, "Compact Dielectric Resonator Antenna Array for Microwave Breast Cancer Detection," in *Region 5 Technical Conference, 2007 IEEE*, 2007, pp. 9–12.

[33] M. Abedian, S. Rahim, and M. Khalily, "Two-Segments Compact Dielectric Resonator Antenna for UWB Application," *Antennas and Wireless Propagation Letters, IEEE*, vol. 11, pp. 1533–1536, 2012.

[34] E. K. I. Hamad and H. A. Atallah, "Bandwidth improvement of compact high permittivity RDRA using parasitic conducting strips," in *Antennas and Propagation (EUCAP), 2012 6th European Conference on*, 2012, pp. 1–4.

[35] R. K. Chaudhary, K. V. Srivastava, and A. Biswas, "Four element multilayer cylindrical dielectric resonator antenna excited by a coaxial probe for wideband applications," in *Communications (NCC), 2011 National Conference on*, 2011, pp. 1–5.

[36] "Revision of Part 15 of the Commissions Rules Regarding Ultra-Wideband Transmission Systems, First Report & Order, Washington DC," Adopted 14 Feb 2002, Released 22 April 2002.

[37] R. Richtinger, "Dielectric Resonators," *Journal of Applied Physics*, vol. Vol.10, pp. pp.391–398, 1939.

[38] R. K. Mongia and B. Bhat, "Accurate resonant frequencies of cylindrical dielectric resonators using a simple analytical technique," *Electronics Letters*, vol. 21, no. 11, pp. 479–480, 1985.

[39] G. Junker, A. Kishk, A. Glisson, and D. Kajfez, "Effect of an air gap around the coaxial probe exciting a cylindrical dielectric resonator antenna," *Elect. Lett.*, vol. 30, no. 3, pp. 177–178, Feb 1994.

[40] R. K. Mongia, A. Ittipiboon, M. Cuhaci, and D. Roscoe, "Radiation Q-factor of rectangular dielectric resonator antennas: theory and experiment," in *Proc. IEEE Antennas Propag. Soc. Int. Symp.*, vol. 2, 1994, pp. 764–767.

[41] S. M. Shum and K. M. Luk, "Characteristics of dielectric ring resonator antenna with an air gap," *Electronics Letters*, vol. 30, no. 4, pp. 277–278, 1994.

[42] R. K. Shukla and A.Biswas, "Coupling between offset layered dielectric resonator in suspended substrate," *Microwave and Optical Technology Letters*, vol. 11, pp. 51–53, 1996.

[43] R. K. Mongia, A. Ittibipoon, and M. Cuhaci, "Low profile dielectric resonator antennas using a very high permittivity material," *Electronics Letters*, vol. 30, no. 17, pp. 1362–1363, 1994.

[44] K. W. Leung and K. M. Luk, "Circular dielectric resonator antenna of high dielectric constant for low-profile applications," in *Antennas and Propagation, 1995., Ninth International Conference on (Conf. Publ. No. 407)*, 1995, pp. 517–519 vol.1.

[45] K. Esselle, "A low-profile rectangular dielectric-resonator antenna," *Antennas and Propagation, IEEE Transactions on*, vol. 44, no. 9, pp. 1296–1297, 1996.

[46] M. Cooper, "Investigation of Current and Novel Rectangular Dielectric Resonator Antenna for Broadband Applications ar L-band Frequencies," Master's thesis, Carleton University, 1997.

[47] S. M. Shum and K. M. Luk, "Stacked annular ring dielectric resonator antenna excited by axi-symmetric coaxial probe," *IEEE Antennas Propag. Mag.*, vol. 43, no. 8, pp. 889–892, 1995.

[48] G. Almpanis, C. Fumeaux, and R. Vahldieck, "Semi-trapezoidal dielectric resonator antenna for wideband applications," in *Antennas and Propagation Society International Symposium, 2007 IEEE*, June, pp. 4877–4880.

[49] K. K. So and K. W. Leung, "Bandwidth enhancement and frequency tuning of the dielectric resonator antenna using a parasitic slot in the ground plane," *Antennas and Propagation, IEEE Transactions on*, vol. 53, no. 12, pp. 4169–4172, 2005.

[50] O. M. H. Ahmed, A. R. Sebak, and T. A. Denidni, "Compact UWB printed monopole loaded with dielectric resonator antenna," *Electron. Lett.*, vol. 47, no. 1, pp. 7–8, 2011.

[51] A. A. Kishk, "Directive dielectric resonator antenna excited by probe or narrow slot," in *Radio and Wireless Symposium (RWS), 2012 IEEE*, 2012, pp. 387–390.

[52] A. Ittipiboon, A. Petosa, D. Roscoe, and M. Cuhaci, "An investigation of a novel broadband dielectric resonator antenna," in *Antennas and Propagation Society International Symposium, 1996. AP-S. Digest*, vol. 3, 1996, pp. 2038–2041 vol.3.

[53] T. A. Denidni, W. Zibin, and M. Niroo-Jazi, "Z-Shaped Dielectric Resonator Antenna for Ultrawideband Applications," *Antennas and Propagation, IEEE Transactions on*, vol. 58, no. 12, pp. 4059–4062, 2010.

[54] A. S. Al-Zoubi, A. A. Kishk, and A. W. Glisson, "Aperture Coupled Rectangular Dielectric Resonator Antenna Array Fed by Dielectric Image Guide," *Antennas and Propagation, IEEE Transactions on*, vol. 57, no. 8, pp. 2252–2259, 2009.

[55]

[56] G. Yong-Xin and L. Kwai-Man, "Dual-polarized dielectric resonator antennas," *Antennas and Propagation, IEEE Transactions on*, vol. 51, no. 5, pp. 1120–1124, 2003.

[57] K. S. Ryu and A. A. Kishk, "UWB Dielectric Resonator Antenna Having Consistent Omnidirectional Pattern and Low Cross-Polarization Characteristics," *Antennas and Propagation, IEEE Transactions on*, vol. 59, no. 4, pp. 1403–1408, 2011.

[58] Y. Ge, K. P. Esselle, and T. S. Bird, "Compact Dielectric Resonator Antennas With Ultrawide 60-110% Bandwidth," *IEEE Trans. Antennas Propag.*, vol. 59, no. 9, pp. 3445–3448, 2011.

[59] R. K. Mongia, "Theoretical and experimental resonant frequencies of rectangular dielectric resonators," *Microwaves, Antennas and Propagation, IEE Proceedings H*, vol. 139, no. 1, pp. 98–104, 1992.

[60] L. Bin and L. Kwok Wa, "Strip-fed rectangular dielectric resonator antennas with/without a parasitic patch," *Antennas and Propagation, IEEE Transactions on*, vol. 53, no. 7, pp. 2200–2207, 2005.

[61] G. Almpanis, C. Fumeaux, and R. Vahldieck, "The Trapezoidal Dielectric Resonator Antenna," *IEEE Antennas Propag. Mag.*, vol. 56, no. 9, pp. 2810–2816, 2008.

[62] J. Van Bladel, "On the Resonances of a Dielectric Resonator of Very High Permittivity," *Microwave Theory and Techniques, IEEE Transactions on*, vol. 23, no. 2, pp. 199–208, Feb 1975.

[63] J. V. Bladel, "The Excitation of Dielectric Resonators of Very High Permittivity," *Microwave Theory and Techniques, IEEE Transactions on*, vol. 23, no. 2, pp. 208–217, Feb 1975.

[64] M. T. K. Tam and R. D. Murch, "Half volume dielectric resonator antenna designs," *Electronics Letters*, vol. 33, no. 23, pp. 1914–1916, 1997.

[65] R. Kumar Mongia and A. Ittipiboon, "Theoretical and experimental investigations on rectangular dielectric resonator antennas," *Antennas and Propagation, IEEE Transactions on*, vol. 45, no. 9, pp. 1348–1356, 1997.

[66] A. A. Kishk, "Wide-band truncated tetrahedron dielectric resonator antenna excited by a coaxial probe," *Antennas and Propagation, IEEE Transactions on*, vol. 51, no. 10, pp. 2913–2917, 2003.

[67] L. Kwok Wa, "Conformal strip excitation of dielectric resonator antenna," *Antennas and Propagation, IEEE Transactions on*, vol. 48, no. 6, pp. 961–967, 2000.

[68] A. Petosa, R. Mongia, A. Ittipiboon, and J. Wright, "Design of microstrip-fed series array of dielectric resonator antennas," *Electronics Letters*, vol. 31, no. 16, pp. 1306–1307, Aug 1995.

[69] M. Haneishi and B. Wu, "Array antenna composed of circularly polarized dielectric resonator antennas," in *Antennas and Propagation Society International Symposium, 1999. IEEE*, vol. 1, July 1999, pp. 252–255 vol.1.

[70] G. Yuehe and K. P. Esselle, "An extremely compact dielectric resonator antenna for space-limited UWB wireless communication devices," in *Radar Conference, 2009. EuRAD 2009. European*, 2009, pp. 393–396.

[71] R. Mongia, "Half-split dielectric resonator placed on metallic plane for antenna applications," *Electronics Letters*, vol. 25, no. 7, pp. 462–464, March 1989.

[72] M. Verplanken and J. Bladel, "The Electric-Dipole Resonances of Ring Resonators of Very High Permittivity (Short Papers)," *Microwave Theory and Techniques, IEEE Transactions on*, vol. 24, no. 2, pp. 108–112, Feb 1976.

[73] C. Ozzaim, "Monopole Antenna Loaded by a Stepped-Radius Dielectric Ring Resonator for Ultrawide Bandwidth," *Antennas and Wireless Propagation Letters, IEEE*, vol. 10, pp. 843–845, 2011.

[74] A. Ittipiboon, R. Mongia, Y. Antar, P. Bhartia, and M. Cuhaci, "Aperture fed rectangular and triangular dielectric resonators for use as magnetic dipole antennas," *Electronics Letters*, vol. 29, no. 23, pp. 2001–2002, Nov 1993.

[75] A. Kishk, "Tetrahedron and triangular dielectric resonator antenna with wideband performance," in *Antennas and Propagation Society International Symposium, 2002. IEEE*, vol. 4, 2002, pp. 462–465 vol.4.

[76] A. A. Kishk, Z. Xiao, A. W. Glisson, and D. Kajfez, "Numerical analysis of stacked dielectric resonator antennas excited by a coaxial probe for wideband applications," *Antennas and Propagation, IEEE Transactions on*, vol. 51, no. 8, pp. 1996–2006, 2003.

[77] R. K. Chaudhary, K. V. Srivastava, and A. Biswas, "Wideband Multi-layer Multi-permittivity Half-split Cylindrical Dielectric Resonator Antenna," *Microwave and Optical Technology Letters*, vol. 54, pp. 2587–2590, 2012.

[78] D. Guha, B. Gupta, and Y. M. M. Antar, "Hybrid Monopole-DRAs Using Hemi-spherical/ Conical-Shaped Dielectric Ring Resonators: Improved Ultrawideband Designs," *IEEE Trans. Antennas Propag.*, vol. 60, no. 1, pp. 393–398, 2012.

[79] S.-M. Deng, C.-L. Tsai, S.-F. Chang, and S.-S. Bor, "A CPW-fed suspended, low profile rectangular dielectric resonator antenna for wideband operation," in *Antennas and Propagation Society International Symposium, 2005 IEEE*, vol. 4B, July, pp. 242–245 vol. 4B.

[80] Y. G. Y. Ruan and X. Shi, "Double annular-ring dielectric resonator antenna for ultra-wideband application," *Microwave and Optical Technology Letters*, vol. 49, pp. 362–366, Feb,2007.

[81] B. I. Lembrikov, *Novel Applications of the UWB Technologies*, T. Smiljanic, Ed. InTech, 2011. [Online]. Available: www.intechopen.com

[82] T. W. Barrett, "History of Ultra Wideband (UWB) Radar and Communication: Pioneers and Innovators." Proceedings of Progress in Electromagnetics Symposium, Cambridge, MA, July 2000.

[83] C. A. Balanis, *Antenna Theory: Analysis and Design*, 3rd ed., 2005, no. 978-0-471-66782-7.

[84] D. Lamensdorf and L. Susman, "Baseband-pulse-antenna techniques," *IEEE Antennas Propag. Mag.*, vol. 36, no. 1, pp. 20–30, 1994.

[85] *IEEE Standard for Definitions of Terms for Antennas*, Std., March 2014.

[86] Q. H. Abbasi, M. M. Khan, S. Liaqat, M. Kamran, A. Alomainy, and Y. Hao, "Experimental investigation of ultra wideband diversity techniques for on-body radio communications," *Progress In Electromagnetics Research C*, vol. 34, pp. 165–181, 2013.

[87] Q. Abbasi, M. Rehman, X. Yang, A. Alomainy, E. Serpedin, and K. Qaraqe, "Ultra wideband band-notched flexible antenna for wearable applications," *IEEE Antenna and Wireless Propagation letter*, no. 99, pp. 1–1, 2013.

[88] X. Yong, L. Yinghua, Z. Hongxin, and W. Yeqiu, "An overview of ultra-wideband technique application for medial engineering," in *Complex Medical Engineering, 2007. CME 2007. IEEE/ICME International Conference on*, May 2007, pp. 408–411.

[89] R. Jain). FCC Approves First Commercial UWB Chipset. [Online]. Available: http://www.cse.wustl.edu/ jain/cse574-08/ftp/uwb/

[90] Q. H. Abbasi, A. Sani, A. Alomainy, and Y. Hao, "On-body radio channel characterization and system-level modeling for multiband ofdm ultra-wideband body-centric wireless network," *Microwave Theory and Techniques, IEEE Transactions on*, vol. 58, no. 12, pp. 3485–3492, 2010.

[91] H. Abbasi, A. Sani, A. Alomainy, and Y. Hao, "Arm movements effect on ultra wideband on-body propagation channels and radio systems," in *Antennas & Propagation Conference, Loughborough 2009.* IEEE, 2009, pp. 261–264.

[92] "First Report and Order in the Matter of Revision of Part 15 of the Commissions Rules Regarding Ultra-Wideband Transmission Systems," *ET Docket 98-153 Federal Communication Commission*, Apr 2002.

[93] Y. Ge, K. Esselle, and T. Bird, "Wideband Stacked Dielectric Resonator Antennas," in *Int. Workshop on Antenna Technology: Small and Smart Antennas Metamaterials and Applications, 2007. IWAT '07.*, 2007, pp. 303–306.

[94] G. Yuehe and K. P. Esselle, "A dielectric resonator antenna for UWB applications," in *Antennas and Propagation Society International Symposium, 2009. APSURSI '09. IEEE*, 2009, pp. 1–4.

[95] Y. Ge, K. Esselle, and T. Bird, *Antennas and Propagation, IEEE Transactions on*, no. 9, pp. 3445–3448, Sept.

[96] G. P. Junker, A. A. Kishk, A. W. Glisson, and D. Kajfez, "Effect of fabrication imperfections for ground-plane-backed dielectric-resonator antennas," *IEEE Antennas Propag. Mag.*, vol. 37, no. 1, pp. 40–47, 1995.

[97] K. M. Luk. and K. W. Leung., *Dielectric Resonator Antennas.* Research Studies Pr Ltd, 2004.

[98] Y. Ranga, L. Matekovits, K. Esselle, and A. R. Weily, "AMultioctave Frequency Selective Surface Reflector for Ultrawideband Antennas," *IEEE Antennas Propag. Lett.*, vol. 10, pp. 219–222, 2011.

[99] G. Brooker, *Introduction to Sensors for Ranging and Imaging*, First ed. SciTech Publishing, December Dec 2009.

[100] Q. Wu, R. Jin, J. Geng, and M. Ding, "Pulse Preserving Capabilities of Printed Circular Disk Monopole Antennas With Different Grounds for the Specified Input

Signal Forms," *IEEE Trans. Antennas Propag.*, vol. 55, no. 10, pp. 2866–2873, Oct 2007.

[101] D. Pozar, *Microwave Engineering*, 3rd ed. John Wiley & Sons, 2005.

[102] M. A. M .Mirshafiei and L. A. P. Larochelleand Rusch, "Pulse shapes that outperform traditional uwb antenna/waveform combinations," in *IEEE Global Telecommunications Conference (GLOBECOM)*, Dec 2010.

[103] S. Gabriel, R. W. Lau, and C. Gabriel, "The dielectric properties of biological tissues: Measurements in the frequency range 10 Hz to 20 GHz," *Physics in Medicine and Biology*, vol. 41, no. 11, p. 2251, 1996.

[104] S. G. O. G. Martinsen and H. P. Schwan, "Interface phenomena and dielectric properties of biological tissue," *Encyclopedia of Surface and Collied Science*, New York: Marcel Dekker, 2002.

[105] N. Chahat, M. Zhadobov, R. Sauleau, and K. Ito, "A Compact UWB Antenna for On-Body Applications," *Antennas and Propagation, IEEE Transactions on*, vol. 59, no. 4, pp. 1123–1131, April 2011.